Design and Control of an Active Knee Exoskeleton for Walking Assistance of CP Hemiplegic Patients

BY

SARA LO VECCHIO
B.S., Politecnico di Torino, Turin, Italy, 2019

THESIS

Submitted as partial fulfillment of the requirements
for the degree of Master of Science in Mechatronic Engineering
in the Graduate College of the
Politecnico di Torino, 2021

Turin, Italy

Defense Committee:

Milos Zefran, Chair and Advisor
Ming Wu
Alessandro Rizzo, Politecnico di Torino

To my Papi, Mimi and Zofi; we are infinite.

ACKNOWLEDGMENTS

First and foremost, I cannot begin to express my thanks to my parents for the never-ending support and trust, even and especially in cases in which they kindly disagree. Thank you for letting me go all the times I need to.

I would like to express my gratitude to Professor Ming Wu, for giving me the opportunity to work on a stimulating and insightful project that encompasses all of my passions and has allowed me to learn a lot. I also wish to thank Professor Milos Zefran and Professor Alessandro Rizzo for the precious support even from afar.

Reaching the end of these five years journey has been challenging under all the aspects of life. I am truly, deeply indebted to the people who stayed next to me everyday, between Turin, Madrid and Chicago, despite the significant quantity of challenges that being in touch with me involves.

A huge thanks goes to Gaia, for looking at me like I am the most shining star in the universe. Thank you for the strength you give me everyday, the real wealth is having you by my side.

ACKNOWLEDGMENTS (continued)

I am extremely grateful to Paola, the other end of the red thread, my other half, my Everglow, my Thunder. Thank you for sharing the lowest moments and making them precious memories, thank you for being my soulmate.

I am truly thankful to Valeria, for so many things that a whole book wouldn't be enough to write them all. But most of all, thank you for choosing to grow up with me. I think that we can say, *with absolute certainty, that we will forever walk at a brisk pace together.*

You girls saved me so many times I will never be thankful enough. I love you with all my heart, I really do.

I am really grateful to Matteo, who has come to mean so much to me during this last year. Some human connections are meant to be, just like ours. We will always be under the same stars.

Last but not least, I want to thank my little sister Sofia, for being the first one to read this dissertation. I just wanted you to know that you are already infinite times better than me.

SLV

TABLE OF CONTENTS

TABLE OF CONTENTS (continued)

CHAPTER **PAGE**

LIST OF TABLES

LIST OF FIGURES

LIST OF FIGURES (continued)

LIST OF ABBREVIATIONS

ICP	Infantile Cerebral Palsy
CNS	Central Nervous System
LE	Lower extremities
SCPE	Surveillance of Cerebral Palsy in Europe
GMFCS	Gross Motor Function Classification System
TZ	Trapezius
ES	Erector Spinae
RA	Rectus Abdominis
EO	External Oblique
GMx	Gluteus Maximus
pGMd	Posterior Gluteus Medius
RF	Rectus Femoris
ST	Semitendinous
TFL	Tensor Fascia Latae
EMG	Electromyography
PPAM	Pleated Pneumatic Artificial Muscles
SEA	Series Elastic Actuator

LIST OF ABBREVIATIONS (continued)

IMU	Inertia Measurement Unit
AAN	Assist As Needed
BLDC	Brushless Direct Current
FSR	Force Sensing Resistor
FSM	Finite State Machine
I^2C	Inter Integrated Circuit
SDA	Serial Data
SCL	Serial Clock
LPF	Low Pass Filter
GND	Ground
PWM	Pulse Width Modulation
PID	Proportional Integral Derivative
PI	Proportional Integral
A/D	Analog to Digital
CoM	Center of Mass
MIL	Model-in-the Loop
PIL	Processor-in-the Loop
EMF	Electromagnetic Force
PMSM	Permanent magnet Synchronous motor

SUMMARY

Patients affected by Cerebral Palsy show various grades of crouch gait. In order to improve their knee extension during the critical phases of walking, they are subjected to physical rehabilitation protocols. This thesis presents the development of a robotic exoskeleton device for the knee joint of hemiplegic patients that could enhance therapy results giving an assistive torque during particular phases of gait.

The device features a modular passive knee brace designed for post-op rehabilitation that has been modified with an aluminum motor support. The motor is actuated via Bowden-cable transmission; while a closed-loop controller provides the reactive torque to the patients through high frequency real-time measurements. The time instant in which the assistance is needed is detected by a control software model designed for gait event detection.

Preliminary Processor-in-the-loop testing has been made before the validation with human subjects affected by hemiplegia derived from low level Cerebral Palsy.

The future investigation with this device will be focused on the improvement of its weight and the control algorithm optimization, which will require an hardware advancement.

CHAPTER 1

INTRODUCTION

1.1 Motivation - Cerebral Palsy

Infantile cerebral palsies (ICPs) are a heterogeneous group of permanent developmental, movement, and posture disorders that cause activity limitation. They are attributed to permanent, non-progressive damage that has occurred in the CNS during fetal or infant development [1]. The damage may be represented by a malformation, injury, or an interference with the CNS development. Motor disorders are often accompanied by sensory, perceptual, cognitive, communicative, behavioral disorders as well as epilepsy or secondary musculoskeletal problems.

The key element of this disorder is that it is a permanent but not immutable impairment that creates a severe functional limitation or disability. During embryonic development there is a damage of certain brain areas, depending on the gestational period, following which there is no longer a normal neurological development. It is called a non-progressive damage because when an area is not mature or has suffered a significant damage, thereafter all those functions that are within its competence will be compromised. What emerges is that every child with a clinical picture of paralysis needs an individualized and multidimensional diagnostic and therapeutic pathway, since in a still developing encephalon that suffers a damage the compromised functions are superior. Therefore, the deduction is that the ICP definition includes a

360-degree involvement with impairment of language, vision, hearing depending on the extent and magnitude of the lesion reported.

1.1.1 Epidemiology

ICP is one of the most frequent causes of physical disability in childhood. The incidence in high-income countries is between 1.4 and 2.7 per thousand births. Data comes from population registries, primarily from the Australian Cerebral Palsy Register and the European Register.

However, it would seem, from the latest available data, that the prevalence and severity rates of ICP in Western countries are decreasing, both in term and preterm births, due to the impact of research, improvements in both obstetric and neonatal prevention and care, and greater attention in public and health policies to the gestational period. This finding applies to both postnatal and pre/perinatal forms.

1.1.2 Causal and predisposing factors

ICP is a heterogeneous set of clinical conditions that are the end result of different pathophysiological patterns. It is not always possible to trace the etiological cause, but with a good history it is possible to trace the risk factors. However, it is believed that most cases of ICP result from a joint action, thus due not only to environmental factors but also to genetic susceptibility. Prematurity and hypoxic-ischemic encephalopathy are thought to be the most relevant factors. However, in $\frac{1}{3}$ of subjects with ICP it is not possible to highlight known risk factors and, according to recent findings, genetics plays an important role in many of these forms. Prenatal factors together account for approximately 94% of the causes of ICP.

1.1.3 Classification approaches

ICP can be determined by various etiologic causes contributing to the damage. This heterogeneity needs a nosography of clinical pictures in order to give uniformity to clinical groups and to be able to plan an effective and targeted treatment [2].

Classification approaches may concern:

- Global picture of the disorder and its severity;
- Type and location of motor impairment (with consequences on motor activities);
- Presence of comorbidity (e.g. cognitive impairment, attentional difficulties);
- Anatomical distribution of the damage;
- Etiological classification;
- Clinic of the disorder.

1.1.3.1 Topographical classification

It takes into account the motor impairment distribution to various body segments:

- monoplegia;
- diplegia (impairment of all four limbs with greater involvement of the lower limbs);
- triplegia (generally LE and one upper limb);
- paraplegia;
- hemiplegia;
- quadriplegia.

However, this classification tends to place a predominant emphasis on motor impairment of the limbs, neglecting the trunk, bulbar motility, and oropharyngeal motility. In addition, the judgment of severity of motor impairment has been criticized for being excessively subjective and for not taking into account the structural and functional differences between upper and lower limbs.

1.1.3.1.1 Hemiplegia

Focusing on hemiplegia, it is possible to provide a brief description in order to understand its main features.

Hemiplegia's forms are almost always spastic and the most frequent type of ICP in term births and the second in premature infants [1]. Motor impairment is often predominantly distal. Associated movements may be characteristically present, such as synergies (activation of distal modules triggers the entire movement sequence) and synkinesias (voluntary movements of the non-paretic limb induce involuntary movements in the paretic limb). Spasticity generally shows up later during development and the prognosis for walking is always favorable. However, muscle contracture or bone changes may develop over time. In addition, the presence of sensory and perceptual disturbances is generally less present than in other forms of ICP. On the other hand, attention disorders, in the form of visual neglect and related to other perceptual components, which can lead to the non-use of the paretic limb, are more relevant. Presence of epilepsy is also frequent. With regard to higher functions, the alteration of specific domains is generally more frequent than the intellectual disability.

The first signs of motor deficit become apparent around 3 to 6 months of age. In fact, clinicians accustomed to seeing children as early as three months can see evidence of a possible lesion and thus begin early diagnosis and rehabilitation therapy.

1.1.3.2 Functional classification

It is related to how much motor impairment and associated deficits affect activity limitation (disability). The SCPE recommends the use of the Gross Motor Function Classification System (GMFCS) to assess the degree of lower extremity impairment [2]. It is characterized by a 5-level scale:

I. walking without limitation;

II. walking with limitation;

III. walking with manual mobility device;

IV. movement possible only with motor structure aid;

V. transport with manual wheelchair.

These descriptors are applied for children ages 6 to 12.

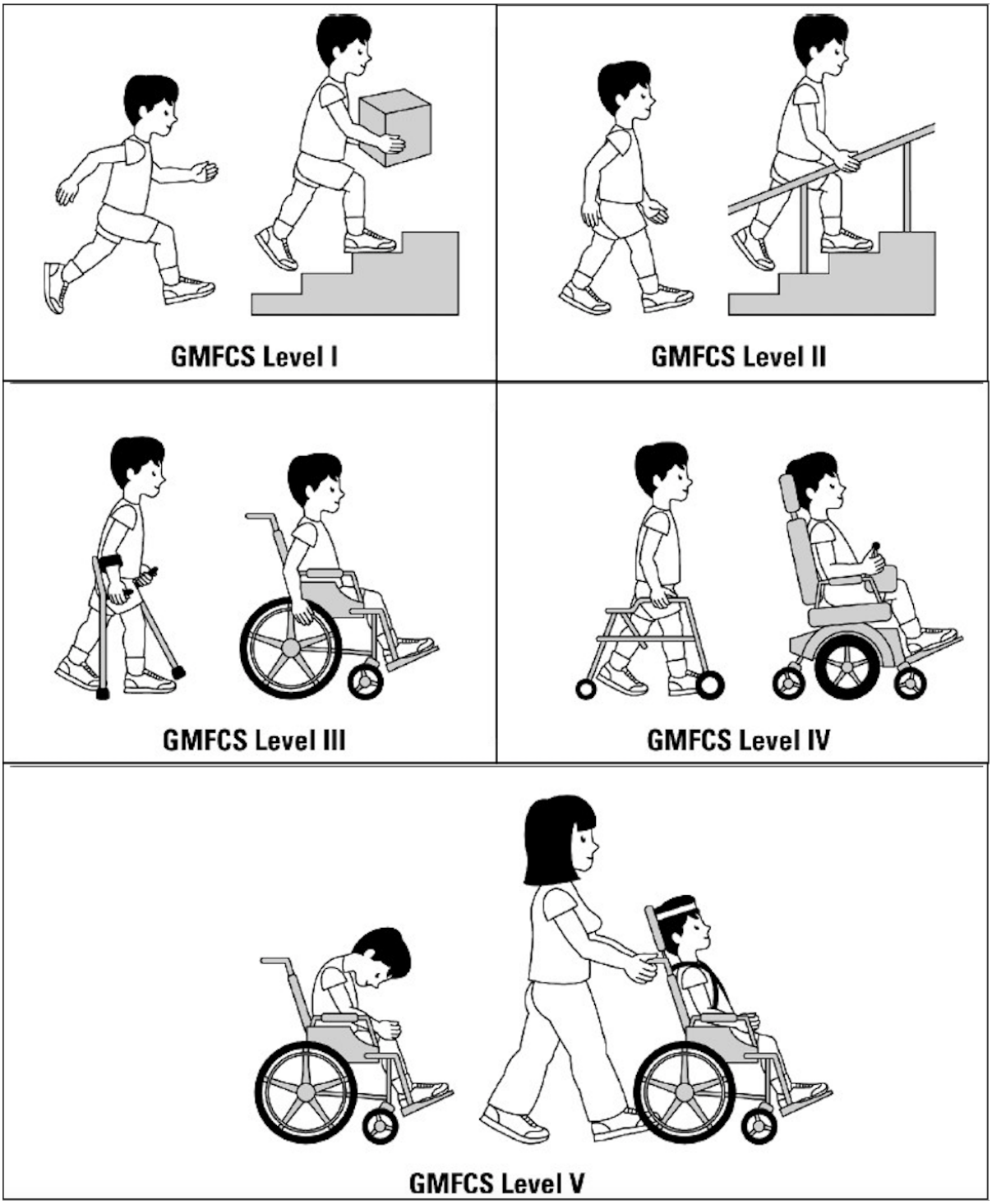

Figure 1: GMFCS CP Functional Classification

TABLE I: GMFCS CP Degree Functional Classification

GMFCS Level	Description
I	Child shows walking activity in different social contexts. He is able to climb stairs without using any kind of support. He shows limited skills in terms of speed, coordination and balance.
II	Child shows walking ability and is able to climbs stairs with the supporting usage of a railing. External factors such as crowded areas, limited spaces, inclined roads, uneven terrain could compromise his capabilities and comfort. He may need an assisting handheld mobility device over long distances. High-consuming motor activities like running and jumping could lead to an under-performance in comparison with a child of the same age.
III	Child needs an handheld mobility device in order to perform walking activities, a wheeled mobility when traveling for long distances. He could be able to climb stairs with appropriate support.
IV	Child's walking activity is limited to short distances performed indoors with compulsory physical assistance or usage of a powered body support walker. In the outdoor spaces or in the community the child needs to be transported manually through a wheelchair or using powered mobility.
V	Child needs to be transported in a manual wheelchair in all contexts and situations. He needs support in order to maintain antigravity head and trunk postures; his ability to control arm and leg movements is limited.

1.2 Gait analysis and muscle activation

1.2.1 Gait abnormalities in children with Cerebral Palsy

Children with CP manifest vast gait patterns. The foremost common abnormality is what is referred to as stiff knee gait. It has been studied and analyzed by T. A. L. Wren in 2005 [3]. The following definition has been provided: the stiff knee gait is characterized by a decreased arc of knee motion, from the maximum knee extension angle during stance phase to the peak knee flexion angle during swing phase. It could also be frequently associated to a perceptible delay in peak swing knee flexion to mid- or terminal swing. The studies conduced by Wren showed that approximately 80% of CP patients are affected by stiff knee gait. Furthermore, the second most common gait abnormality that arose was crouch gait, which is characterized by an increased knee flexion during stance phase. The percentage of reported cases is approximately equal to the 69%. Hemiplegic patients showed a prevalence of varus foot deformities compared to the ones with bilateral involvement. Walking habitually with these gait abnormalities increases the danger for bone deformities, especially rotational misalignments such femoral or tibial internal rotation [3]. The challenges that children with CP have to face result in a social and community life that is comparatively less participatory than that of their typical developing (TD) peers.

Physical therapy is the key factor for a consistent improvement in mobility skills. For instance, after studying activity-focused motor interventions, Valvano [4] reported that with constant practice in time, ankle and pelvis movement coordination improved in children with spastic diplegia. This was also related to improvements in walking speed and efficiency.

Furthermore, Bjornson claims that: “interventions aimed toward improving daily ambulation activity performance appear to possess the foremost potential for change in youth with CP in GMFCS levels II and III” [5]. These results point to a requirement for CP children to possess assistive devices that provide them equivalent opportunities for community activities as their TD peers.

Recent studies conduced on CP patients belonging to all the 5 GMFCS categories [6] have demonstrated that the prevalence of a certain gait abnormality varies with respect to the GMFCS class. Moreover, crouch gait and out-toeing seems to increase with age while equinus and in-toeing shows a reduction during lifetime. These new outcomes are fundamental for an even more peculiar design of a device that is dedicated to a specific GMFCS class.

1.2.2 Natural gait description and differences with Crouch Gait

Understanding and analyzing each phase of the human body's natural gait is a fundamental step in the design of an active electromechanical support. Human gait can be divided into various phases and this division can be extremely detailed. The main phases of the gait cycle; i.e. the stance phase and the swing phase, can in turn be subdivided into further phases that are strictly dependent on the movements of the lower limbs and their spatial configuration during a precise instant of the single cycle. The gait cycle's phases can be characterized as function of the spatiotemporal pattern of only one or both lower limbs. For the purposes of the design described in this dissertation, the gait cycle is here divided into seven phases, each of which is related to the movement of both limbs.

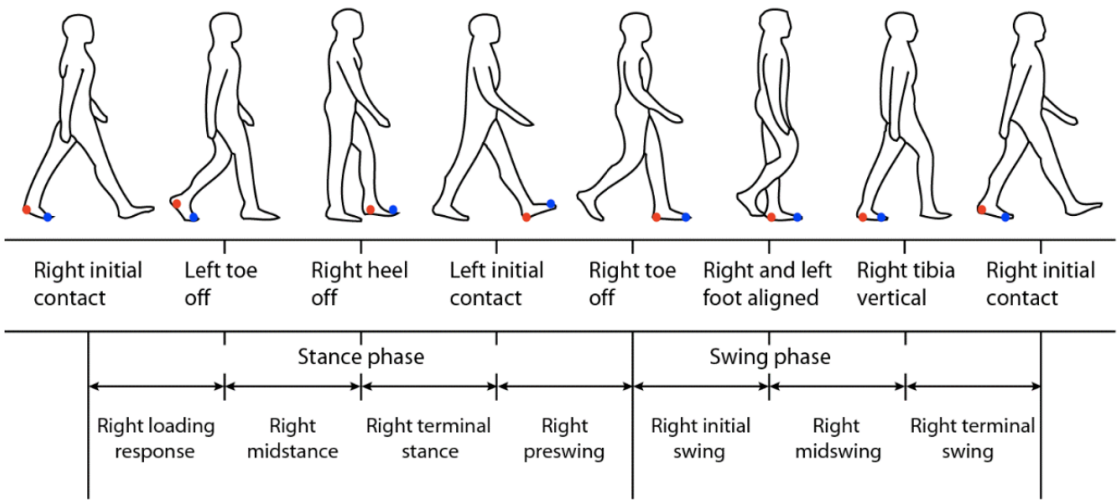

Figure 2: Natural gait phases related to both lower limbs

Referring to Fig.2, the gait phases can be described as follows, taking into account that this description is strictly related to both lower limbs for design purposes; furthermore this division is obtained by thoroughly analyzing the principal stance and swing phases.

- Stance phase covers approximately the 60% of the gait cycle; it is divided in:
  - Right loading response (from 0 to 10% of the cycle); this phase starts with the Initial Contact of the right heel and ends with the Loading Response, which is characterized by the detachment of the left toe from the ground and right leg's weight acceptance. The right knee firstly extends during the Initial contact, then flexes during the Loading Response;
  - Right midstance (from 10 to 30% of the cycle): this phase starts with the left toe off and ends with the right heel off. The right knee extends without reaching 0 degrees;
  - Right terminal stance (from 30 to 50% of the cycle): it begins with the right heel off and ends with the Initial Contact of the left heel. The knee extends and then flexes;
  - Right preswing (from 50 to 60% of the cycle): it starts with the Left Initial Contact and ends with the Right toe off, the knee flexes of several degrees in order to prepare for the swing phase, by transferring the load to the left leg;
- Swing phase is divided in:
  - Right initial swing (from 60 to 73% of the cycle): this phase starts with the right toe off and the allignement of the two feet, the knee angle reaches up to 70 ° of flexion;

- Right midswing (from 73 to 87% of the cycle): during this phase the weight distribution on the left foot becomes Inhomogeneous, since the weight is majorly shifted on the left toe; the right leg is detached from the ground and defines the end of this phase when the right tibia becomes approximately vertical with respect to the ground; the knee angle extends progressively;
- Right terminal swing (from 87 to 100% of the cycle): this phase starts with the left toe detachment, progressive augment of body weight on the left toe and then ends with the beginning of the following gait cycle, which is the Right initial contact. During this phase the knee progressively extends.

It is important to underline that not only the knee articulation behavior and angle changes can be related to the gait cycle; in fact, also the hip and ankle angle have specific reference curve patterns that repeat during basic walking motion. In this subsection, Only the knee angular pattern has been analyzed, for interests linked to the final objective of this project.

1.2.2.1 Crouch Gait peculiarities

Understanding crouch gait and the explanation for its progressive development is still challenging since motions generated by muscles forces are still not clear [7]. Bi-articular muscles may have non-intuitive functions as a result of the dynamic coupling generated by the complex multi-joint linkage that the human body is characterized by [8]. Joint accelerations generated by muscle forces strictly depend upon the body configuration and linkages' orientation, hence crouch gait could reduce the articulations extension range capability. This could be an explanation for the differences in muscle activation while performing walking activity [9]. This leads

to severe consequences from a clinical point of view. First of all, this posture requires an higher muscular force magnitude required to exert movements while maintaining the crouching attitude. The effect that gravity has on Crouch gait is a flexion action at both hip and knee joints, which increases the demands on muscles. Articulations' acceleration requirements change too. Crouch gait subject shows larger knee flexion with respect to normal subject (Figure 3).

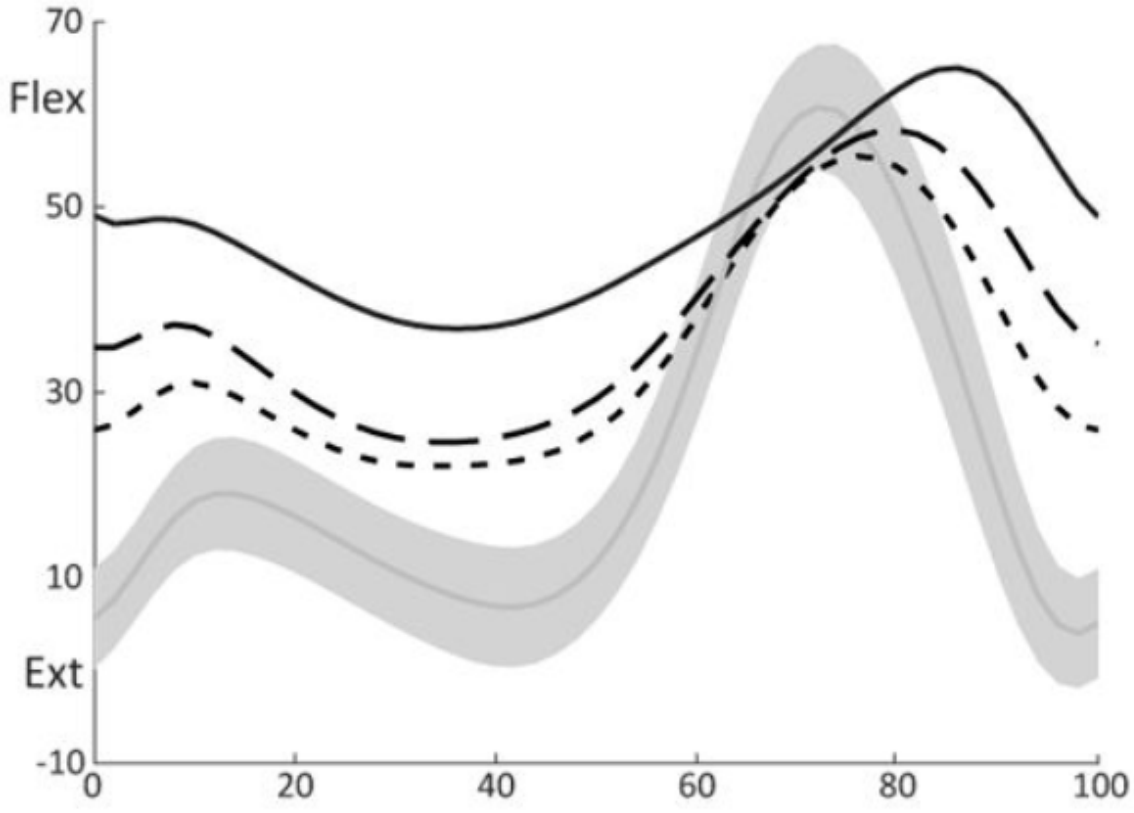

Figure 3: Average joint kinematics for normal and crouch gait[5]. The grey line shows the normal joint pattern, while the black one is related to an increasingly severe crouch gait.

The posture is a limitation in producing the required accelerations during the knee extension phase [7]. Moreover, the capacities of the GMx (Gluteus Maximus), GM (Posterior Gluteus Medus), V (Vasti), and S (Soleus) muscles to extend the joints were markedly reduced. In addition, the activation patterns of the muscles are not coherent with the normal muscles activation phases observed (Figure 4) and appears to be strongly altered.

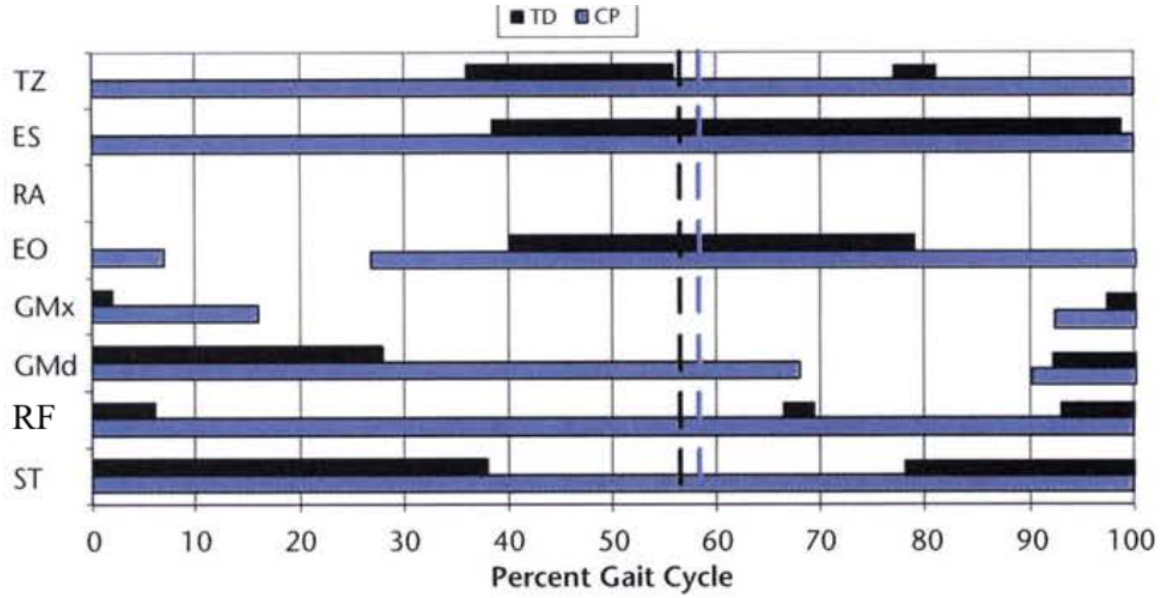

Figure 4: Muscle activity during the gait cycle in children with TD and CP [10].

Analyzing the effect that the muscles have at the knee joint level, it is notable that the PGM has almost no extension capacity, while the of Soleus, Vasti, and GMx were less than 50% with reference to the normal values.This makes it difficult to associate muscle activation during

mobility in a CP patient with a precise moment in the gait cycle. The muscular activation pattern that comes closest to natural human physiology is that of the GMx, but it would still make the determination of a phase of the cycle inaccurate. Furthermore, also the knee flexors show to be affected by the crouched posture. The TFL (tensor fascia latae) showed an higher flexion capability, on the contrary the Psoas showed a reduced flexion capability.

1.3 Physical therapy and Exoskeleton state of the art

As mentioned in previous paragraphs, continuous physical therapy over time is the strategy that most guarantees a consistent improvement in mobility skills and freedom.

1.3.1 Therapeutic Objectives

The therapy should be designed to achieve the following goals:

- Functionality: achievement of motor autonomy (focus on the specific motor goal, ignoring how it is achieved);
- Physical activity: it should be promoted in any child with CP, regardless of the level of disability, for the benefits that it has on neuroplasticity and to prevent musculoskeletal complications;
- Family education: the health status of the child cannot disregard the provision of resources and support to the whole family, an essential living environment for the child.

1.3.1.1 Treatment of Spasticity and Dystonia

It aims to improve mobility in high-functioning patients (GMFCS classes I-III) and to improve posture in order to allow greater comfort in a sitting position, facilitate personal hygiene and reduce chronic pain in low-functioning patients (classes IV-V). First-line interventions include physiokinesiotherapy, occupational therapy, and the use of orthopedic devices.

An orthosis is a rigid orthopedic device that can be fabricated, designed or adapted for children sizes. This device could be use to correct an abnormal position or orientation of the joints of interest. Moreover, it gives the child greater stability and support.

1.4 Exoskeletons for CP patients and state of the art

1.4.1 Exoskeletons used for therapy

The set up of protocols aimed at patients affected by walking abnormalities typical of cerebral palsy gives a good margin of improvement in the quality of movements and muscle energy savings. The number of devices currently available in the market is wide, as well as the features they have. They can be classified primarily according to the type of support they give, which can be active or passive. In the first case, the device is equipped with an electromechanical structure, whose complexity depends on the needs, which applies an external force of various kinds on the patient. In the second case, the device is devoid of any type of actuation and gives the patient support due solely to the mechanical design of the exoskeleton. Moreover, the devices may be designed for different categories of patients, therefore with different needs in terms of joints to be supported and/or actuated, different durations of actuation, different intensities. The use of passive and active wearable devices is a great resource for physiatrists

and kinesiologists who work closely with the patient during therapy. The output force can be generated by different types of actuators, whose electromechanical design determines significant variations that make some of them more suitable for certain applications than others. this aspect will be analyzed in detail in a following chapter. In addition to the actuation system, orthoses can be equipped with a wide range of sensors, useful not only for the collection of patient's physiological data but above all for the correct functioning of the exoskeleton. In fact, it is possible to associate the reception of specific signals to moments of the gait cycle that, if recognized, determine the beginning of the active support phase. The possible applications are various.

Many currently existing active exoskeletons were created with the intention of reinforcing the physical capacities of able-bodied individuals, providing support in the repetitive movements typical of certain work tasks (such as, for example, the work performed by warehouse workers or factory workers) and allowing patients who are severely limited in movement to perform efforts that would be unthinkable to them without full support. Some examples of such devices can be found in Table II.

TABLE II: Main Examples of Active Lower Limb Exoskeletons

Exoskeleton	Objective	Actuator type	Sensor
HAL-3[11] (2003)	Autonomy	DC motor, gearhead, servodriver	EMG sensor, Rotary encoder, Pressure Foot sensor
HAL-5[12] (2006)	Force augmentation and enhanced mobility	DC motor	EMG sensor, Pressure Foot sensor
BLEEX[13] (2006)	Force augmentation	Linear Hydraulic Actuator	IMU, angular sensor, rotary encoder, load distribution sensor, indinometer, linear force sensor, Foot switch
LOPES[14] (2007)	Gait rehabilitation	Series Elastic and Bowden Cable Actuators	EMG, Force sensor, tracking motion system
KNEXO[15] (2010)	Gait rehabilitation	Pleated Pneumatic Artificial Muscles (PPAM)	Incremental encoder, gauge pressure sensor, FSR
CUHK-EXO[16] (2017)	Autonomy	Series Elastic Actuator (SEA)	Potentiometers, encoders, IMUs, Pressure sensors

Therapeutic exoskeletons owe their development to the exoskeletons in Table II and further studies in the field of prosthetics. One of the most advanced sensing techniques used is that of myoelectric prostheses, which exploit the EMG signal [17]. The signal is captured, filtered, analyzed by comparing it with appropriate threshold values and used as a target for motor control. Generally, the contraction of the muscle is sought. This technique has been transferred to exoskeleton applications. However, this signal in CP patients is strongly different from that of healthy individuals, so its use would not be accurate. The EMG signal reading is a

good measure of analysis during the course of therapy to analyze improvements. However, it is important that the design of these devices takes into account the limitations, needs, and goals of the individual patient. Since CP patients are pediatric subjects, the designer must consider the need for a lightweight, ergonomic wearable design that does not excessively burden the child. Focusing on patients with CP, it is possible to identify two main types of devices, which in turn can be subdivided into sub-categories according to different parameters: fully supportive or partially supportive exoskeletons. The main difference between these two classes is the intensity of the force applied at joint's level.

For certain patients, mainly the ones belonging to an high level GMFCS class, the force magnitude applied to the joints needs to be almost equal to the physiological one that a natural walking human being has with the same physical parameters and equal conditions of movement. In this case the exoskeleton actuators substitute the muscle activity and work in synergy to complete the entire movement, drastically reducing muscular implementation and supporting the patient also from a postural point of view.

Partially supported exoskeletons, on the other hand, are mainly dedicated to patients belonging to the lower classes of the GMFCS. They are generally lighter and therefore more comfortable to wear for longer periods than full-support exoskeletons. The active assistance generated has a reduced intensity compared to the total force required to complete the movement. For therapeutic reasons, the percentage varies depending on the needs of the patient and the goal of therapy.

1.4.2 Exoskeletons specifically developed for CP patients

As mentioned above, the design of exoskeletons dedicated to patients with GMFCS grade I to III Cerebral Palsy requires special attention and study of the actuation phases. Replacing active support during 100% of the gait cycle with partial support increases the likelihood that the patient will gain more independence and benefit from physical therapy. In fact, if the child, in the case where he already has partial motor autonomy, is supported and assisted in the movements of the most critical phases of the cycle, he is more likely to obtain a real improvement. There is also the possibility that the patient is able to complete the movement and therefore there is the need to apply a force against the movement's direction, in order to correct his incorrect movements through a compensatory action. A critical aspect of pediatric device design is the weight aspect. In fact, pediatric patients are more sensitive to the size and mass of the orthosis. An exoskeleton that is too heavy could lead to opposite effects to those desired and hinder therapy. The natural gait could be compromised and cause undesirable effects. Another important aspect to be considered in the control of such devices is the trajectory that the joints must follow while performing the action. Generally, the paths that control systems use as reference belong to kinematic data collected from healthy patients. In order to meet the requirements of a specific patient, a possible approach that guarantees a more physiological reference curve is multibody modeling for custom sizing[22]. However, this modeling technique needs a motion capture system to be used.

The following paragraphs describe the devices that represent the primary examples of exoskeletons exclusively dedicated to pediatric patients suffering from neuromuscular disorders.

Studies conducted on patients wearing the Anklebot Exoskeleton [18] revealed that a force-weight of up to 25 N does not alter gait kinematics at the knee joint. The kinematic data collected does not show any significant alteration of the recorded gait with respect to the estimated one. It is inferred that the gait pattern for masses equal to or less than 2.5kg is not modified. Furthermore, during that study it was shown that unilateral loading does not affect the natural gait of the unloaded limb. This aspect had been previously addressed [19][20] but the studies focused on adult patients. This constitutes an important insight for the purpose of therapeutic work with hemiplegic patients. Another example of robotic device dedicated to CP patients is WAKE-UP, that is a Wearable Ankle Knee Exoskeleton [21] designed for rehabilitation of locomotion of pediatric subjects affected by different neurological diseases. Its actuators are SEA composed by DC motors and a torsional spring mounted in series.

The Knee Exoskeleton for Spastic Diplegia Treatment [23] is based on constant assistive forces proportional to the knee extensor demand during stance and late swing phases. It is composed of a sigle-joint actuation module per leg. The knee joint is the one of interest. Following studies conduced on the same device have shown evidence of significant postural improvements [24] and the proof that a long-term therapy leads to a visible enhancement in crouch progressively in time. Furthermore, this device was involved in proving that an extension assistance favorably reduces the excessive knee extension present during stance phase. Also, the peak knee extension increases significantly and the extensor muscle activity decreases slightly during assisted walking. Some patients also showed an improved knee flexor muscles activity. These discoveries sustain the use of wearable exoskeletons for crouch gait therapy[25].

Unlike the previous device, P-LEGS [26] is equipped with a total of 6 degrees of freedom. Furthermore, the control strategy is based on what is called Assist-As-Needed (AAN) algorithm, which leverages a hierarchical control system (divided into high-level and low-level) in order to provide active support when needed. The high-level controller acts as a collector of signals from the sensors and is responsible for determining patient's intent. In turn, the low-level controller receives commands from the high-level controller and implements the desired trajectory. A big limit of the device is the weight, equal to 8 kg.

The Bilateral Ankle Exoskeleton [27] was used in a study demonstrating that walking therapy with exoskeleton assistance was well-tolerated, increased speed and stride length with respect to the unassisted walking motion. The long term protocol showed significant outcomes during unassisted post-therapy walking.

1.5 Thesis objectives and outline

1.5.1 Objective

This project is dedicated to the design of an exoskeleton with a single degree of freedom to assist the hemiplegic patient suffering from cerebral palsy. The device must be able to actively provide support via Bowden cable actuation when needed in order to allow for an effective long-term treatment protocol. The choice of actuator should reflect the requirements in terms of maximum mechanical moment, angular velocity and power. The starting mechanical skeleton consists of a functional passive knee brace, which alone provides support to the knee joint and increases its stability (Figure 5). The control strategy should be based on a hierarchical algorithm capable of providing a rational-based intervention strategy. Various sensors act as triggers for assistance activation during appropriate gait phases. The device must take into account the patient's hemiplegia.

1.5.2 Outline

- In Chapter 2 the Exoskeleton design is presented. The first section shows the mechanical design while in the second one the actuator choice is analyzed. Finally, the sensors chosen to be implemented in this project are shown, with particular attention to their characteristics and how they have been inserted at circuit level in the electronic part of the hardware.
- In Chapter 3 the Control Strategy is presented. The three control levels are explained separately and the MATLAB code is shown in details. When needed, the physical model that is behind the algorithm is presented.

- In Chapter 4 the testing method and set-up is shown, then the results collected are discussed and compared with the expected behavior. It is important to specify that at this stage of the project the actuator part is simulated through a model made in MATLAB/Simulink©.
- Finally, Chapter 5 discusses the overall work done and draws the inferred conclusions.

CHAPTER 2

EXOSKELETON DESIGN

2.1 Passive mechanical part

The first step in the design of an active exoskeleton is the choice of the passive mechanical structure representing the skeleton of the device. Although there are several devices known as soft-exosuits [28], where the support is almost entirely provided by the active assistive system, most exoskeletons have an orthotic-type structural core. In the specific case of pediatric patients with cerebral palsy, a light and unobtrusive structure such as that of exosuits would be an advantage for the patient's freedom of movement. Considering also the young age, an excessive weight compromises the success of a therapy and sometimes the walking activity. However, the knee joint is particularly problematic in CP patients. Therefore, there is a need to immobilize and structurally support the joint in order to achieve a correct movement and posture. The knee is a hinge-type joint, involving primarily flexion and extension and a slight degree of medial and lateral rotation (Figure(5)). However, flexion and extension are only required for walking activity. The lateral rotations compromise stability and furthermore could cause pain and damage to the articulation.

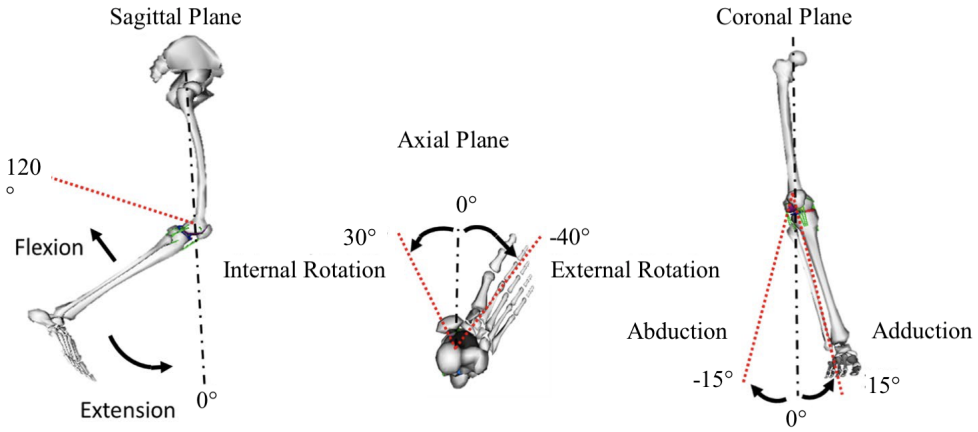

Figure 5: Knee joint degrees of freedom[29]

2.1.1 Passive orthopedic brace

To ensure joint stability during walking, the orthosis in Figure 6 was chosen as the structural core of the exoskeleton. In order to ensure proper alignment between the exoskeleton joint and the joint, the upper and lower legs must be properly secured to the exoskeleton at an appropriate height. The orthosis in question, manufactured by *Orthomen*©, has the following features:

TABLE III: Knee Brace Features

Weight	1,40 kg
Length	adjustable from 48 to 61 cm
Thigh brace circumference	From 15 cm to 60 cm
Calf brace circumference	Up to 48 cm

The brace in concern was suitable for the preliminary tests performed, presented in this dissertation. Its weight is not a limitation for therapy even in pediatric patients. It must be taken into account that the structure presents standard measures which are generally adaptable to a single patient but may be unsuitable for CP patients of very reduced age or of small corporature.

Figure 6: Functional Knee brace by Orthomen

Since the brace is not designed for this specific application, it requires some additional mechanical modifications that enable the Bowden Cable actuator connection and the positioning of sensors. In particular, the support shown in Figure 7 has been produced and mounted. It is useful for the potentiometer sensor mounting and proper connection to the joint. Furthermore, it will be the base on which the Bowden cable joint extremity will be connected, as shown in Figure 11.

Figure 7: Knee brace with additional aluminum support mounted

2.2 Actuator

The actuation method chosen for this exoskeleton was the Bowden Cable-based actuation method (see section 2.2.2 for more details). This choice is due to the great advantages that this technique has when applicable. In fact, it is characterized by a good force transmission and, most importantly, it offers the possibility of locating the actuator away from the patient[30]. High-strength cable materials, which support the transmission of high force magnitude, have been developed during the last years [31]. Thus, the employment of this kind of actuation permits the dislocation of the motor and the remote actuation of the joint of interest. This feature is relevant in the field of wearable active devices, since it does not impose the inertia of the actuator on patient's body. Even though there are evident improvements in terms of functionality and safety, there are still some disadvantages connected to this method. In fact, Bowden cable-based actuation only can operate in pulling direction; moreover the friction is nonlinear and depends on material, curvature and geometry of the cable.

2.2.1 Actuator design: motor and gearhead combination selection

The first step in actuator design is the selection of the motor and, eventually, of the gearbox. This choice strongly depends on the type of application as well as the available budget. A choice that is usually made in the field of wearable exoskeletons as well as in the case of Bowden cable type actuators is the one of Brushless DC (BLDC) motors. The use of this type of motor has various advantages: its light weight, high power-to-size ratio, high efficiency, low inertia, reduced production of heat and electromagnetic noise. The speed range is wide, they have good stability, low vibration and a strong over load capacity. The absence of brushes ensures reduced maintenance requirements and improves motor endurance over time. Disadvantages of this type of motor include it high cost and the mandatory need for an electronic controller switch and Hall sensor or encoder (Appendix A.3).

The design discussed requires a single actuator consisting of a motor capable of supporting knee assistance when needed. The motor in question must be high in horsepower and as small in size as possible. The overall weight must also be very low, preferably less than 1 kg. In practice, small motors result in small torque, which is why they should be combined with a suitable gearbox.

The maximum knee extensor torque recorded during walking motion at moderate speeds [32] is used to select the maximum output nominal torque needed in this project. Considering a maximum knee extensor torque of $0,38\frac{Nm}{kg}$, and a patient of $m = 50kg$, if the maximum

assistive torque would be equal to 40% of the maximum one, the actuator were to generate a torque equal to:

$$\tau_{\text{out}} = 0,38\frac{N}{kg} \cdot 50kg \cdot 40\% = 7,6Nm \tag{2.1}$$

The motor and gearbox combinations listed in Table IV have been analyzed in terms of weight, power and maximum output torque in order to choose the most suitable one for the exoskeleton in exam. All the motors chosen are high power BLDC motors.

TABLE IV: Motor and Gearhead Selection Procedure

Motor	m_M	Gearhead	m_G	m_{tot}	τ_n
EC 60, 150W 625858	350 g	GP 52, 4-30 Nm N=56	770 g	1120 g	15,7 Nm
EC 40, 170 W 393023	580 g	GP 42, 3-15 Nm N=150	560 g	1140 g	17,11 Nm
EC 45, 120 W 608148	149 g	GP 42, 3-15 Nm N=156	460 g	609 g	19 Nm
EC-i 40, 130 W 676600	587 g	GP 42, 3-15 Nm N=81	460 g	1047 g	16,9 Nm
EC-4 pole 30 200 W 305013	300 g	GP 32, 4-8 Nm N=123	210 g	510 g	8,23 Nm

It is evident that all these motor-gearhead combinations have an higher torque than required, hence this parameter does not constitute a limitation. Each norminal output torque is computed as follows:

$$\tau_{\mathrm{n}} = \tau_{\mathrm{nMotor}} \cdot N \cdot \xi \tag{2.2}$$

Where ξ is the gearhead efficiency and N the reduction ratio; while $\tau_{\mathrm{nMotor}}$is the nominal motor torque. Further attention is dedicated to the total mass, which for most combinations exceeds 1kg. As previously noted, in the case of wearable devices, especially if intended for pediatric patients, the total weight of the device should be as low as possible. In addition, the highest possible power ensures that high output speeds are achieved in less time. Therefore, the choice falls on the last combination in the table. The motor and gearhead in question (Appendix A.1 and A.2) meet all requirements. Furthermore, the nominal output speed is such as to support the eventual maximum rotation speed of the knee [33]. Considering a maximum knee rotation speed of $60rpm = 360\frac{\mathrm{deg}}{sec}$ for a maximum walking speed of $1,6\frac{m}{s}$, and comparing this to the nominal output speed of:

$$v_{\mathrm{n}} = \frac{v_{\mathrm{nMotor}}}{N}\xi = 95,04rpm \tag{2.3}$$

Figure 8: selected Gearhead by Maxon©

Figure 9: selected Motor by Maxon©

2.2.2 Bowden Cable Actuation method

The Bowden cable-based is a remote actuation method. The actuator can be placed far away from the joint to be actuated, even out of the exoskeleton itself.In fact, the actuator chosen in this type of application is bulky and does not weigh on the body but is placed on an external support surface. In this design, the actuator is intended to be worn around the patient's waist by means of a special belt; inside a box containing the motor and gearbox, the servodriver (Appendix A.4), the main battery, the safety system with a special button on the

output. The motor will be driven by the servodriver, communicating with the controller when necessary and giving assistance in terms of extension, so the cable will pull in the direction of the motor, lifting the lower limb. As illustrated in Figure 11, the knee joint is not directly actuated by the cable. In fact, the linear force f_l actuates on the calf, which is lifted upwards. Regardless, the motor torque τ_m is still function of the knee joint, since the velocity output of the actuator has to reflect the necessities of the joint motion.

Figure 10: Bowden cable for remote release

In addition, the analytical model of the actuation system may take into account the presence of the Bowden cable. In the following section, the model used in the implementation of this project is explained.

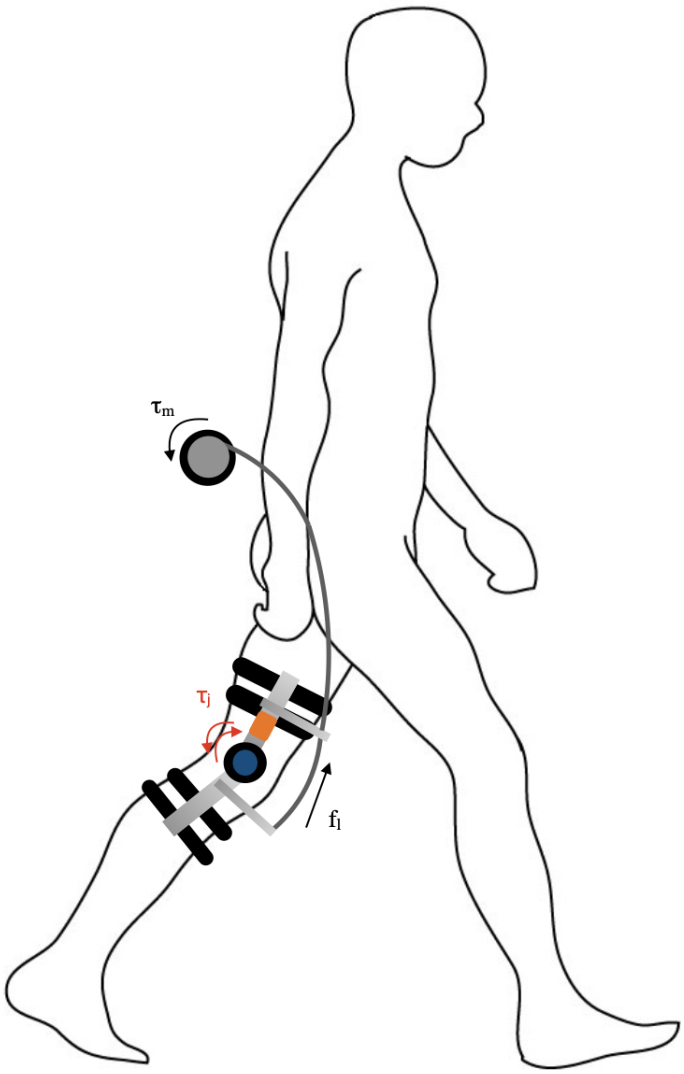

Figure 11: sketch representing the connection between the actuator and the exoskeleton

2.2.3 Actuation System Analytical model

The actuator can be modeled considering the Bowden cable characteristics and the motor rotation angle separately, in relation to both the cable shift and the exoskeleton characteristics[34].

2.2.3.1 Bowden Cable model

The Bowden cable is characterized by a nonlinear friction, which can be modeled as a the efficiency resulting from the connection between joint and actuator [35]. The force that the inner cable develops when a torque τ_{j} is generated at joint level, being r_{j} the radius of the pulley at the joint is equal to:

$$F_{\mathrm{bc}} = \frac{\tau_{\mathrm{j}}}{r_{\mathrm{j}}} e^{\mu\Phi} \tag{2.4}$$

where μ is the sliding friction coefficient [36] that in this specific case of a steel teflon coated cable is equal to 0,092. Φ is the bending angle of the cable, that for the sake of simplicity it is approximated constant and equal to $\frac{\pi}{2}$.

It is important to underline that r_{j} is a design parameter of the exoskeleton, while τ_{j} choices could be limited by certain limits imposed by the designed therapy, patients' necessities or actuator capabilities.

The displacement x_{bc} of the cable subject to the force in Equation (2.4) is equal to:

$$x_{\mathrm{bc}} = \theta_{\mathrm{j}} r_{\mathrm{j}} + \frac{F_{\mathrm{bc}}}{k_{\mathrm{bc}}} \tag{2.5}$$

Where θ_{j} is the angle spaced by the joint of interest and k_{bc} is the axial stiffness, which is a parameter dependent to the inner cable section area, length and material. In this specific case, the inner cable is made of steel and has a diameter equal to $d = 1,53mm$ that has been measured with an high precision caliber and a length of $L = 1,5m$. Hence, the axial stiffness results equal to:

$$k_{\mathrm{cb}} = \frac{E_{\mathrm{steel}} \cdot A_{\mathrm{cb}}}{L_{\mathrm{cb}}} \tag{2.6}$$

Where $E_{\mathrm{steel}} = \frac{200kN}{mm^2}$ is the Young Modulus of Steel.

2.2.3.2 Motor model

The angle that the motor spaced during the rotation that results in the x_{bc} cable displacement during pulling actuation can be modeled as follows:

$$\theta_{\mathrm{m}} = \frac{x_{\mathrm{bc}}}{r_{\mathrm{m}}} \tag{2.7}$$

The radius of the motor pulley r_{m} is also a design parameter.

$$\theta_{\mathrm{m}} = \frac{\theta_{\mathrm{j}} r_{\mathrm{j}}}{r_{\mathrm{m}}} + \frac{F_{\mathrm{bc}}}{k_{\mathrm{bc}} r_{\mathrm{m}}} \tag{2.8}$$

It is underlined that the two terms of the right-hand side of the equation (2.8) represent, respectively, the relation between the joint and the motor rotation angle neglecting the cable friction effect, and the additional angular motion needed in order to take the Bowden Cable axial stiffness into account.

Computing the first derivative of (2.7) $\dot{\theta}_{\mathrm{m}}$ it is possible to obtain the motor angular velocity needed in order to induce an angular displacement θ_{j} and torque θ_{j} at the joint, compensating the cable friction effect.

The required actuation output of the motor can be described also in terms of torque, as in the equation that follows:

$$\tau_{\mathrm{m}} = \ddot{\theta}_{\mathrm{m}} I_{\mathrm{m}} + F_{\mathrm{bc}} r_{\mathrm{m}} \tag{2.9}$$

where also the rotor inertia $\mathrm{I_m}$ is taken into account.

2.3 Sensors

Sensors are a key part of this project as they compensate for the lack of an inertial model of the orthosis and are responsible for detecting the patient's intentions and movements, which determine the implementation steps. Primarily, 3 different sensors were chosen that are responsible for tasks related to the high-level control phase. The use of EMG sensors was evaluated but discarded due to the difficulty in detecting movement intentions of CP patients from such signals, which are quite distorted. A simple filtering circuit design was done for each sensor used to make the input signal to the controller smoother and less noisy. The IMU sensor takes care of walking speed estimation, while the potentiometer and Force Sensing Resistors (FSR) work at the Finite State Machine (FSM) level to detect gait phase.

2.3.1 IMU

The Inertial Measurement Unit (IMU) is an integrated circuit based on inertial sensors, such as accelerometers and gyroscopes, which allow the monitoring of the dynamics of a moving

object or vehicle. It is used to detect orientation by measuring pitch, roll and yaw angles. A 9-axis IMU such as the one used (Figure 12) combines a 3-axis gyroscope, a 3-axis compass, and a 3-axis accelerometer.

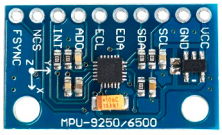

Figure 12: MPU-9250 IMU 9-axis sensor

These sensors are accurate but require initial calibration in order to adjust the offset of the input signal. In addition, the signal needs to be filtered in order to improve its readability. Oscillations strongly disturb the measurements, so the possibility of error must be taken into account. The sensor in question is mounted just above the knee joint, at the low lateral thigh. For reasons of greater stability and orientation it has been anchored to the flat metal plate of the orthosis. Not all the integrated circuit pins are of interest: in fact only the first four have been soldered, that is those relating to power supply and communication I^2C (Inter Integrated Circuit) or SDA (Serial Data) which reports data from the circuit to the board and SCL (Serial CLock) which is the clock line.

2.3.2 FSR

FSR was used in the construction of a pressure foot sensor. It is a variable resistance to the force exerted on it. The surface area can be relatively small or large depending on the sensor chosen, as well as the range of pressures borne by it. The Tekscan sensor (Figure 14) has the characteristic of being small, light, flexible, and with a surface suitable for the application. In addition, it is capable of withstanding very high forces (Appendix B.1,B.2).

Figure 13: Pressure foot sensor built with two FSR

For the realization of the pressure sensor (Figure 13), 2 FSR sensors were used, attaching them to the insole in a way as to come in contact with the heel and forefoot areas. This was then covered with insulating tape after opportunely connecting the sensor pins to the connect wires necessary for connecting the sensor to the rest of the circuit.

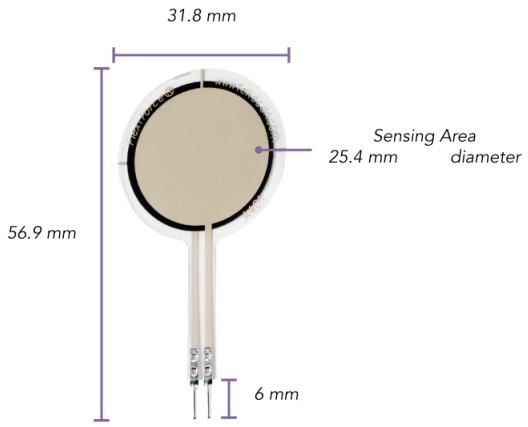

Figure 14: Large Force Sensing Resistor FlexiForce©A401

The use of a pressure sensor for the purpose of detecting assistance phases is an accurate technique both because of the fidelity between the phases of lower or higher pressure exerted and the gait phases and because of the responsiveness of the sensors. However, walking abnormalities in CP patients could be a limitation to the correct detection of some gait phases, as the foot of the crouch gait affected limb does not often rest correctly. In fact, while the toe touches

the ground at each gait cycle, in some cases the heel often does not. In general, a strongly unbalanced pressure distribution is observed. For these reasons the sensor has been designated to be worn below the foot of the leg that is not affected by crouch gait in hemiplegic patients.

2.3.2.1 Preliminary test and Characteristic Curve

This sensor shows an impedance of more than $10M\Omega$ when connected directly to the power supply and when no load is graving on its surface. The resistance value cannot be measured with precision in this condition. It is also difficult to predict a characteristic Pressure-Impedance curve since with no resistance in series the Force range that the sensor is able to measure is really wide.

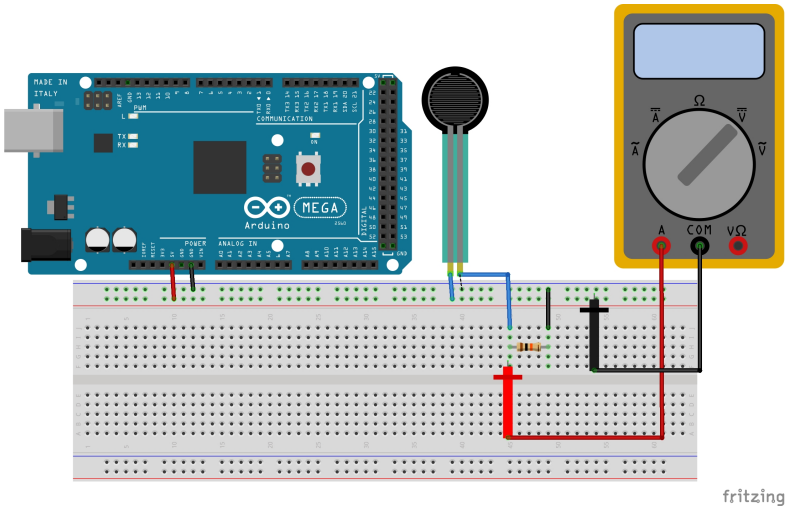

Figure 15: FSR calibration setup

Also, the characteristic curve is sligthly different for every sensor. For this reason the FSR needs to be calibrated. For this procedure, the Arduino Mega 2560 board that will be the final controller board used for this project has been used as positive constant Voltage Source and GND (Ground) connection (Figure 15).

In this case the 5V pin has been chosen since it is the maximum Voltage reference applicable to the FSR. Then, a resistor of $10k\Omega$ has been put in series with the FSR and then connected to the GND.

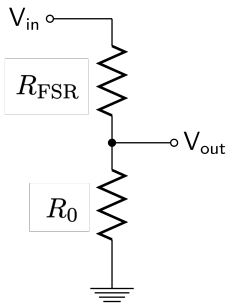

Figure 16: Voltage divider circuit for FSR calibration

$$V_{\text{out}} = V_{\text{in}} \frac{R_0}{R_{\text{FSR}} + R_0} \tag{2.10}$$

where $V_{\text{in}} = 5V$, $R_0 = 10k\Omega$.

A simple Voltage divider has just been mounted (Figure 16), then the V_{out} output Voltage has been measured for different loads applied on the sensor FSR surface through a multimeter and its value has been recorded in order to compute the R_{FSR} values. These latter ones have been obtained from the Voltage measurement and the inverse of the formula (2.10); they are shown in Table V.

TABLE V: FSR Calibration Values

mass (g)	Voltage (V)	Resistance (Ω)
0	0	>10000000 (the value is unmeasurable)
600	0	8798646.3 (measured with Multimeter only)
800	0.05083	973671.1
1000	0.05591	884294.4
4000	0.2542	186695.5

These values have then been used in order to compute the linear fit curve $y = -0,01246 + 0,6128 * 10^{-5}x$ that describes the trend of the characteristic curve mass-Voltage shown in Figure 17 realized with *Origin*© Software.

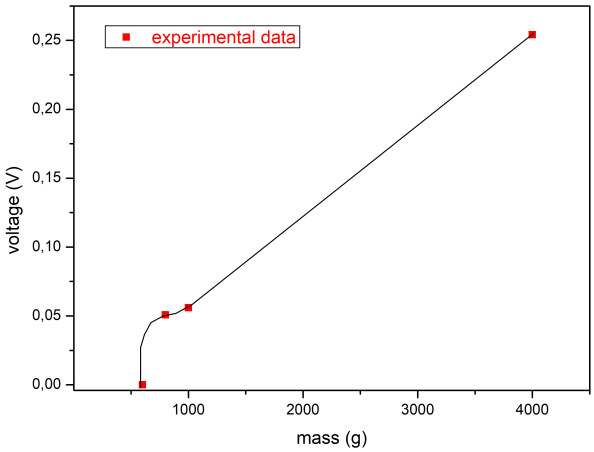

(a) Experimental data

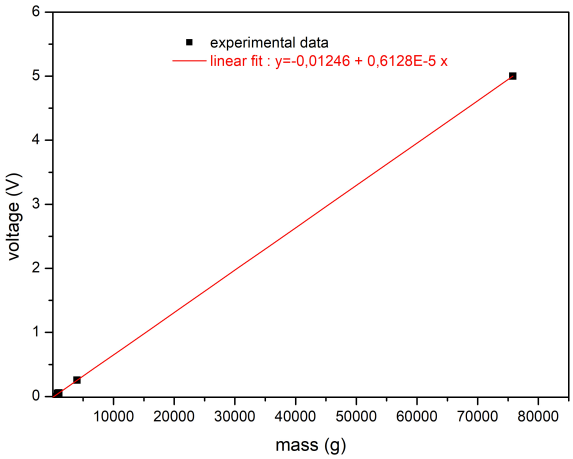

(b) Linear fit

Figure 17: FSR characteristic curve for a R_o of $10k\Omega$

2.3.2.2 Circuit Design - FSR

Since the signal acquired from the FSR sensor is analogue and a resistor put in series is needed in order to choose a proper force range, it is advisable to connect the FSR to an LPF (Low Pass Filter) active circuit. Hence, the pins of the FSR are connected to a negative voltage reference whose possible values are present in the datasheet (Appendix B.2). In this particular case the $V_{\text{ref}} = -5V$ and it has been obtained from a 9V battery whose negative pin has been connected to a Voltage divider circuit that reduces the voltage.

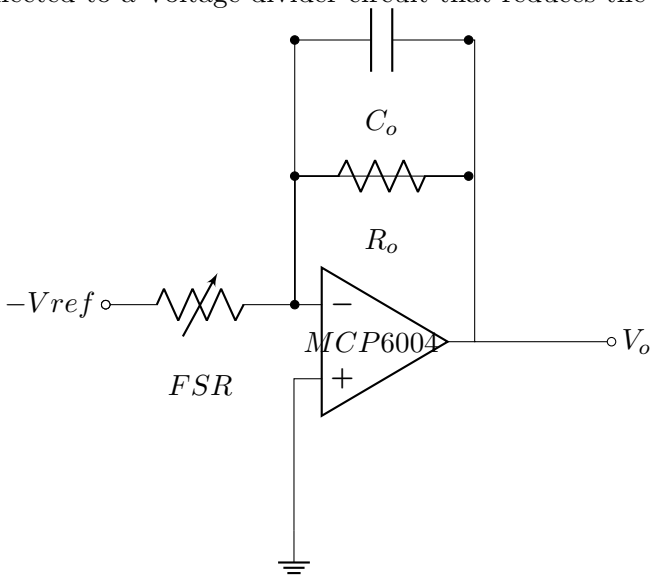

Then, the LPF circuit is mounted as shown above, and the resistor and capacitor values are chosen in order to guarantee a cut-off frequency appropriate to the application. Moreover, the resistor value is chosen in order to have a characteristic curve mass-Voltage close to the one obtained experimentally. The MCP6004 has been chosen, since it is a chip that groups 4 different operational amplifiers, accepts DC voltages as input and has a power supply positive

voltage of 5V. This allows the connection of both FSR to the chip and it can also be powered up by the microcontroller directly.

$$A_{\mathrm{DC}}gain = \frac{R_0}{R_{\mathrm{FSR}}} \tag{2.11}$$

$$f_{\,\mathrm{cutoff}} = \frac{1}{2\pi R_0 C_0} = 159,23Hz \tag{2.12}$$

where $R_0 = 10k\Omega$, $C_0 = 100nF$, $V_{\mathrm{ref}} = -5V$.

Finally, the circuit output is connected to the controller board through 18 AWG electrical coated cable in order to isolate the signal from disturbances.

2.3.3 Potentiometer

The Potentiometer, or angular sensor, is needed in order to predict the shift from one gait phase to the other in cooperation with the pressure foot sensor. It is designed to be mounted in correspondence of a rotational joint, this is why it is designed with an hollow shaft. The specific one used in this project is the high precision hollow-shaft rotary sensor. It has an impressive high resolution, that is under the 0,1°. Its electrical angle is equal to 150°, which means that larger angles will be read equal to 150°.

For the application this electrical angle is more than enough as it exceeds the maximum flexion angle possible in case of a normal walking activity. Furthermore, angles major than a certain value are characteristic of the same gait phase, so the important aspect that has been taken into account is that low values have to be recorded properly by the sensor.

Figure 18: Potentiometer from Contelec©

2.3.3.1 Circuit design - Potentiometer

A passive Low Pass Filter with a low cut-off frequency has been implemented in order to obtain a smoother output signal to be connected to the control board.

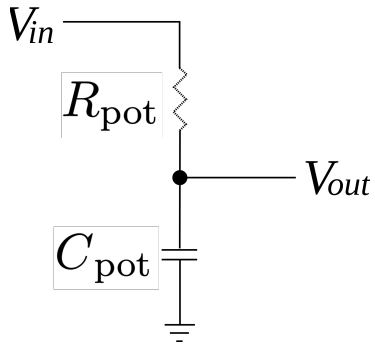

Figure 19: Angular sensor circuit. The Vout pin is connected to the central output pin of the sensor

The central output pin of the sensor is connected to V_{out} in Figure 21, while the other two pins are connected respectively to the 5V voltage source and to the GND.

$$A_{\mathrm{DC}} gain = 1 \tag{2.13}$$

$$f_{\mathrm{cutoff}} = \frac{1}{2\pi R_{\mathrm{pot}} C_{\mathrm{pot}}} = 3,62 Hz \tag{2.14}$$

where $R_{\mathrm{pot}} = 2k\Omega$; $C_0 = 22\mu F$

The C_0 and R_0 have been chosen in order to have a low cut-off frequency close to DC. The Gain of the circuit in pass band region is equal to 1, so that the magnitude of the input signal is not attenuated by the filter.

2.3.3.2 Mounting and preliminar test

In order to look at the potentiometer offset and functioning a preliminary test was conduced, during which the potentiometer has been the only sensor to be mounted and its output signal has been the only one to be measured. As mentioned in the previous section, the sensor has been mounted in correspondence of the joint, taking advantage of the mechanical support previously illustrated at section 2.1.2.

As the first step, the signal has been recorded while the leg was fully extended in standing-up position. Then, some simple flexions have been performed in order to verify the correct functioning of the potentiometer. An offset angle equal to 66,86° has been recorded while the orthosis is held in a straight position, with no flexion applied. For design needs, this offset is too high to be neglected and has to be taken into account in the signal processing part of the

Figure 20: Preliminar test with Potentiometer mounted on the orthosis

control algorithm (see Chapter 3). The Simulink code was subsequently modified by adding a signal correction that deletes the initial offset. After the offset correction, the signal has been recorded during a slow-paced walk performed by a healthy subject. The result is shown in Figure 21.

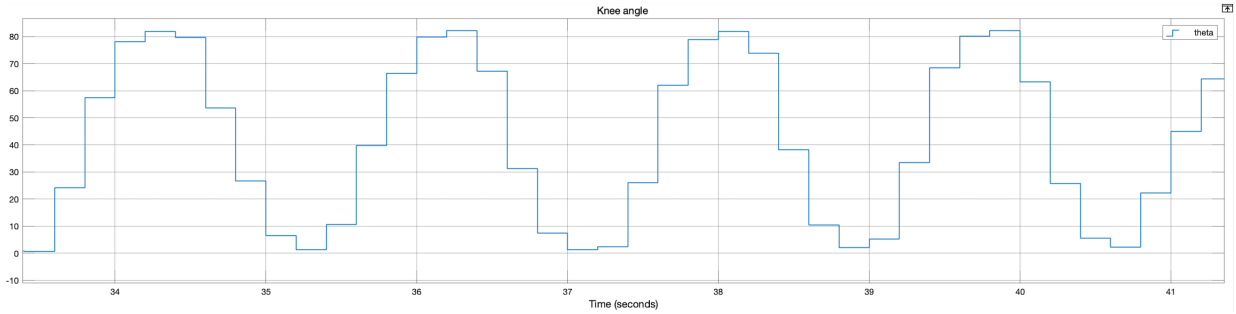

Figure 21: Preliminary test output with Potentiometer after offset correction

2.3.4 Final Hardware mounting

Figure 22 shows the final hardware setup, considering the sensors, their relative circuits and their connections to the controller. The board that has been chosen is Arduino Mega 2560. This choice is due to several reasons, including ease of implementation, the ability to easily connect analog sensors and integrated circuits, the compactness and lightness, the possibility of being able to program it through the tool C-code generation of MATLAB / Simulink, the possibility of generating a command PWM output signal with which to communicate with the servodriver. However, there are limitations given by the power, clock time and flash memory,

as well as the number of pins. A future implementation should take into account the possibility of investing in a more powerful controller.

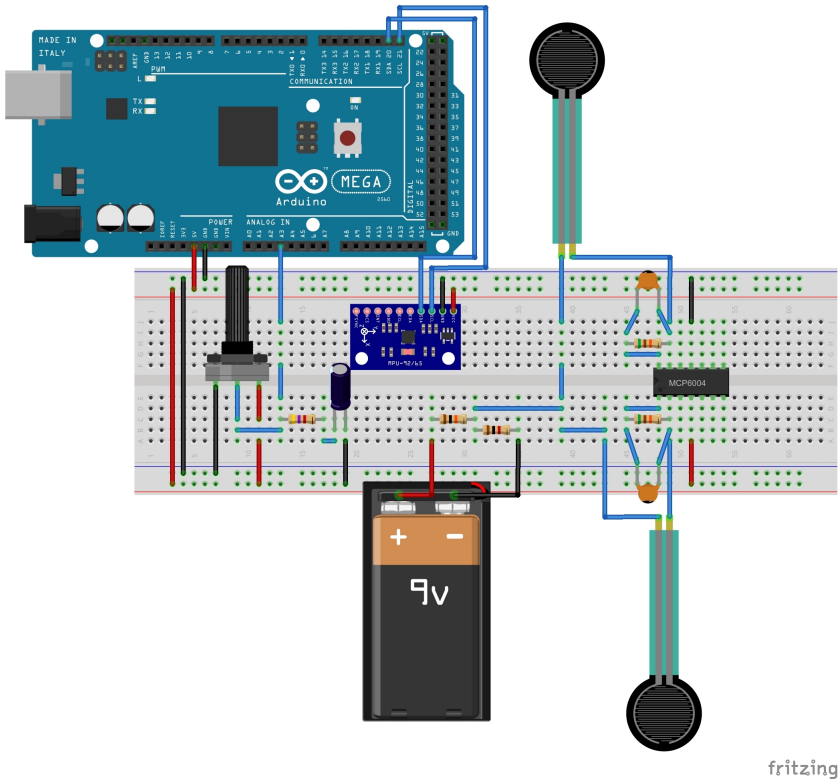

Figure 22: Electronic components mounted in their final configuration

2.4 Overall electromechanical system

The Figure 23 shows the communication paths between all the electromechanical devices of the exoskeleton. ESCON 50/5 is the Maxon$_{©}$servocontroller chosen as servodriver for this project. It operates as a velocity PID controller and it is programmable through its own software that has the possibility of selecting the motor and gearhead from Maxon$_{©}$company for a better performance. The rotational Encoder listed has the function to connect the BLDC motor to the servodriver, creating a closed loop branch that allows the motor speed control. Its presence is mandatory when a BLDC motor is used, as mentioned in section (2.2.1). The rest of the components in the block diagram have been covered in earlier sections of this chapter.

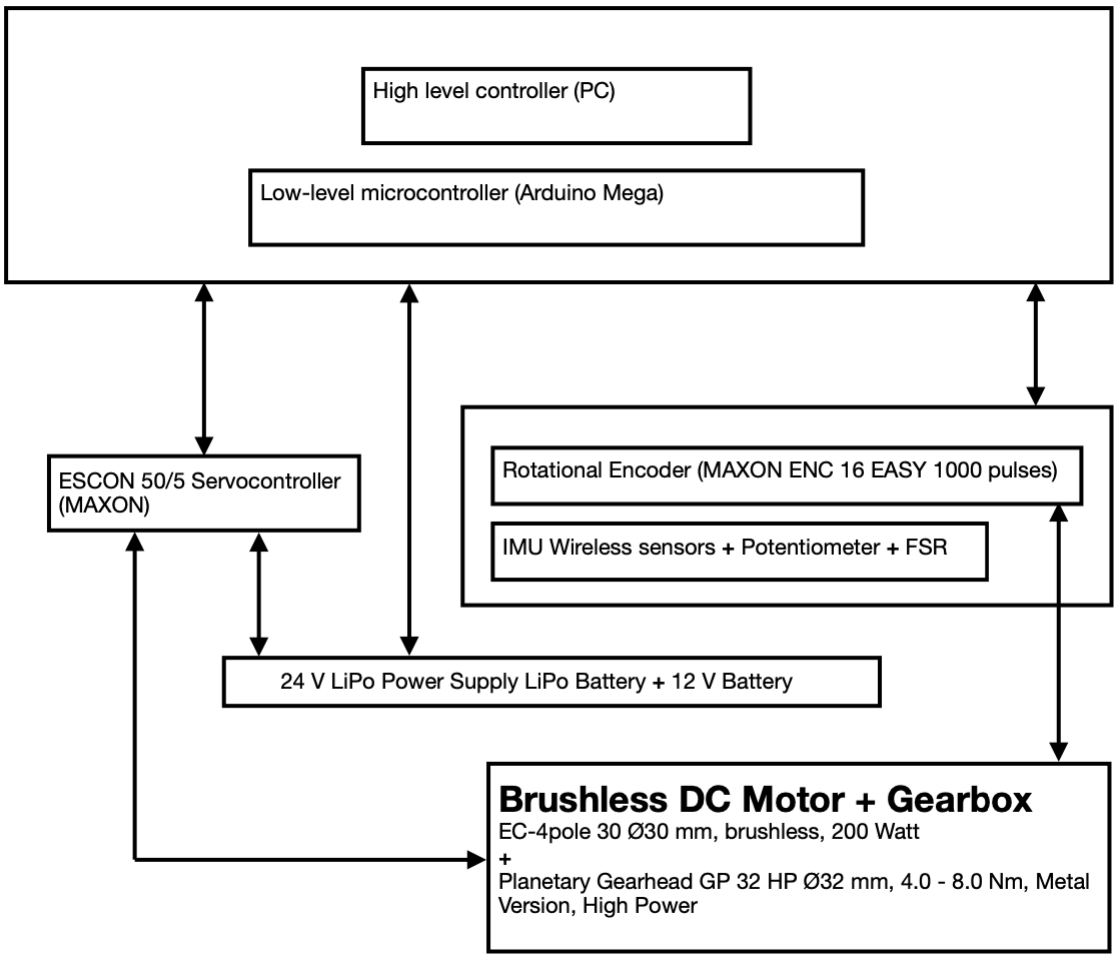

Figure 23: Block diagram showing connections and communication patterns between all the active components of the exoskeleton

CHAPTER 3

CONTROL STRATEGY

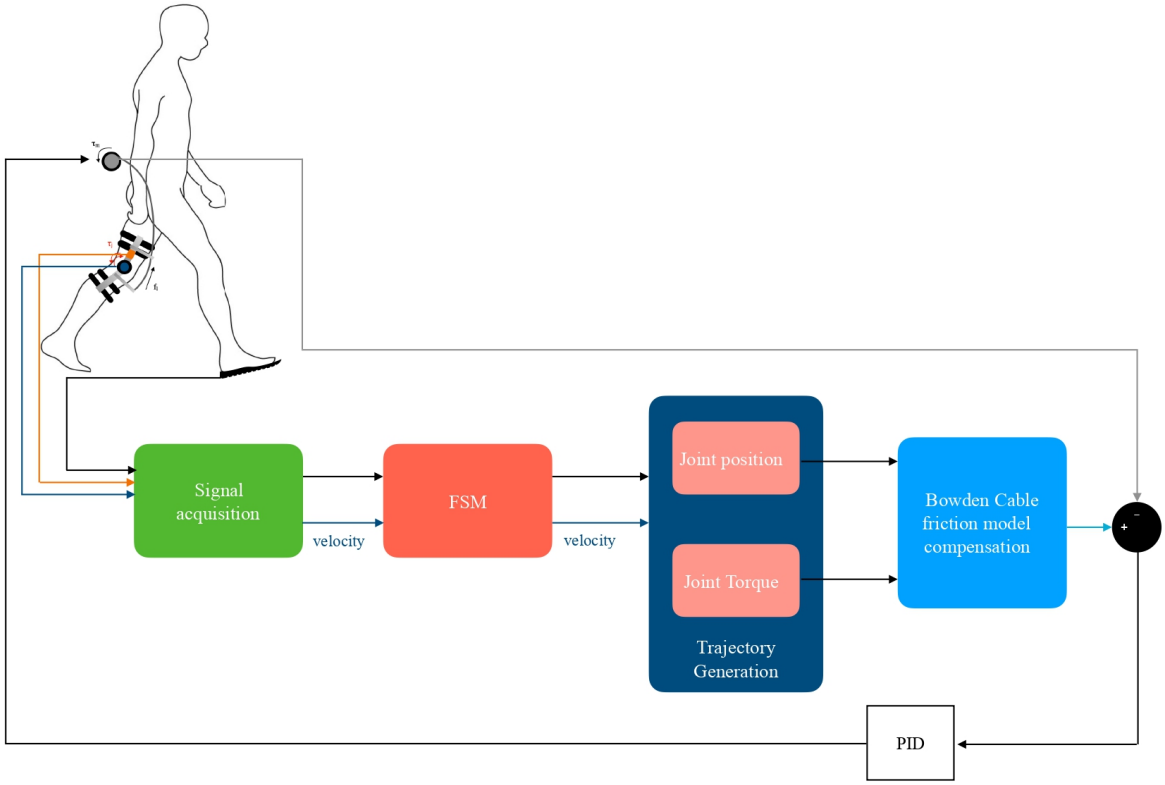

Figure 24: Control strategy block scheme representing the main blocks of the algorithm and connection patterns between the subject and the controller parts

The difficulty associated with Bowden cable-type actuation system is the formulation of a model that can be employed in the control strategy. In addition, the exoskeleton taken under consideration was designed around an already constructed orthosis whose design characteristics are unknown. Given the many unknown factors, it is approximate to formulate a control strategy based on the mechanical response of an inertial model of exoskeleton, human body, and human-robot interaction.

In order to account for the presence of the Bowden cable and the actuation system, the model presented in section (2.2.3.1) was used in the generation of the reference output signal that serves as the control signal for the motor.

The remaining part of the algorithm relies heavily on the detection of real-time signals picked up by the present sensors and the reverberation curves for angular displacement and knee joint torque recorded from healthy walking patients.

The entire control strategy was designed in MATLAB/Simulink.

The C-code has been generated from MATLAB codes and Simulink blocks combined together in a unique algorithm through the Code Generation tool. In the final application of the project, the PID controller is regulated and powered by the MASCON 50/5 servodriver.

3.1 High level control

The high level control is composed of the parts of the algorithm that are strongly related to the external inputs and to the subject's actions while wearing the exoskeleton.

Hence, the code related to the sensors' signals reading, filtering and processing is part of this section. Each algorithm part related to a specific sensor is described and shown in the following.

3.1.1 Sensor reading: FSR and Potentiometer signals

The first sensors to be read are the two FSR.

The signal is read from the sensor and then passed to the 10-bit Analog-to-Digital (A/D) converter. Since this latter one maps the analog signal between 0 and the operating voltage (which in this case is equal to 5 V) into an integer value from 0 to 1023, the input value read by the controller is converted into the initial range again in order to simplify its interpretation.

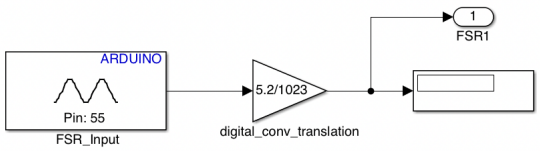

Figure 25: Analog reading block from Arduino Simulink Support Package and gain block needed to map the digital signal value into the analog value range

A similar conversion is related to the potentiometer signal, but in this case the analog range in which the input has to be reconverted is between 0° and 150°, which is the electrical angle

value. After the conversion in degrees, the knee angle value is derived through a discrete-time derivation block and saved through a memory block. These two actions are fundamental for the correct implementation of the FSM, since the angular velocity and its previous instant value are required.

3.1.1.1 Finite State Machine

The read signals enter into a Stateflow diagram in which each state represents a gait phase. The criteria for passing from one state to another are relative to angle and voltage limits for the potentiometer and foot pressure sensor signals, respectively. The function of the FSM is to initially determine the gait phase at which the patient is and consequently the need for active assistance.

FSMs are a fundamental part of assistive exoskeletons, several have been devised [37] and are in most cases dependent on sensors' signals.

Their importance lies not only in the detection of the correct phase during which it is necessary to provide assistance, but also in the choice of the type of therapy provided.

In the case of patients with cerebral palsy, specifically for lower limb exoskeletons, the phases during which it is possible to choose to provide assistance are complementary.

In fact, as seen in Chapter 1, the motor curve representing the flexion of the knee joint is different from the expected one, both in terms of maximum peak of flexion angle and minimum point of extension angle.

Therefore, the choice of providing assistance during the initial swing phase in order to assist

the knee exclusively in the flexion phase could be evaluated.

On the contrary, another approach concerns the assistance given during the stance and final swing phases with the aim of assisting the knee joint in the completion of the extensor act. This second option considers the possibility that bringing the curve representing the spaced angle between the upper and lower leg during the walk within the expected extension values, will naturally help the patient in the flexion act as demonstrated in several studies that have chosen to apply this assistance strategy[23][24].

FSMs are mainly related to sensor signals in the exoskeleton, considering that they are the most instantaneous method of determining gait status.

The design choice made in this project was to combine the signals from FSR and potentiometer in order to increase the detection accuracy.

Moreover, since in hemiplegic patients the crouch gait affected leg has a foot pressure distribution that is not faithful to the expected, the foot sensor is worn on the side that is unaffected by spasticity. Hence, the gait phases are related to the leg that needs assistance and takes into account the knee angle from the leg wearing the brace and the pressure values obtained from the other foot. The FSM designed is conceived for the determination of the instants of heel strike, beginning of the final stance flexion phase and beginning of the mid-final swing extension phase.

Figure 26 shows the states and the flow that determines the transition from one to the other. The thresholds relative to the potentiometer were identified from the mean values of the knee angle curves during walking of healthy subjects.

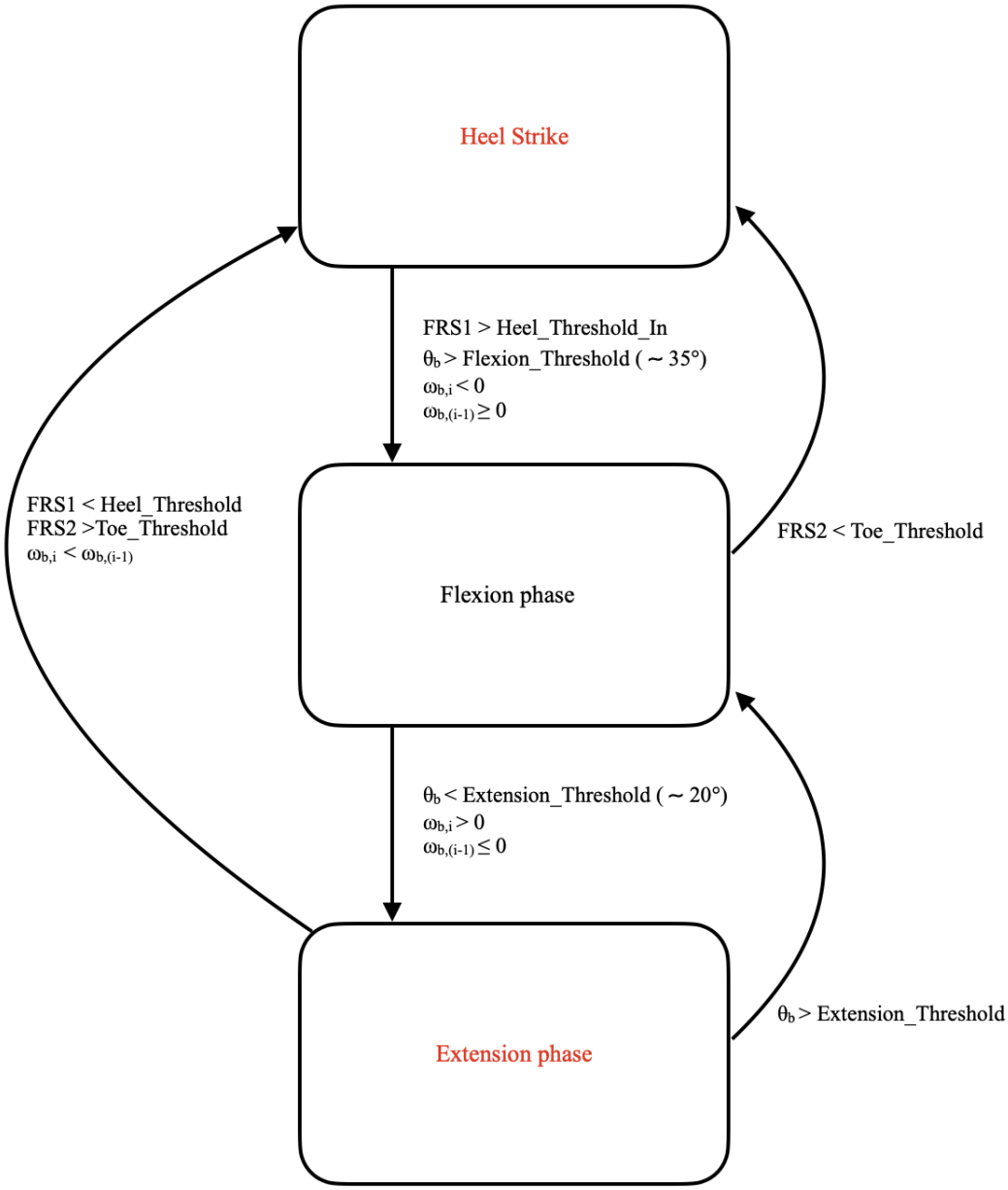

Figure 26: Finite State Machine

The thresholds of sensors FSR1 (i.e. sensor on which the heel rests) and FSR2 (i.e. sensor on which the forefoot rests) should be customized according to the patient, as a percentage of their body weight. Specifically:

- $HeelThresholdIn = \frac{5 \cdot 35\% \cdot m}{75,79}$;
- $ToeThreshold = \frac{5 \cdot 25\% \cdot m}{75,79}$;
- $HeelThreshold = \frac{5 \cdot 20\% \cdot m}{75,79}$.

Where m is the body weight of the patient and 75,79 is the maximum measurable weight in kg considering the characteristic curve of the circuit (Figure 17b). The thresholds' names are relative to the ones present in Figure 26.

These percentages were obtained by conducting an initial test during which the insole alone was worn by a healthy subject while walking. The voltage values during the transitional phases of the walk, such as support of the whole sole of the foot, support of the heel only and transition from total support to the toe only were recorded and consequently related to the body mass in percentage according to the characteristic curve obtained in Figure 17. The FSM present in Figure 26 reflects the Stateflow block implemented in Simulink. Looking at Figure 2 it is possible to follow the gait phases associated to the weak leg. The colored dots attached to the leg unrelated to the gait cycle represent FSR1 and FSR2. The Heel strike state is considered as the starting point of the gait cycle (time instant t_0=0). It starts with the weak leg heel strike and it is associated to an increasing pressure on the opposite leg toe and decreasing pressure on the opposite leg heel. Furthermore, the knee angular velocity is in decrease. During this phase the assistance is required. The transition between the Heel Strike state and the Flexion phase

occurs when the FSR2 signal from the heel becomes higher than the relative threshold, the knee angle measured is above the flexion threshold and the knee angular velocity changes in trend (turns from positive to negative). This happens at approximately the 60% of the gait cycle. This state corresponds to no assistance given. When the knee angle goes below the extension threshold and its angular velocity changes in trend from negative to positive, the Extension phase begins. This happens at approximately the 87% of the gait cycle. It corresponds to the late swing phase, and the assistance is now required. If the events typical of the Heel strike happen, the gait cycle restarts.

3.1.2 IMU reading: velocity estimation algorithm

The IMU signal is read through I^2C communication, thus the tool given by MATLAB Arduino Support Package that allows the connection and reading on the sensor in real time is used.

Its function is to estimate the patient's walking speed using the detected linear acceleration and angular velocity around the axes.

The sensor is placed on the metal part of the brace at the height of the lower thigh, above the knee, so as to ensure a stable base that minimizes oscillations and therefore measurement errors.

The position is instead related to the algorithm chosen for the calculation of the estimated speed, as detailed below.

This section of the algorithm starts with a MATLAB Code (Appendix C) that allows the first signal processing step. Accelerations along x- and y-axes are read, as well as angular ve-

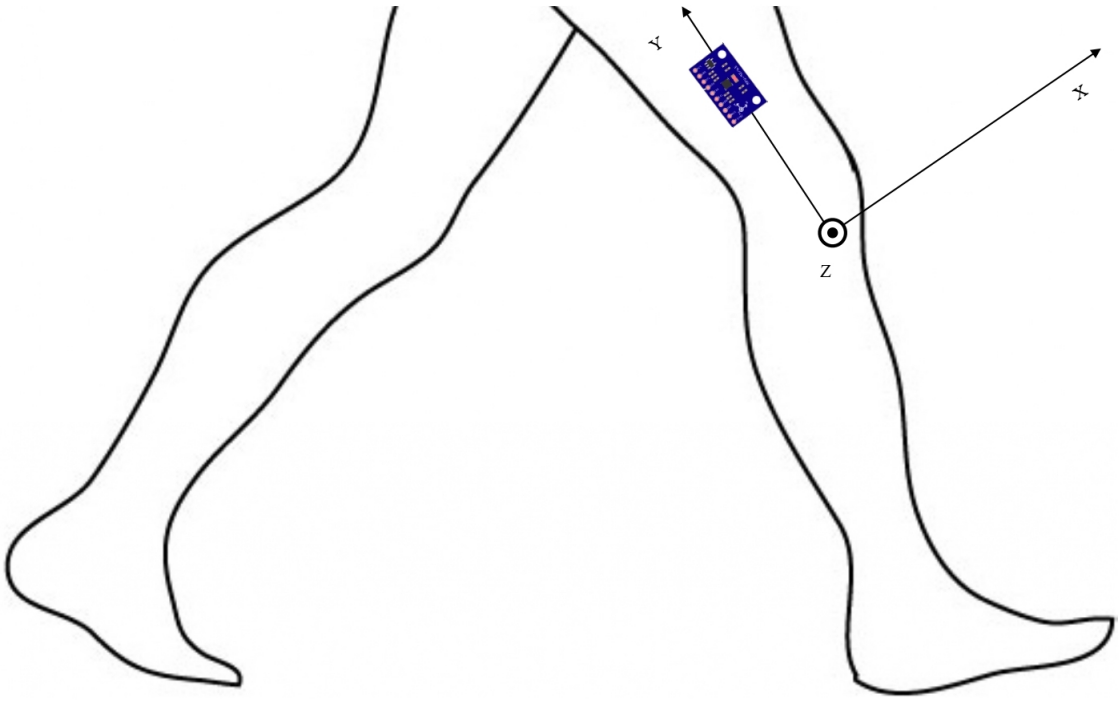

Figure 27: IMU Sensor positioned on the leg

locity around the z-axis, in real time. The reference to the axes can be found in Figure 27. The offset is measured and subtracted from the output signals after an initial calibration step. A Kalman filter is then used to fuse the accelerometer and gyroscope signals in order to estimate the y-axis orientation angle, denoted as θ in the drawing in Figure 28.

3.1.2.1 Inverted Pendulum model

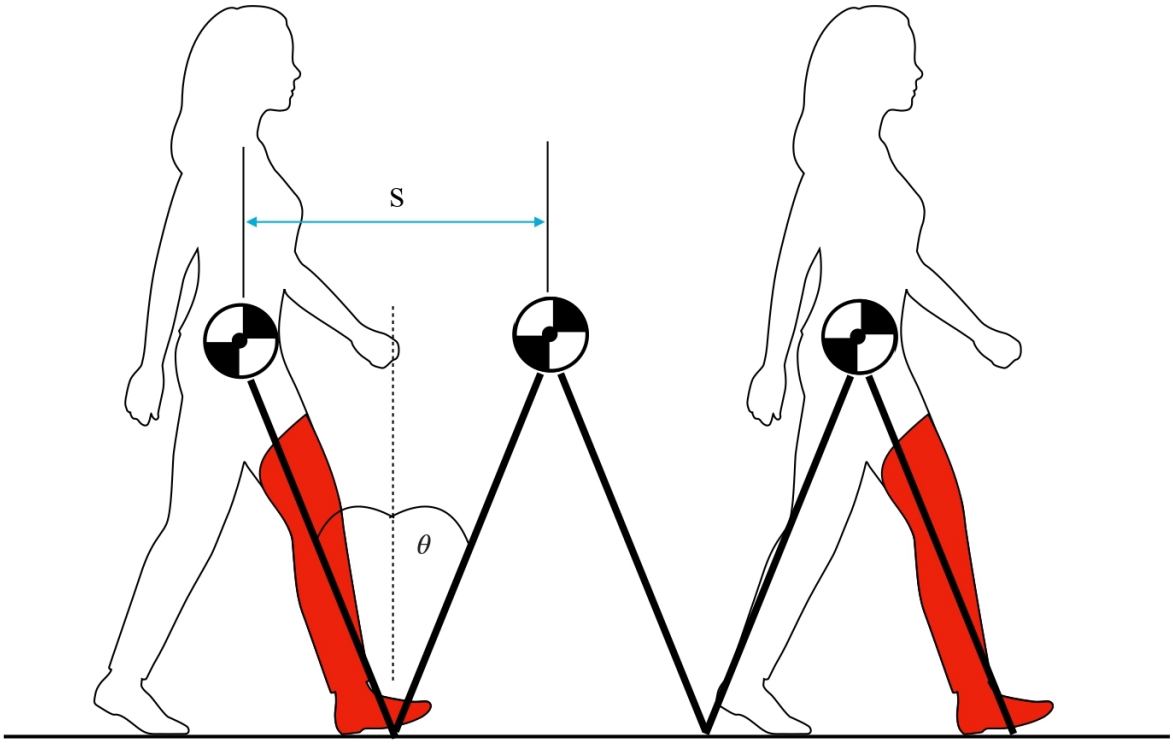

Figure 28: Inverted Pendulum gait approximation

Inertial sensors have been used in several studies to determine temporal parameters of gait[40], placed in different parts of the body.

Usually a network of sensors is used in order to calculate more accurately features such as walking frequency and stride length. In this case, more complex models describing the human body can be used because of the presence of a greater amount of acquired data that decreases the number of unknown parameters and gives the possibility to use more sophisticated human body models.

Another aspect that has to be taken into account about the spatio-temporal gait parameter estimation is the fact that the accuracy in speed estimation is flanked by the limitation of being subject-specific in terms of calibration[41]. An alternative to the indirect spatial parameters estimation is the displacement determination directly from the integration of the signals read from the IMU sensor. Placing it on the thigh of the stance leg, the subject velocity can be estimated using the inverted pendulum model. In this gait description, the mass is concentrated at the level of the hips, constituting a center of mass (CoM) of the entire human body, and oscillates by performing a motion approximating the one of the leg (Figure 28).

It has been demonstrated to be a faithful approximation of the gait cycle[38]. More complex models, consisting of an inverted pendulum with a hinge in between, have shown similar results to the simpler inverted pendulum[39].

The objective is to compute the strade length S and divide it for the gait cycle period T.

The first step is computing the tangent and normal accelerations (respectively a_{t} and a_{n}) values. They are respectively parallel and perpendicular to the ground. In formula:

$$a_{\mathrm{t}}(t) = -a_{\mathrm{y}}(t)sen\theta(t) + a_{\mathrm{x}}(t)cos\theta(t) \tag{3.1}$$

$$a_{\mathrm{n}}(t) = a_{\mathrm{y}}(t)cos\theta(t) + a_{\mathrm{x}}(t)sen\theta(t) - g \tag{3.2}$$

Where g is the gravitational acceleration, θ is the rotation angle of the y-axis about the origin of axes, a_{x} and a_{y} are the accelerations read respectively along the x- and y-axes through the IMU sensor. In order to obtain θ, a Kalman Filter for orientation estimation is used (see section 3.1.2.3).

After obtaining the two accelerations values, the normal and tangential velocities (respectively v_{t} and v_{n}) are computed integrating the accelerations' values:

$$v_{\mathrm{t}}(t) = \int_0^t a_{\mathrm{t}}(\tau)d\tau + v_{\mathrm{t}}(0) \tag{3.3}$$

$$v_{\mathrm{n}}(t) = \int_0^t a_{\mathrm{n}}(\tau)d\tau + v_{\mathrm{n}}(0) \tag{3.4}$$

Where $v_{\mathrm{t}}(0)$ and $v_{\mathrm{t}}(0)$ are the initial tangential and normal velocity values. In the case of this algorithm, they are equal to 0.

Moving forward, the tangential and normal displacement (respectively s_{t} and s_{n}) are computed.

$$s_{\mathrm{t}}(t) = \int_0^t v_{\mathrm{t}}(\tau)d\tau + s_{\mathrm{t}}(0) \tag{3.5}$$

$$s_{\mathrm{n}}(t) = \int_0^t v_{\mathrm{n}}(\tau)d\tau + s_{\mathrm{n}}(0) \tag{3.6}$$

Where $s_{\mathrm{t}}(0)$ and $s_{\mathrm{t}}(0)$ are the initial tangential and normal displacement values. In the case of this algorithm, they are equal to 0.

In order to calculate the stride length, it is necessary to identify a gait event that marks the beginning of a cycle. The instant in which the leg on which the sensor is mounted is in a vertical position with respect to the ground during the stance phase has been chosen. The angle crosses the zero going from a negative to a positive value. Each time this event is detected, the period T is updated.

The displacement offsets are estimated:

$$s_{\mathrm{t}}{}^{\mathrm{offset}} = \frac{1}{2} a_{\mathrm{t}}{}^{\mathrm{offset}} T^2 = \frac{1}{2} v_{\mathrm{t}}(T)T \tag{3.7}$$

$$s_{\mathrm{n}}{}^{\mathrm{offset}} = \frac{1}{2} a_{\mathrm{n}}{}^{\mathrm{offset}} T^2 = \frac{1}{2} v_{\mathrm{n}}(T)T \tag{3.8}$$

and the stride length S is computed as:

$$S = \sqrt{(s_{\mathrm{t}}(T) - s_{\mathrm{t}}{}^{\mathrm{offset}})^2 + (s_{\mathrm{n}}(T) - s_{\mathrm{n}}{}^{\mathrm{offset}})^2} \tag{3.9}$$

Finally, the average walking gait cycle speed is computed:

$$V(T) = \frac{S(T)}{T} \tag{3.10}$$

This value is used in the following algorithm steps in order to choose the assistance rate and, consequentially, the reference trajectory that best fits the requirements.

3.1.2.2 Filtering: accelerations x and y

Before the velocity calculation, the accelerometer signals are filtered through a Median Filter [42].

The latter is a nonlinear filter in which each output sample is computed as the median value of the input signals under a certain window of length N. Such a digital filter reduces random noise signals and is typically used as signal pre-processing.

3.1.2.3 Angular position around z - Kalman Filter Estimation algorithm

Measuring leg inclination θ with respect to the axis normal to the ground proves to be more difficult.

One possible option is to integrate the gyroscopic signal ω_z which represents the speed of rotation about the z-axis.

Another possibility is instead to merge the accelerometer and gyroscope signals and estimate the axis orientation using a Kalman filter[43].

Through some initial measurements it was possible to verify that the second method proved to be more accurate in detecting the beginning of a new gait cycle and consequently also in terms of calculation of the period T.

The Kalman filter models the desired vector in exam as linear and recursive. It can be generally represented as:

$$x_k = A_k x_{k-1} + w_k \tag{3.11}$$

Where x_k has N degrees of freedom and consequentially, A_k is an NxN linear prediction matrix (possibly time-varying), while w_k is an Nx1 noise vector.

The vector x_k is assumed to be unmeasurable directly, hence it has to be estimated from the measurable vector z_k, linearly related to x_k as follows:

$$z_k = C_k x_k + v_k \tag{3.12}$$

Where z_k has N degrees of freedom and C_k is an NxN matrix (possibly time-varying), while v_k is an Nx1 noise vector.

Noise vectors are assumed to be zero mean white noises, hence:

$$E[w_k] = 0 \tag{3.13}$$

$$E[v_k] = 0 \tag{3.14}$$

$$cov\{w_k, w_j\} = E[w_k w_j^T] = Q_{w,k}\delta_{kj} \tag{3.15}$$

$$cov\{v_k, v_j\} = E[v_k v_j^T] = Q_{v,k}\delta_{kj} \tag{3.16}$$

Where $Q_{w,k}$ and $Q_{v,k}$ are covariance matrices that are symmetric by definition.

The objective of the Kalman filter is to compute an unbiased *a posteriori* estimate $\hat{x}_k^+$ of the signal x_k, from the previous iteration's *a posteriori* estimate $\hat{x}_{k-1}^+$ and the current measurement z_k. In formula,

$$\hat{x}_k^+ = K'_k \hat{x}_{k-1}^+ + K_k z_k \tag{3.17}$$

The time-varying Kalman gain matrices K'_k and K_k define the relative weightings given to the previous iteration's Kalman filter estimate and to the current measurement. If the measurements' noise is low, its relative term in the equation above will weight more than the term relative to the *a posteriori* estimation and viceversa. The Kalman filter is therefore a time varying recursive filter.

The general Kalman Filter equations are: The *a priori* estimate is defined as the application of the linear prediction matrix to the previous *a posteriori* estimate;

$$\hat{x}_k^- = A_k \hat{x}_{k-1}^+ \tag{3.18}$$

The *a priori* error covariance matrix P_k^- is updated using the model matrix A_k and the noise matrix $Q_{w,k}$;

$$P_k^- = A_k P_{k-1}^+ A_k^T + Q_{w,k} \tag{3.19}$$

The Kalman Filter gain matrix K_k is updated as:

$$K_k = P_k^- C_k^T (C_k P_k^- C_k^T + Q_{v,k})^{-1} \tag{3.20}$$

The Kalman filter *a posteriori* estimate is computed from the *a priori* estimate and actual measurement;

$$\hat{x}_k^+ = \hat{x}_k^- + K_k(z_k - C_k\hat{x}_k^-) = (I - K_k C_k)\hat{x}_k^- + K_k z_k \tag{3.21}$$

The *a posteriori* error covariance matrix P_k^+ is updated;

$$P_k^+ = (I - K_k C_k)P_k^- . \tag{3.22}$$

The equations related to this particular algorithm are:

$$x_k^- = 0 \tag{3.23}$$

$$Q_k = P_k^- \tag{3.24}$$

$$x_k^+ = K_k z_k \tag{3.25}$$

and the equations (3.20),(3.22). The k represents the current iteration, while the $^+$ superscipt represents *a posteriori* estimate, and the $^-$ superscipt represents *a priori* estimate.

The following diagram shows the algorithm structure:

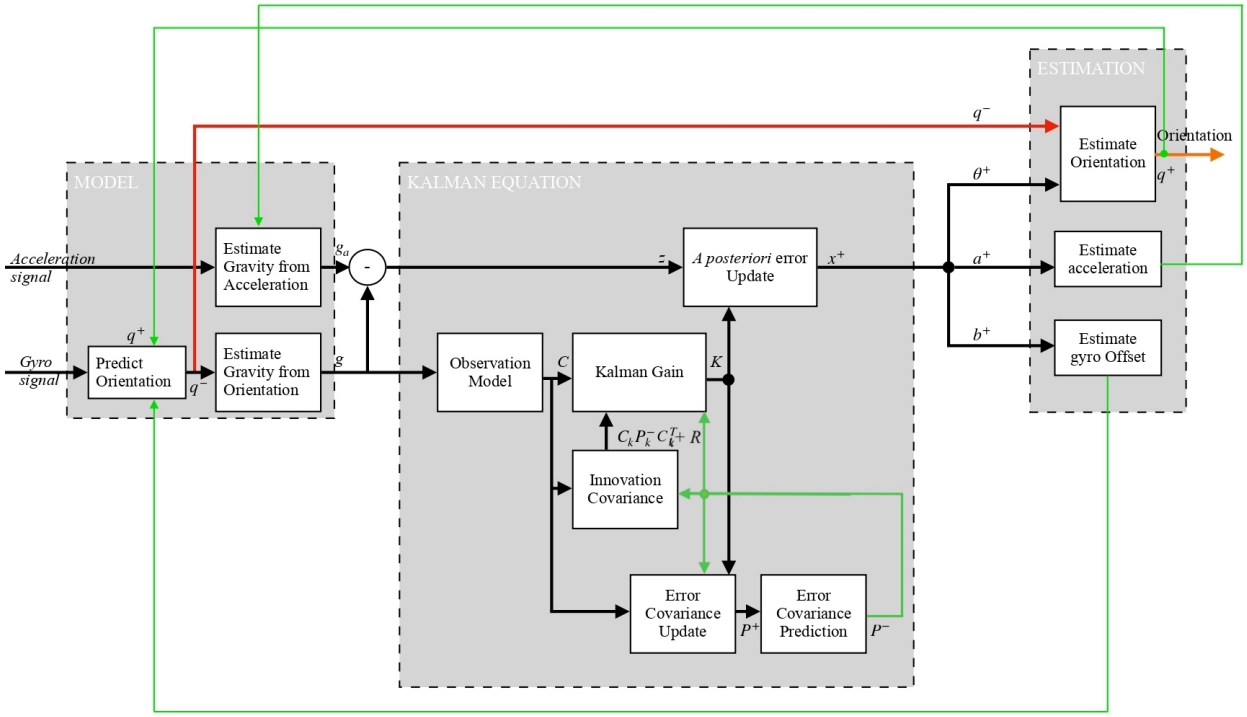

Figure 29: Kalman Filter block system for orientation estimation algorithm

The algorithm structure computes the orientation as follows: The angle variations are modeled as linear processes. The orientation for the actual frame is predicted by a primary estimation of the angular change from the previous frame that is followed by a conversion in quaternions.

$$\Delta\phi_{Nx3} = \frac{gyroSignal_{Nx3} - gyroOffset1x3}{f_s} \tag{3.26}$$

where f_s is the sample rate;

$$\Delta Q_{N+1} = quaternion(\Delta\phi_{Nx3}) \tag{3.27}$$

Then, the previous orientation is updated.

Gravity is estimated from both orientations, as the third column of the quaternium q^-:

$$g_{q,1x3} = (rPrior(:,3))^T \tag{3.28}$$

and acceleration, by the subtraction of the prior linear acceleration estimate from the acceleration signal read:

$$g_{a,1x3} = AccelSignal_{1x3} - Accelprior_{1x3} \tag{3.29}$$

The error is then computed as the difference between the two estimated gravity vectors:

$$z = g_{q,1x3} - g_{a,1x3} \tag{3.30}$$

The gravity estimate from gyroscope signal $g_{q,1x3}$ and the error z are used to update the Kalman gain K and the covariance matrices. The Observation model (Figure 29) maps the observed $g_{q,1x3}$ in the following 3x9 state:

$$C = \begin{bmatrix} 0 & g_z & -g_y & 0 & -\kappa g_z & \kappa g_y & 1 & 0 & 0 \\ -g_z & 0 & g_x & \kappa g_z & 0 & -\kappa g_x & 0 & 1 & 0 \\ g_y & -g_x & 0 & \kappa g_y & \kappa g_x & 0 & 0 & 0 & 1 \end{bmatrix} \tag{3.31}$$

where $\kappa = \frac{decimation factor}{sample time}$. The innovation covariance matrix has the objective of tracking the measurements' variability. It is equal to $C_k P_k^- C_k^T + R$, where C_k is the observation model, P the *a priori* covariance estimation computed during the prior iteration and R is the model noise covariance, equal to:

$$R = (\lambda + \kappa(\beta + \eta) + \psi) \begin{bmatrix} 1 & 0 & 0 \\ 0 & 1 & 0 \\ 0 & 0 & 1 \end{bmatrix} \tag{3.32}$$

where β is gyroscope drift noise, η the gyroscope noise, λ the accelerometer noise and ψ the linear acceleration noise.

The estimation error covariance matrix is updated as shown in equation (3.22). The Kalman gain K has the objective of weighting the innovation. His construction is shown in equation (3.20). The Kalman filter is also applied to the error z in order to determine the *a posteriori* error x^+ (Equation 3.25).

Finally, the prior orientation estimate, the linear acceleration and the gyroscope offset vectors are updated. The orientation is updated multiplying the previous estimated value by the *a posteriori* error;

$$q^{+} = q^{-}\theta^{+} \tag{3.33}$$

The previous acceleration estimate is multiplied by the decay factor and then subtracted by the *a posteriori* error;

$$Accelprior = Accelprior^{-}\nu - b^{+} \tag{3.34}$$

the prior gyroscope offset is simply subtracted by the *a posteriori* error.

$$gyroOffset = gyroOffset^{-} - a^{+} \tag{3.35}$$

3.2 Middle level control

Once the signals are acquired from the sensors, the estimated walking speed is calculated, and the phase of the gait cycle is determined, the reference trajectory must be selected. This algorithm does not provide a single reference signal to control the exoskeleton, but it is automatically chosen by the controller based on the revealed walking speed.

In addition, the shape of the reference is not based on any periodic signal, but it is the result of interpolation between third- or fifth-degree polynomials calculated to be faithful to signals detected from healthy subjects. Reference trajectories for torque and knee angle are generated relative to gait velocity and phase. In the case of no need for assistance, the reference trajectories delivered are zero.

Desired torque and joint position are combined together according to the Bowden cable model in such a way that the effect of friction is compensated for. The output signal from the medium level control block represents the desired motor speed.

3.2.1 Trajectory pattern generation

The goal of trajectory planning is to generate the reference input to the motion control system that will ensure that the joint executes the planned trajectory [50].

In this particular case, the trajectory is planned in the joint space: a function $q(t)$ is generated by the planning algorithm and describes the joint path in time, referred to as trajectory.

This $q(t)$ function is obtained by the interpolation of some given vectors of joint variables at certain points, following the system constraints. A joint space trajectory planning algorithm

has to be not computationally intensive, it should generate joint position and velocity functions that are continuous and smooth functions in time.

Previously designed exoskeletons and prostheses exploit different techniques in reference signal generation.

Ankle Assistance Exoskeleton [44] implements proportional joint-torque control. The reference torque is calculated as a function of the pressure signal received from the foot force sensor, following a second-degree polynomial function.

The lower leg prosthesis [45] calculates the reference torque signal through an impedance model of the prosthesis, whose stiffness and damping are known.

In the lower limb controller for rehabilitation after stroke [46], the reference torque consists of a sinusoidal signal whose period is proportional to the gait period during the swing phase, while it is based on the gravity compensation model during the stance phase.

Several assistance exoskeletons employ constant signals as reference signals activated periodically or at the time of required assistance[47]. Among them, the exoskeleton designed for children with CP has shown positive text results[23]. However, there is a necessity of employing reference signals close to the physiological ones, especially in the use of kinematic reference signals, as in this case where the rotational speed of the joint will be used.

The interpolation of polynomials of 3^{rd} or 5^{th} degree is a suitable strategy, commonly implemented in planning algorithms. Cubic polynomials guarantee the generation of continuous

position, velocity and acceleration functions. The required constraints only concern the initial and final position and velocity values. No constraint is required for what concerns the acceleration, at the expense of its function, that results to be linear and discontinuous . In case the acceleration constraints are required for the application the initial and final values are nencessary and as a consequence, a polynomial of higher value is needed: this is the case in which a Quintic polynomial trajectory is needed.

In previous studies regarding the control design of lower limb exoskeletons [49] the quintic and cubic polynomial trajectories have been implemented and compared, and the first one has been preferred in terms of continuity, when the data available allows the possibility to have the necessary constraints.

For what concerns the design in exam, joint trajectory is described by a motion through a sequence of points. These points are interpolated through cubic polynomials and quintic polynomials for obtaining the knee angular torque and position respectively. This choice is due to two main reasons. Firstly, obtaining acceleration constraints from torque data turned out to be inaccurate considering the absence of any data of its first derivative. Secondly, original data acquired from knee joint position, velocity and acceleration of healthy subjects is present in literature. Hence, the constraints necessary for the quintic polynomials computation are given.

3.2.1.1 Kinematic and kinetic data collection from healthy patients during walking

In order to obtain the final points from which generating the reference position and torque curves, some data taken from healthy subject during walking are needed. These are essential to impose the sequence of interpolation points and their related constraints.

3.2.1.1.1 Knee joint angular position: Quintic Polynomial Trajectory

Primarily, the knee joint characteristic curve obtained from healthy subjects walking at different speeds is observed [33]. In this study, 36 healthy adult individuals were required to walk at different speeds. Then, their data was collected and put together in a unique mean curve for each walking speed range. As the speed changes, it is noticed that the knee flexion path shape is almost equal, but different in magnitude. Furthermore, identifying a unique curve for different speeds suggests that the knee flexion curve shape remains almost unaltered under a certain walking speed interval. This deduction has been implemented in the project, dividing the velocities in four different intervals and associating a different knee flexion reference curve to each of them. Specifically, the following speed intervals have been chosen:
The second column in Table VI shows how the knee flexion curve magnitude has been adapted for each velocity range. The ratio between the peak value of each curve and the curve relative to the $1,2\frac{m}{s}$ velocity, has been computed. This result has been used as conversion ratio between the reference curve θ_{ref} and the curve related to another velocity range.

TABLE VI: Walking Velocity Ranges, Relative Assistance and Knee Position Curve Proportionality

Velocity range ($\frac{m}{s}$)	$\frac{\theta_i}{\theta_{ref}}$ratio	Related assistance
0,2-0-6	0,90	10%
0,6-0,8	0,95	20%
0,8-1,2	1	30%
>1,2	1,10	40%

θ_{ref} has been computed using an open access database [48]. This database collects kinematic data from 50 different healthy subject and includes also 21 pediatric individuals. In order to obtain the knee position reference curve, only the data from the pediatric patients has been taken into consideration.

During a first selection, 7 of these datasets belonging to the pediatric group have been excluded, for reasons of data quality. The remaining 14 datasets have been used in order to compute a unique set of points.

For each dataset, the points at specific time instants of the gait cycle are taken and then a mean value between the datapoints relative to each time instant is computed. These time instants correspond to the percentage of gait cycle at which specific significant events happen (Table VII).

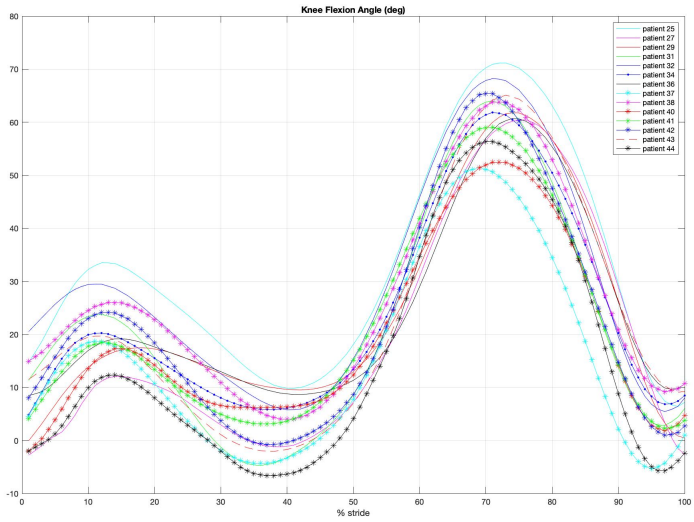

Figure 30: Knee angular position curve from selected healthy pediatric subjects

TABLE VII: Time Instants Chosen for Knee Flexion Curve Segmentation and Datasets for Knee Kinematic Trajectories

Gait percentage	**Gait event**	**Position reference dataset**	**Velocity reference dataset**	**Acceleration reference dataset**
0	Heel strike	7.163	100.840	2323.343
10%	Opposite toe off	18.315	118.602	-2523.301
30%	Heel rise	4.263	-41.825	25.783
50%	Opposite initial contact	13.430	219.442	2294.123
60%	Toe off	36.652	344.920	-1255.923
73%	Feet adjacent	59.941	-154.125	-3902.415
87%	Tibia Vertical	10.050	-422.269	272.727
100%	Heel strike	1.163	100.840	2323.343

The resulting data vector constitutes the points to be interpolated through quintic polynomials. Hence, they represent the via points that give origin to the θ_{ref} curve.

The velocity and acceleration constraints have been obtained by deriving the curves in Figure 30 and taking the resulting values at the appropriate time instants. Being able to specify angular position, velocity and acceleration at each datapoint, the quintic polynomial function $\theta(t) = a_0 + a_1 t + a_2 t^2 + a_3 t^3 + a_4 t^4 + a_5 t^5$ can be obtained for each segment, since the following constraints are always defined:

- initial position $\theta(0) = \theta_0$;
- final position $\theta(t_f) = \theta_f$;
- initial velocity $\dot{\theta}(0) = \dot{\theta}_0$;
- final velocity $\dot{\theta}(t_f) = \dot{\theta}_f$;
- initial acceleration $\ddot{\theta}(0) = \ddot{\theta}_0$;
- final acceleration $\ddot{\theta}(t_f) = \ddot{\theta}_f$.

Applying these six constraints, the following equations arise, allowing the unknown parameters computation:

$$\theta_0 = a_0 \tag{3.36}$$

$$\dot{\theta}_0 = a_1 \tag{3.37}$$

$$\ddot{\theta}_0 = 2a_2 \tag{3.38}$$

$$\theta_f = a_0 + a_1 t_f + a_2 t_f^2 + a_3 t_f^3 + a_4 t_f^4 + a_5 t_f^5 \tag{3.39}$$

$$\dot{\theta}_f = a_1 + 2a_2 t_f + 3a_3 t_f^2 + 4a_4 t_f^3 + 5a_5 t_f^4 \tag{3.40}$$

$$\ddot{\theta}_f = 2a_2 + 6a_3 t_f + 12a_4 t_f^2 + 20a_5 t_f^3 \tag{3.41}$$

The solutions of this six equations system are:

$$a_0 = \theta_0 \tag{3.42}$$

$$a_1 = \dot{\theta}_0 \tag{3.43}$$

$$a_2 = \frac{\ddot{\theta}_0}{2} \tag{3.44}$$

$$a_3 = \frac{20\theta_f - 20\theta_0 - (8\dot{\theta}_f + 12\dot{\theta}_0)t_f - (3\ddot{\theta}_0 - \ddot{\theta}_f)t_f^2}{2t_f^3} \tag{3.45}$$

$$a_4 = \frac{-30\theta_f + 30\theta_0 + (14\dot{\theta}_f + 16\dot{\theta}_0)t_f + (3\ddot{\theta}_0 - 2\ddot{\theta}_f)t_f^2}{2t_f^4} \tag{3.46}$$

$$a_5 = \frac{12\theta_f - 12\theta_0 - (6\dot{\theta}_f + 6\dot{\theta}_0)t_f - (\ddot{\theta}_0 - \ddot{\theta}_f)t_f^2}{2t_f^5} \tag{3.47}$$

The final θ_{ref} curves obtained for each walking speed range are represented in Figure 31.

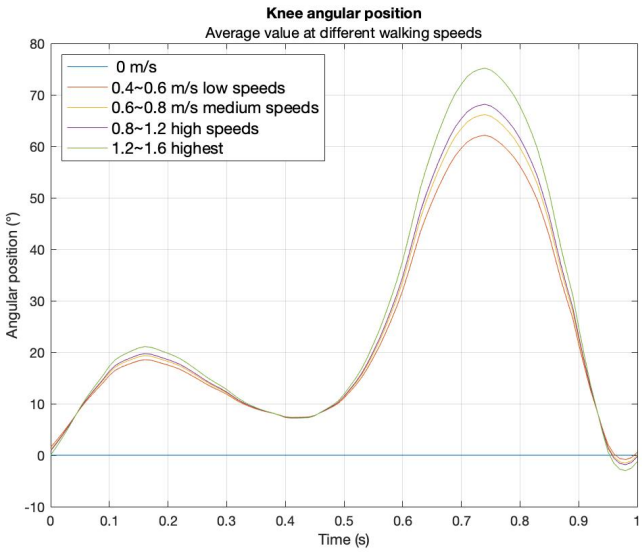

Figure 31: Knee joint angular position θ_{ref} used as reference control signal

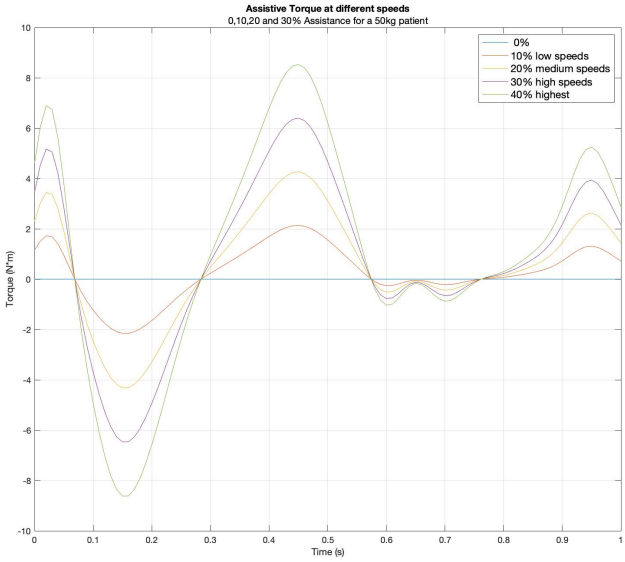

Figure 32: Knee joint torque τ_{ref} in case of a torque control algorithm

3.2.1.1.2 Knee joint Assistive Torque: Cubic Polynomial Trajectory

The torque path has been obtained from an open source dataset[32], whose data is normalized to $\frac{Nm}{kg}$.

The function has been derived in order to obtain the first derivative constraints. Since the second derivative of the function didn't show a suitable outcome, the cubic polynomials have been chosen for the torque trajectory reference.

Datapoints have been sampled at the same significative time instants as in knee position curve case. For each single cubic polynomial $\tau(t) = a_0 + a_1 t + a_2 t^2 + a_3 t^3$ the following constraints are needed:

- initial value $\tau(0) = \tau_0$;
- final value $\tau(t_f) = \tau_f$;
- initial first derivative $\dot{\tau}(0) = \dot{\tau}_0$;
- final first derivative $\dot{\tau}(t_f) = \dot{\tau}_f$.

Applying these four constraints, the following equations arise, allowing the unknown parameters computation:

$$\tau_0 = a_0 \tag{3.48}$$

$$\dot{\tau}_0 = a_1 \tag{3.49}$$

$$\tau_f = a_0 + a_1 t_f + a_2 t_f^2 + a_3 t_f^3 \tag{3.50}$$

$$\dot{\tau}_f = a_1 + 2a_2 t_f + 3a_3 t_f^2 \tag{3.51}$$

Whose solution is:

$$\tau_0 = a_0 \tag{3.52}$$

$$\dot{\tau}_0 = a_1 \tag{3.53}$$

$$a_2 = \frac{3(\tau_f - \tau_0)}{t_f^2} - \frac{2\dot{\tau}_0 + \dot{\tau}_f}{t_f} \tag{3.54}$$

$$a_3 = -\frac{2(\tau_f - \tau_0)}{t_f^3} + \frac{\dot{\tau}_0 + \dot{\tau}_f}{t_f^2} \tag{3.55}$$

These equations allow the computation of each cubic polynomial that connects two consecutive datapoints. The obtained curve magnitude is adjusted according to the subject weight. After the cubic polynomial interpolation, the result is equal to the τ_j function (Figure 33), which is needed in order to be exploited in the Bowden cable friction compensation (Equation 2.4).

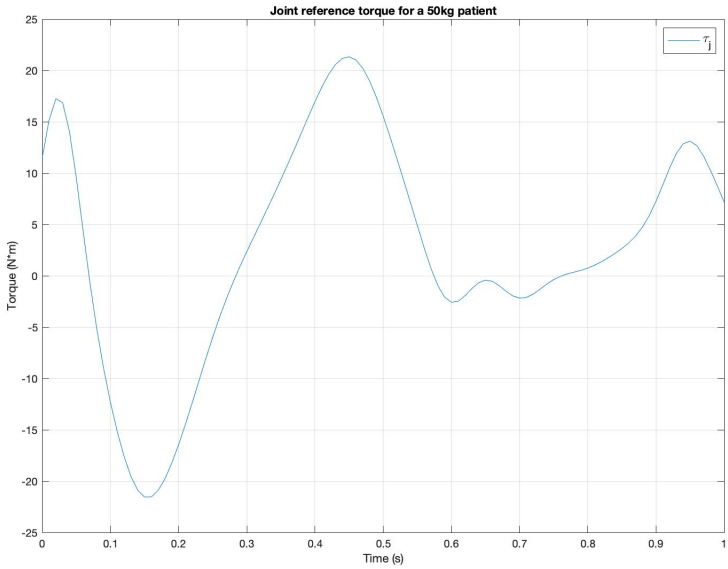

Figure 33: Knee joint reference torque for a 50kg patient. These values are used in the Bowden Cable friction compensation model

The majority of AAN exoskeleton takes advantage of the torque as reference control signal. However, in order to properly apply a torque control strategy, a linear force sensor is needed. One of the limitations regarding the exoskeleton design of this dissertation is the absence of a force cell sensor, which could have been used in order to control the knee joint in terms of torque. The following paragraph shows how the assistance protocol would be if the low level control were to be a closed loop torque control system instead of a closed loop velocity control system.

The torque reference signal magnitude can be regulated accordingly to the walking speed, in terms of percentage of assistance. A higher speed corresponds to a maximum of 40% assistance.

Thus, the torque reference signal is 40% of that physiologically generated by a healthy subject. A lower speed range corresponds to a lower assistance. The choice is related to the therapeutic objective of the device. The patient should not be assisted completely but only partially, during critical gait phases. The τ_{ref} curves that could be used as reference signal in case of closed loop torque control are shown in Figure 32. Their magnitude depends on the estimated walking speed value.

3.2.2 Bowden Cable friction compensation model

This part of the algorithm computes the final motor desired speed $\dot{\theta}_{m,ref}$ that constitutes the reference signal for the low level closed loop speed controller. The $\dot{\theta}_{m,ref}$ is composed of two terms (2.8): the first one depends on the mechanical structure of the exoskeleton and the desired knee trajectory θ_{ref}, while the second one represent the Bowden cable friction compensation. The first term represents the ideal desired motor angular position. It is obtained by multiplying θ_{ref} for the joint to motor pulleys radius ratio. The second term is obtained by computing the inner cable force (2.4) using τ_{ref} as joint torque and then deriving the resulting linear displacement dividing the force (2.4) by the axial stiffness that in this application is equal to:

$$k_{cb} = \frac{E_{steel} \cdot A_{cb}}{L_{cb}} = 367,52\frac{N}{m}. \tag{3.56}$$

Finally, the linear displacement obtained is divided by the motor pulley radius in order to obtain the corresponding angle spaced by the motor. Once $\theta_{m,ref}$ (2.8) has been computed,

the corresponding velocity curve $\dot{\theta}_m$ is obtained through discrete time derivative and converted from $\frac{deg}{s}$ to rpm. This conversion is due to the fact that the servodriver receives and controls the motor with velocity expressed in rpm.

The resulting trajectory is the $\dot{\theta}_{m,ref}$ signal reference used by the low level closed loop velocity controller.

3.3 Low level control: PID and Motor model

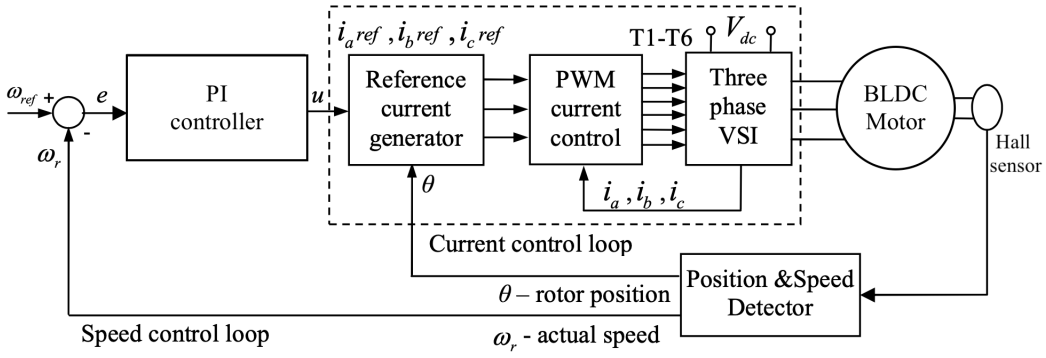

Figure 34: Low level speed closed loop control block scheme

The project involves the implementation of the low-level controller in the MASCON 50/5 servomotor (Appendix A.4). This device is able to compare the actual speed signal monitored through the Encoder in A.3 with the reference value received from Arduino. If a deviation is perceived, the motor speed is dynamically adjusted.

MASCON 50/5 operates as a PI closed loop speed controller. Through his customized software it is possible to firstly complete the device configuration, reporting all the significant known motor datas. The speed constant, number of pole pairs, thermal time constant winding, presence of sensors apart from the Hall integrated sensors, maximum speed, nominal current, maximum output current limit and operation mode are required.

Secondly, the PI controller can be tuned both manually or automatically. If desired, the P value

and integral time constant can be changed inserting their values manually.

Before the entire hardware was assembled, the high and medium control levels have been tested. A motor and PI controller model was built in *Simulink*© and used for MIL and PIL tests, in order to evaluate the upper control layers and motor model performance.

3.3.1 PI controller

The PI controller is widely implemented for BLDC motors control. The requirements that a speed controller has to satisfy are accuracy, responsiveness and limited overshoot. The PI controller has the capability of meeting these objectives when tuned correctly. A significative advantage of PI controller is that it is easily re-tunable on-line [51]. The controller output is represented as follows:

$$u(t) = K_p \cdot e(t) + K_i \int_0^t e_t dt \tag{3.57}$$

As shown in Figure 34, $e(t)$ represents the error between the motor velocity reference signal and the actual motor speed, while $u(t)$ represents the controller output signal. K_p and K_i are the proportional and integral gain respectively. Adjusting these two parameters it is possible to minimize rise time and steady-state error. The effects that the parameters tuning has on output are summarized in Table VIII.

Looking at it, it can be seen that increasing K_i and K_p in order to reduce the rise time and steady state error, overshoot will consequentially increase. An additional parameter that would compensate this effect is the derivative gain K_d.

TABLE VIII: Effects of Control Parameter on Output

Control parameter	K_p	K_i
Rise time	Decrease	Decrease
Overshoot	Increase	Increase
Settling time	Small change	Increase
Steady state error	Decrease	Eliminate

This component cannot be implemented with MASCON 50/5 servodriver, however his contribution would reduce the oscillation, increase stability and eliminate overshoot.

3.3.2 BLDC model

In order to build a BLDC motor schematic in *Simulink*©, it is fundamental to understand its functioning. Brushless DC motors have two critical parts: the stator and the rotor. The phase windings are wrapped around the stator, while the rotor is constructed with permanent magnets composed of a certain number of poles[53]. The mechanical commutator is replaced with an electronic switching converter [52]. In fact, the BLDC motor is a permanent magnet synchronous motor (PMSM) with trapezoidal back electromagnetic force (EMF). The stator generates the magnetic field in order to induce the rotor motion, while the Hall Effect sensors detect the rotor position as the commutating signals.

BLDC motor analysis is based on certain assumptions for model simplification[53];

- the motor is not saturated;
- self inductance is constant, as mutual inductance;
- stator impedances are equal;

- inverter semiconductors are ideal;
- iron loss is neglected;
- EMF waveforms are equal for all phases.

Normally, to a 3-phase brushless DC motor corresponds six electronic switches that generates 3-phase voltage. The rotor position is translated into a switching sequence [54][55].

The dynamic equations of a BLDC motor are derived using the assumption listed above and are present in Appendix D. Figure 35 shows the Simulink model of the BLDC motor speed control

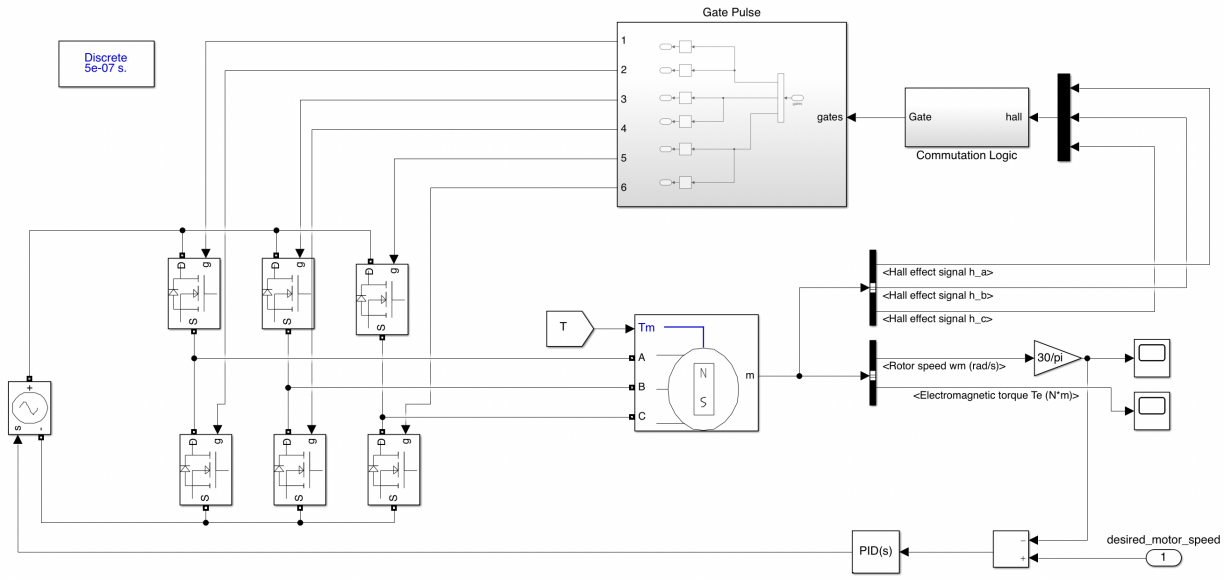

Figure 35: BLDC motor closed loop speed control model implemented in *Simulink*©

loop. The commutation logic block decodes the Hall sensor signal sequence and generates the back EMF. The gate pulse block follows, which is responsible of the six step inverter switching with the proper sequence according to the back EMF.

3.3.3 MIL simulation

In order to evaluate the low level controller and motor performance in presence of a reference signal generated from the higher control levels, some Model in-the-Loop (MIL) tests have been performed, using the signal obtained from the quintic polynomial interpolation.

MIL testing is referred to as the control logic verification process that occurs as first stage. Both the plant and controller are modeled and simulated offline in the same modeling target, which in this case is Simulink.

Two tests have been performed: considering a walking speed of $1,2\frac{m}{s}$, the corresponding knee joint angle trajectory was generated and then the corresponding desired motor speed curve was computed and fed into the closed loop system in rpm. During the first test, no disturbance was applied, while during the second one a constant unitary step disturbance was added between the controller and the motor model.

Firstly, the PID controller has been tuned by exploiting the Ziegler-Nichols method [56].

The open loop system was fed with a constant unitary step signal and the response was observed.

Following the Ziegler-Nichols method, the parameters shown in Figure 36 have been derived by drawing a tangent line to the steepest point of the output curve (Figure 37).

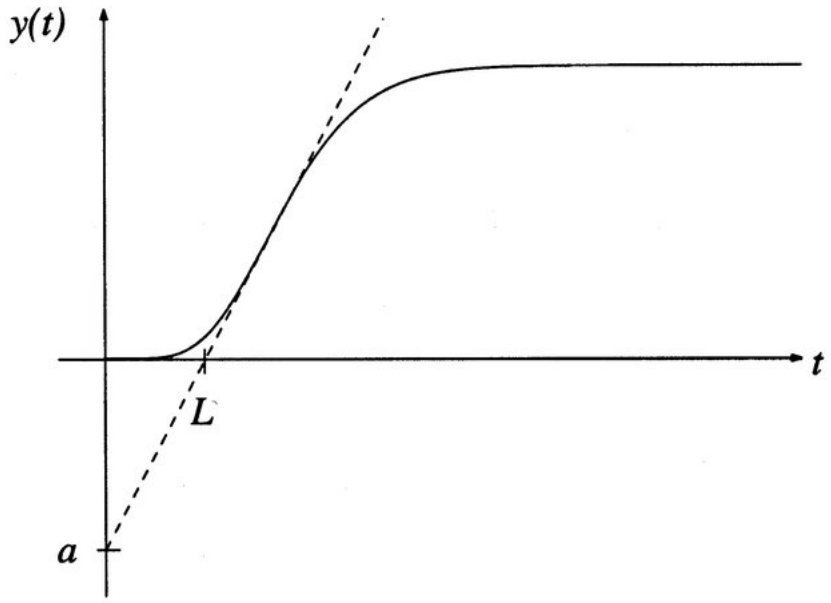

Figure 36: Ziegler-Nichols tuning method - how to measure a and L from output

Then, after obtaining a and L, the corresponding integral and proportional gains are computed. Their values are listed in Table IX.

TABLE IX: Ziegler-Nichols Tuning Parameter Obtained from Open Loop System

a	-0,19
L	$1,2 \cdot 10^{-5}$
Kp	$\frac{0.9}{a} = 4,74$
Ki	$\frac{1}{3L} = 27,7 \cdot 10^{3}$

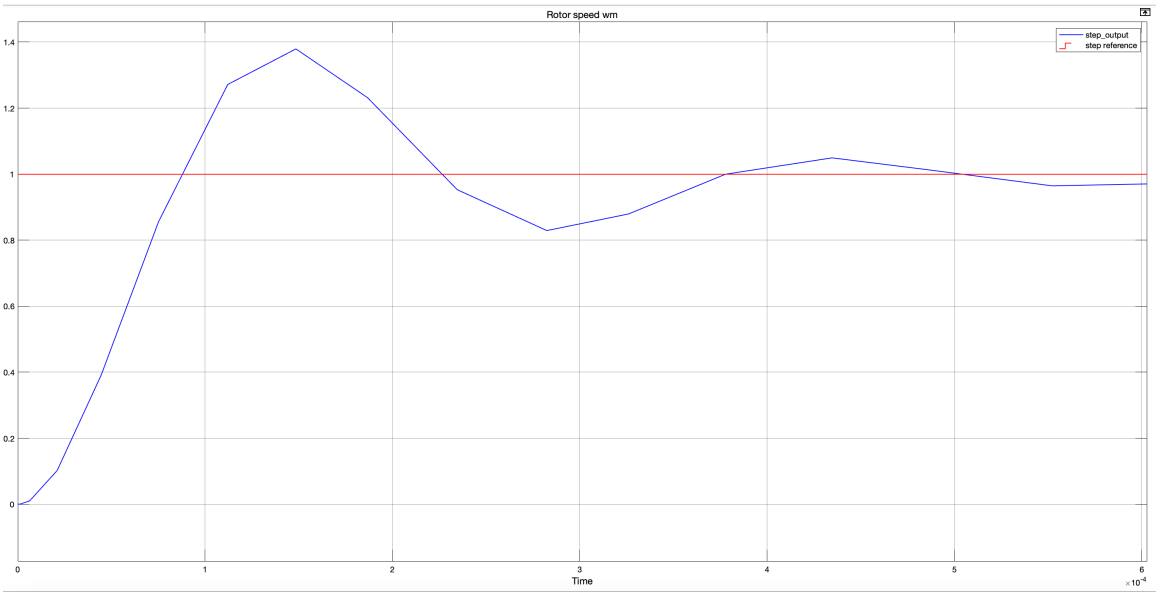

Figure 37: Open loop step response of the system

The obtained gains have then been used as PI controller gains during the simulations with motor speed reference signal $\omega_{m,ref}$. The overall response improved in terms of steady state error that appeared cancelled (Figure 38), while the oscillations increased (Figure 39).

Since the MASCON 50/5 servocontroller is not able to implement a derivative component, the controller used in this simulation is a PI and it is not possible to reduce the overshoot significantly using an integrative and a proportional parameter only. The presence of an element that is able to anticipate the future output changes improves the performance in terms of overshoot and oscillations.

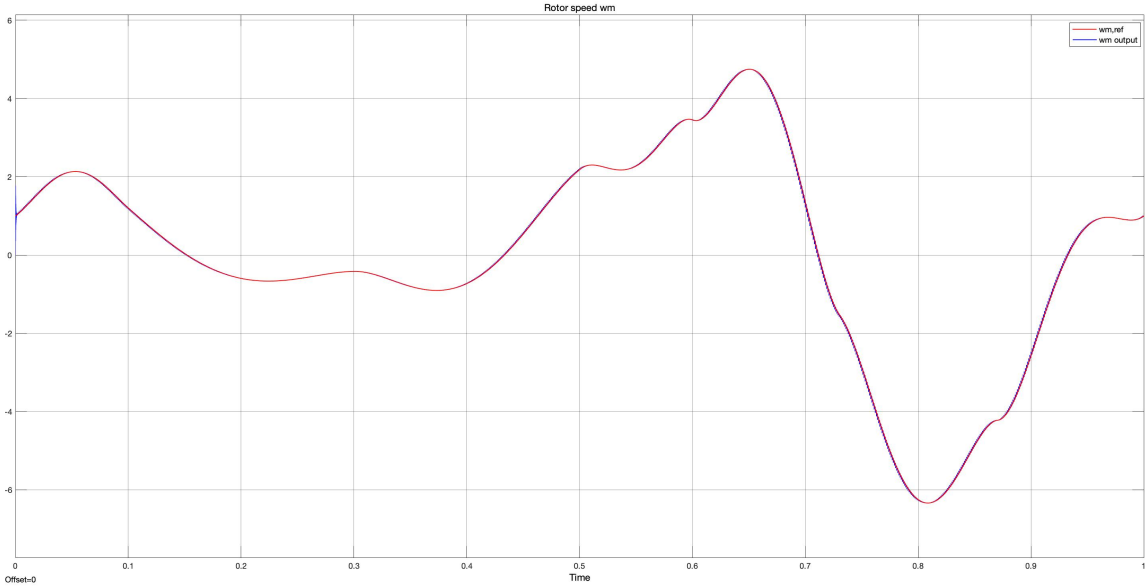

Figure 38: System response to the desired motor speed

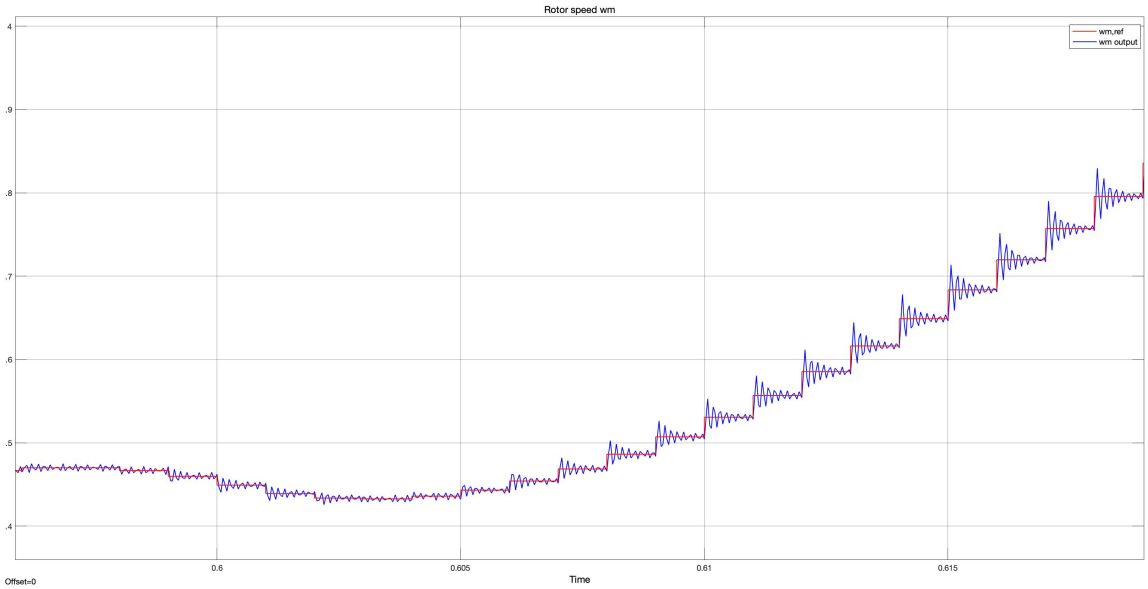

Figure 39: Output motor speed signal oscillations with respect to the desired curve

In Figure 40 the output signal $w_{m,out}$ response during the first milliseconds is shown. It is evident that a significant overshoot has been measured. Its maximum peak is equal to: $P.O. = 75\%$.

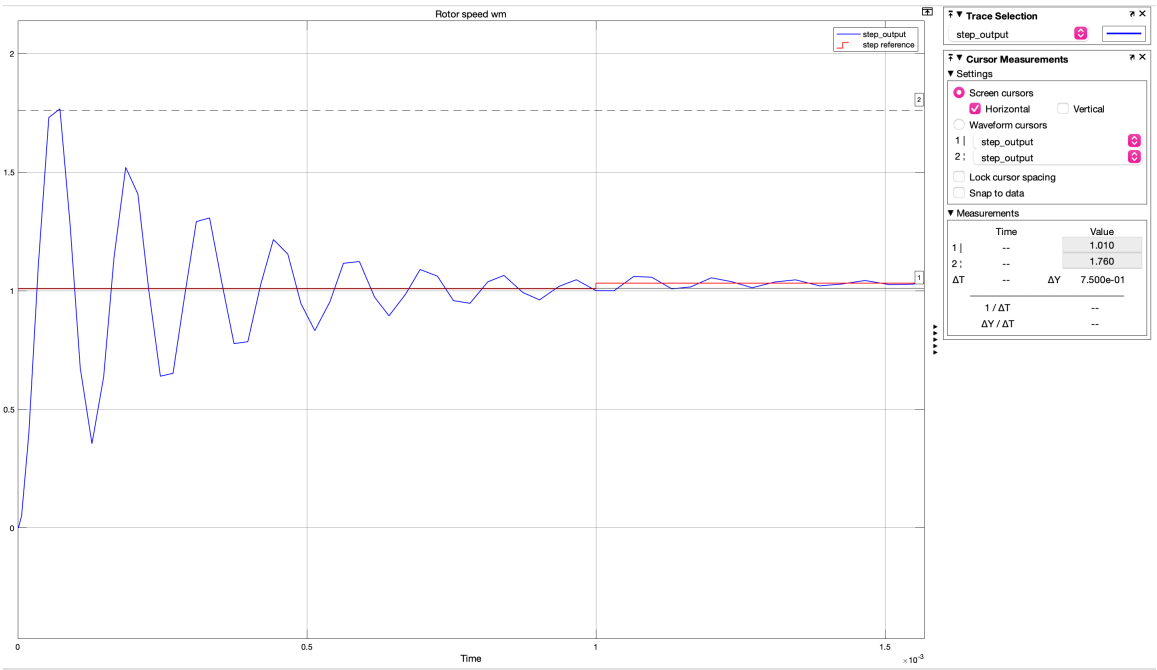

Figure 40: System overshoot

On the contrary, it is notable that the performance is notable in terms of settling time, (Figure 41) which has been measured and is equal to: $t_{s,2\%} = 1,04ms$. Furthermore, the rise time appeared to be low; it has been measured as equal to: $t_r = 30,45\mu s$.

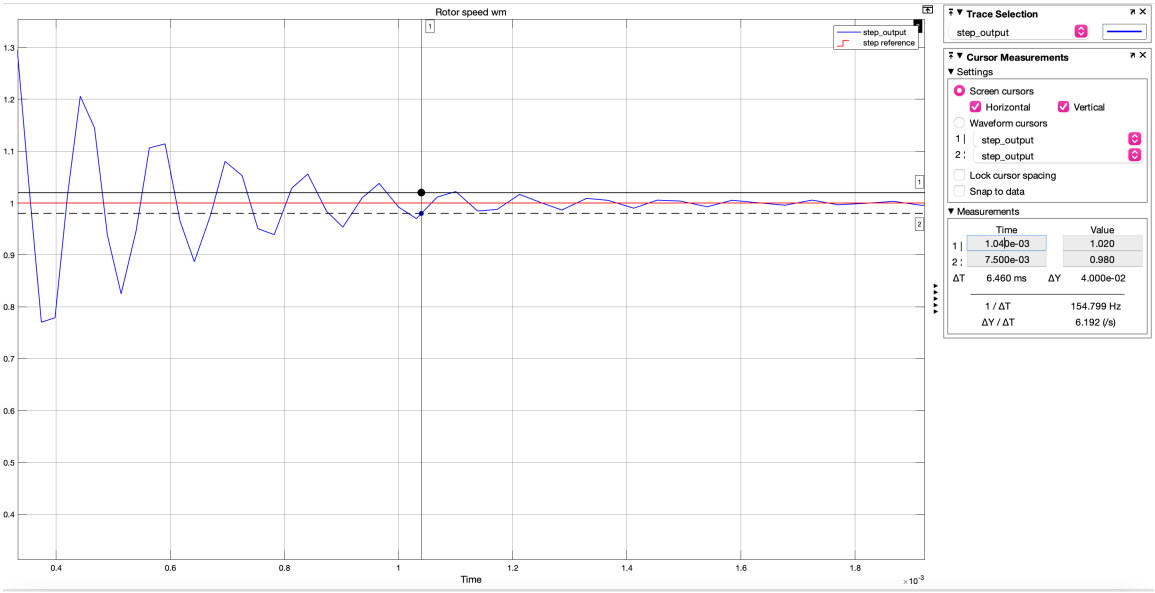

Figure 41: System settling time

The overall performance has been considered valuable, since the steady state error has been deleted and, considering the several changes in the speed trend, the oscillations and the settling time are relatively limited.

The presence of a derivative component would have improved the system response in terms of oscillation, but it would not be consistent with the servocontroller designed for the exoskeleton hardware.

CHAPTER 4

TESTING, MEASUREMENTS AND RESULTS

The PIL (Processor-in-The Loop) test is a real-time procedure in which the C-code generated from the built Simulink model is deployed in the target hardware and run while data is transferred to another Simulink model used for verification purposes.

The first version of the device presented has been tested, entirely deploying the control algorithm in Arduino Mega 2560 and then connecting the microcontroller to the main PC, in which a Simulink model for PIL simulation was run in real-time.

The pilot study consisted in a healthy subject wearing the unactivated device performing simple walking tasks on a treadmill. Specifically, the subject has been asked to walk at 0.5,0.9 and 1.2 $\frac{m}{s}$. The tests have been performed at *Shirley Ryan AbilityLab.*

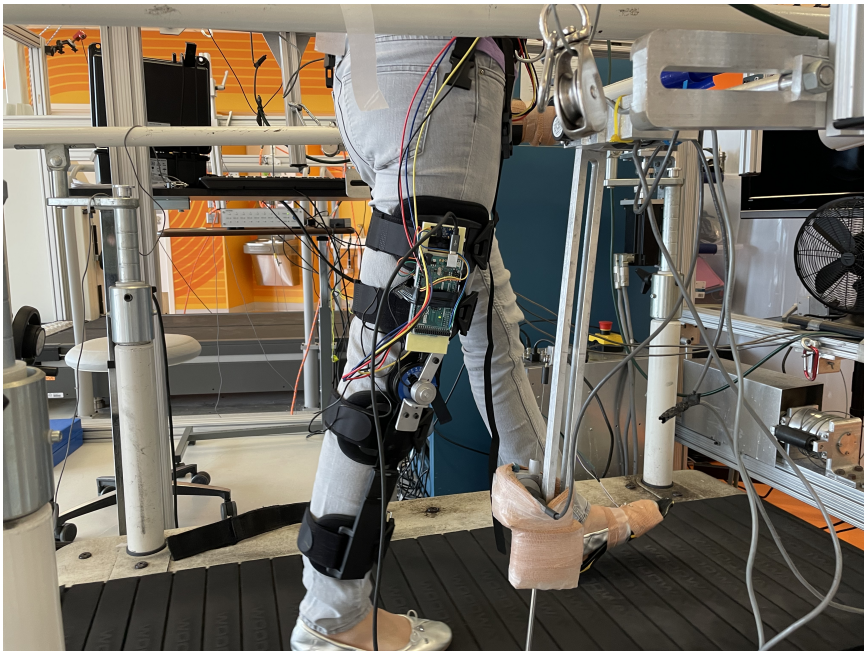

Figure 42: PIL pilot test

First of all, the algorithm has been updated with the weight of the subject. The FSR resulting thresholds result equal to:

$HeelThresholdIn = 1,098V, ToeThreshold = 0,825V, HeelThreshold = 0,660V$.

Then, the exoskeleton has been worn . As shown in Figure 43, the potentiometer is mounted in correspondence of the joint, while the microcontroller is attached to the upper part of the orthosis. The IMU sensor is properly attached to the back of the board on which the electrical circuits have been mounted. The foot sensor is worn on the opposite foot, the FSR sensors are connected to the board through long electrical wires that are supported by a belt.

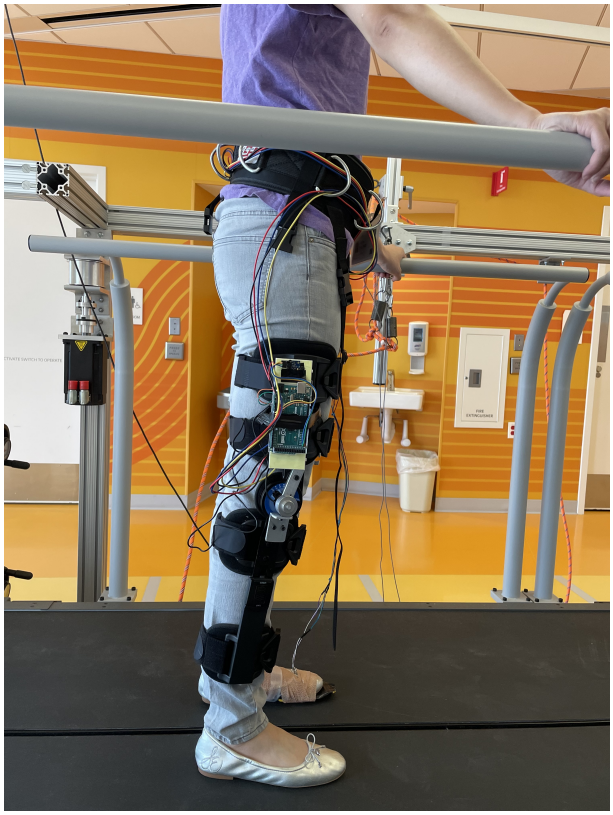

(a) Sagittal plane

(b) Coronal plane

Figure 43: Overall exoskeleton structure worn by an healthy subject

After verifying that the FSR thresholds of the FSM algorithm have been updated, the subject has been asked to walk for 60 seconds. The speed has been maintained constant for the whole time during each test, in order to evaluate the changes in speed evaluation.
The acceleration signals collected from the IMU have been measured (Figure 44), as well as the Y-axis orientation estimated by the Kalman filter algorithm (Figure 45).

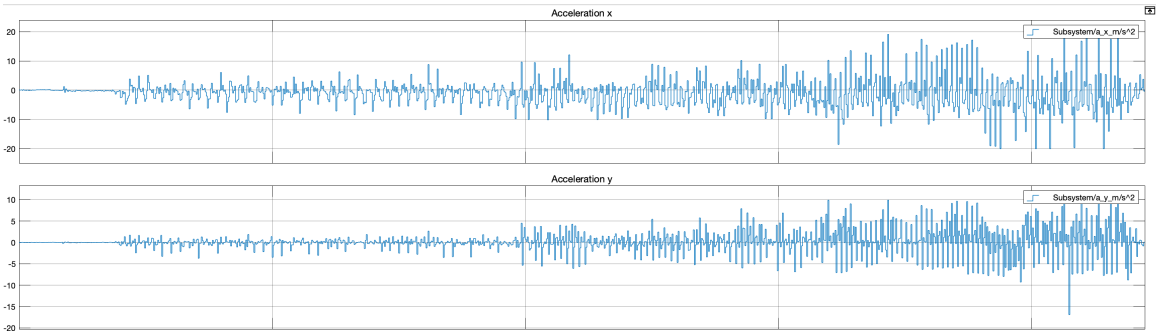

Figure 44: Accelerometer along x and y signals in time

What arises from the tests at different treadmill speeds was a visible variation in the speed estimation value during each test. This allows the computation of the maximum error of the speed estimation algorithm.

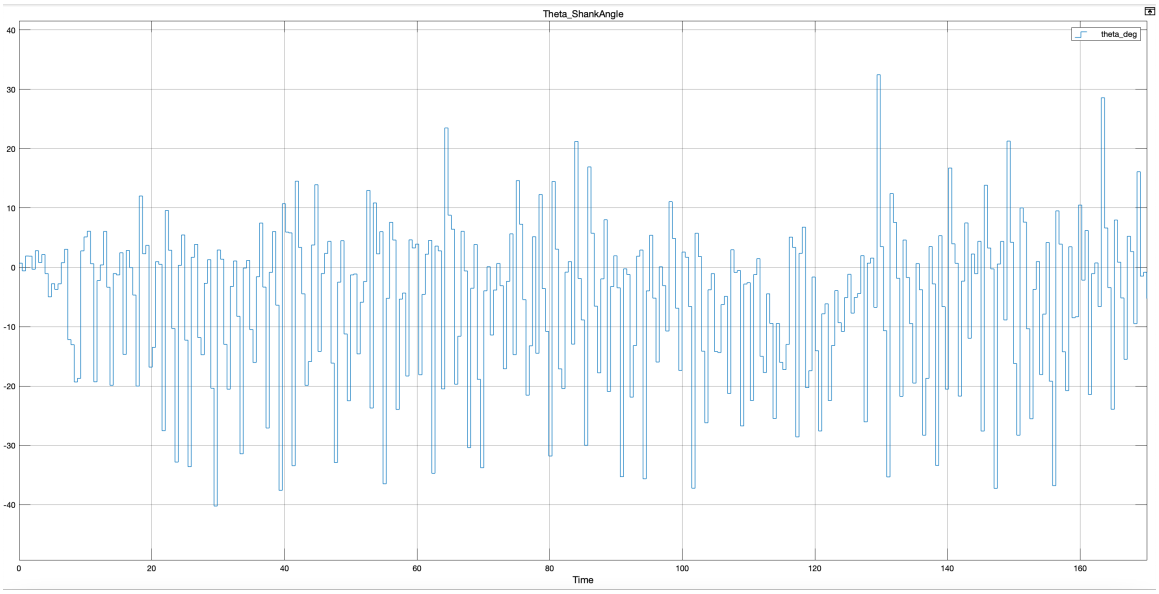

Figure 45: Y-axis orientation obtained through Kalman filter

In the following Table X the speed estimated values obtained during the three run tests are presented.

As can be noticed, to lower speeds corresponds an higher error. This particular measure is strongly related to disturbances, human errors and vibration disturbs. This error could vary in a significant way running other tests under different environment and subject conditions.

The potentiometer signal has been measured while the walking task was performed. The peak values and shape result adequate. Furthermore, the knee angular speed , which is obtained by the discrete-time derivation of the potentiometer signal, has been compared in time to the knee position detected (Figure 46).

TABLE X: Estimated Speed Errors Obtained

Treadmill speed	Maximum error Speed Estimated value
0.5	38%
0.9	17,7%
1.2	15%

The overall high control level performance has been evaluated in terms of Assistance period length. Considering the gait cycle division and the considerations about its phases, the assistance should be present during approximately 73% of the time.

The longest assistance period detected lasted 75% of the gait cycle, while the shortest one lasted 66.55% of the gait cycle (Figure 47).

The joint position output has been evaluated (Figura 48).

It is interesting to notice two aspects related to this curve.

Firstly, it can be noticed that for a certain period of time the joint position is equal to zero. This is due to the fact that during the *"no assistance"* period the middle level controller has to erogate a null signal, since the motor velocity has to be zero.

Furthermore, looking at the curve maximum points, it is possible to see that two different joint position magnitudes are present, even though the test is run at constant speed. This event occured because of the error in the walking speed estimation.

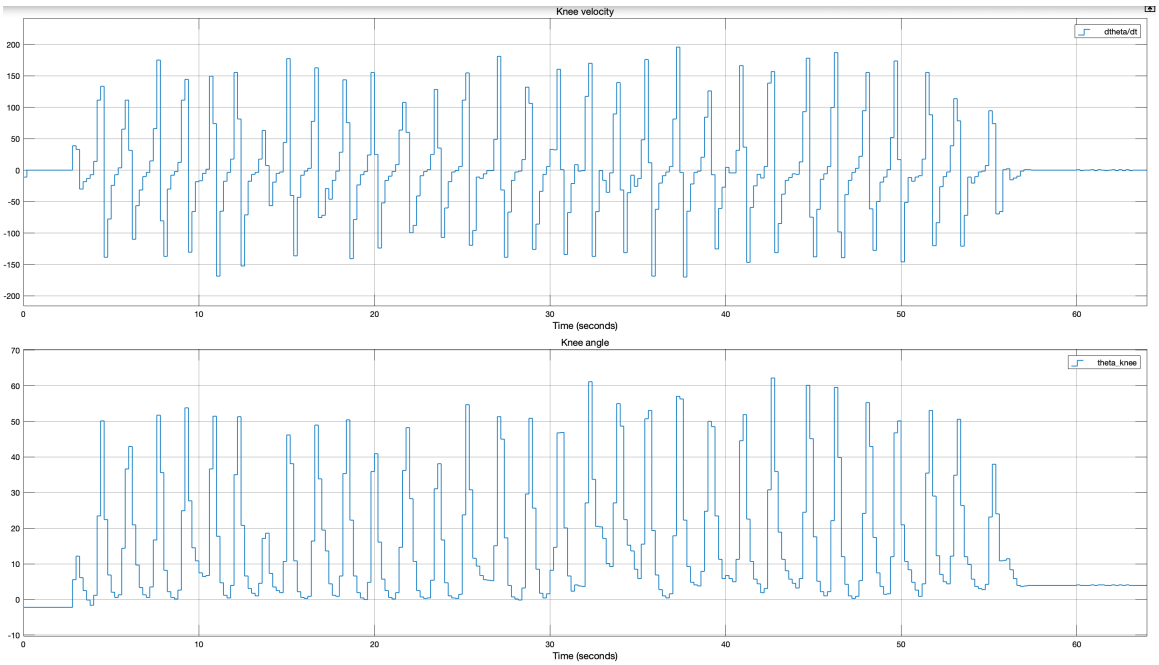

Figure 46: Knee angle measured by the potentiometer and its time-discrete first derivative

During a certain time interval the estimated velocity was lower than the effective one.

This resulted in an error in trajectory reference computation.

Finally, the motor speed reference signal $\omega_{m,ref}$ has been registered. This signal is the result of the high and middle level control algorithm deployed in Arduino. The speed value shown in Figure 49 is measured in rpm.

This signal has to be fed into the servodriver, in order to be able to control the actuator.

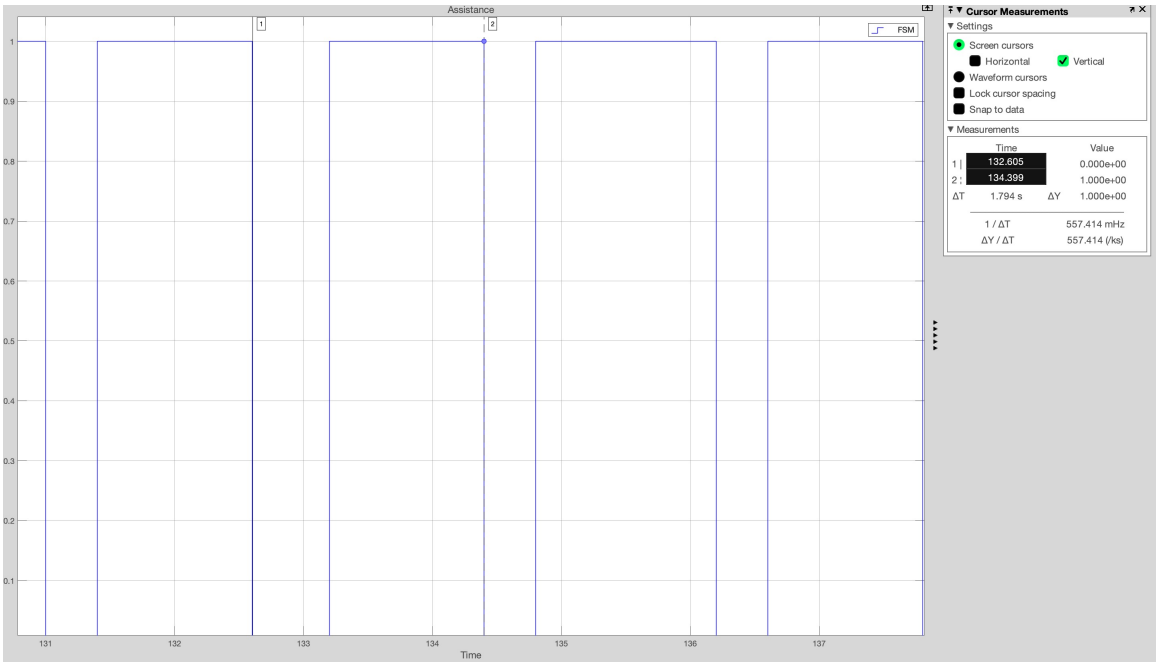

Figure 47: Assistance switching

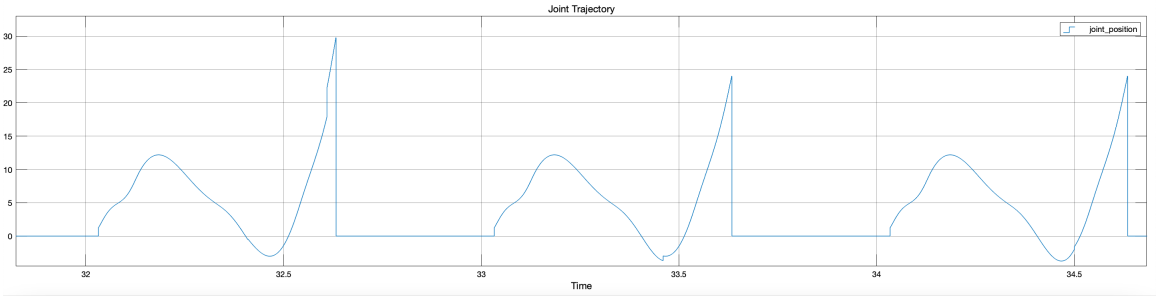

Figure 48: Joint position reference signal computed based on estimated walking speed

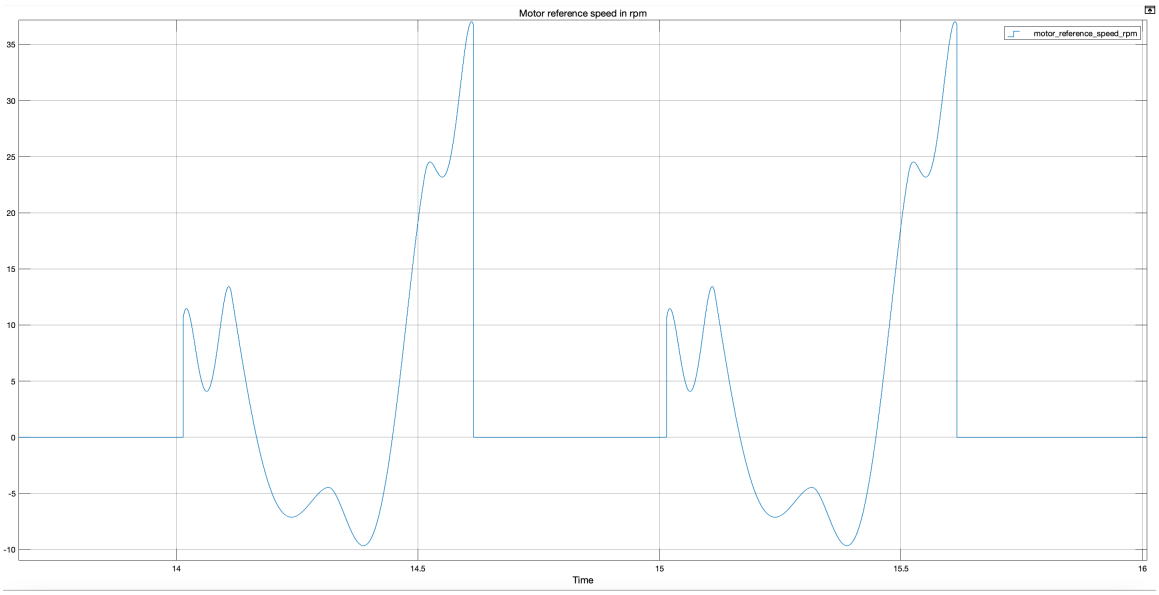

Figure 49: Motor speed reference signal $\omega_{m,ref}$

CHAPTER 5

CONCLUSIONS

AAN exoskeletons are an important resource for the rehabilitation of patients with cerebral palsy. The positive responses obtained from therapies assisted by robotic orthoses demonstrate how crucial these devices can be for motor recovery and the acquisition of greater mobility and independence for patients.

Pediatric devices should be of primary interest, as initiating physical therapies from an early age provides a greater possibility of success.

The device designed in this dissertation constitutes a cost-effective prototype that may be open to improvement and further tests.

Given the results obtained from the pilot test, the FSM assistance performance resulted to be satisfactory, considering the assistance periods with respect to the entire gait cycle. The FSR and potentiometer sensors have demonstrated positive reactivity and good signal quality resulting in accurate gait phase detection.

The following step to be accomplished is mounting the overall structure and completing the assembly, including the servodriver, motor and security system.

Moving forward, the device should be further tested in order to verify the effective therapeutic outcome. If possible, a long term trial involving different subjects affected by hemiplegia would demonstrate the evidence of significant improvement.

The actual device could be adjusted under different aspects.

A lighter mechanical structure could be designed, drawing with a CAD software and then printing it in 3D, in order to further lighten the structure and substitute the orthopedic brace that could be too bulky for really young patients.

The microcontroller should be improved in terms of memory availability and processing speed. In order to enhance the control algorithm, a more powerful device is needed, since Arduino could result limited. The substitution with a microprocessor with an integrated operational system could be adequate.

The control algorithm could be optimized under different levels.

The high level controller could exploit the EMG signals, in case of patients with a low level CP that have a EMG signal that is not significantly altered with respect to the one of a healthy subject. Furthermore, the speed estimation algorithm could be improved or the speed ranges of the medium control level could be adjusted. As the measurements performed in the pilot test have shown, the error in estimating the walking speed could lead the computation of the wrong reference curve if the speed is excessively over- or underestimated.

Finally, if there were the possibility to add a load cell linear force sensor, the torque control strategy could be tested, in order to compare its performance with respect to the closed loop speed controller currently implemented.

APPENDICES

Appendix A

MOTOR AND GEARHEAD DATASHEETS

Appendix A (continued)

A.1

EC-4pole 30 ∅30 mm, brushless, 200 Watt

High Power

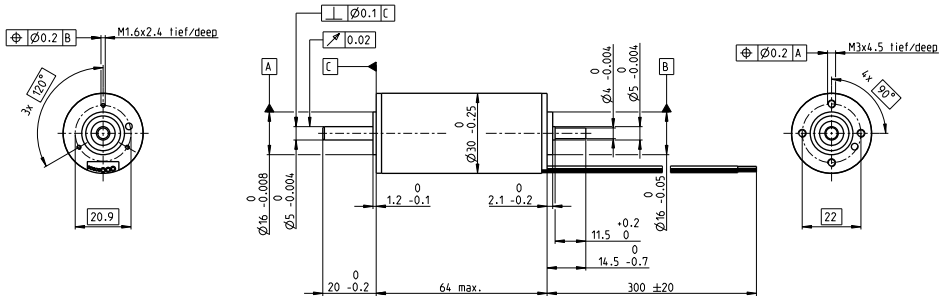

M 1:2

Stock program
Standard program
Special program (on request)

Motor Data		Part Numbers 305013	305014	305015
Values at nominal voltage				
1 Nominal voltage	V	24	36	48
2 No load speed	rpm	16700	16700	16500
3 No load current	mA	723	482	356
4 Nominal speed	rpm	16100	16100	16000
5 Nominal torque (max. continuous torque)	mNm	95.6	95.2	92.9
6 Nominal current (max. continuous current)	A	7.61	5.06	3.68
7 Stall torque	mNm	3240	3520	3430
8 Stall current	A	236	171	124
9 Max. efficiency	%	90	90	90
Characteristics				
10 Terminal resistance phase to phase	Ω	0.102	0.21	0.386
11 Terminal inductance phase to phase	mH	0.016	0.037	0.065
12 Torque constant	mNm/A	13.7	20.6	27.6
13 Speed constant	rpm/V	697	465	346
14 Speed/torque gradient	rpm/mNm	5.17	4.75	4.83
15 Mechanical time constant	ms	1.80	1.66	1.69
16 Rotor inertia	gcm²	33.3	33.3	33.3

Specifications

Thermal data

17	Thermal resistance housing-ambient	7.4 K/W
18	Thermal resistance winding-housing	0.21 K/W
19	Thermal time constant winding	2.11 s
20	Thermal time constant motor	1180 s
21	Ambient temperature	-20...+100°C
22	Max. winding temperature	+155°C

Mechanical data (preloaded ball bearings)

23	Max. speed		25 000 rpm
24	Axial play at axial load	< 4.0 N	0 mm
		> 4.0 N	0.14 mm
25	Radial play		preloaded
26	Max. axial load (dynamic)		5.5 N
27	Max. force for press fits (static)		73 N
	(static, shaft supported)		1300 N
28	Max. radial load, 5 mm from flange		25 N

Other specifications

29	Number of pole pairs	2
30	Number of phases	3
31	Weight of motor	300 g

Values listed in the table are nominal.

Connection motor (Cable AWG 18)

black	Motor winding 2
white	Motor winding 3
red	Motor winding 1

Connection sensors (Cable AWG 26)

black/grey	Hall sensor 2
blue	GND
green	V_{Hall} 3...24 VDC
red/grey	Hall sensor 1
white/grey	Hall sensor 3

Wiring diagram for Hall sensors see p. 47

Operating Range Comments

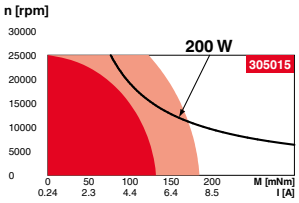

Continuous operation
Continuous operation with reduced thermal resistance R_{th2} 50%
Intermittent operation

Assigned power rating

maxon Modular System Details on catalog page 36

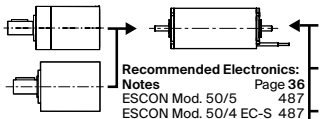

Planetary Gearhead
∅32 mm
4 - 8 Nm
Page 392

Planetary Gearhead
∅42 mm
3 - 15 Nm
Page 397-398

Recommended Electronics:

Notes	Page 36
ESCON Mod. 50/5	487
ESCON Mod. 50/4 EC-S	487
ESCON Mod. 50/8 (HE)	488
ESCON 50/5	489
ESCON 70/10	489
DEC Module 50/5	491
EPOS4 Mod./Comp. 50/5	496
EPOS4 Module 50/8	497
EPOS4 Comp. 50/8 CAN	499
EPOS4 50/5	501
EPOS4 70/15	501

Encoder 16 EASY/XT
128 - 1024 CPT, 3 channels
Page 449/451
Encoder 16 EASY Absolute/XT
4096 steps, Single Turn
Page 453/455
Encoder 16 RIO
1024 - 32768 CPT, 3 channels
Page 466
Encoder AEDL 5810
1024 - 5000 CPT, 3 channels
Page 469
Encoder HEDL 5540
500 CPT, 3 channels
Page 476
Brake AB 20
24 VDC, 0.1 Nm
Page 517

Appendix A (continued)

A.2
Planetary Gearhead GP 32 HP ∅32 mm, 4.0–8.0 Nm

High Power

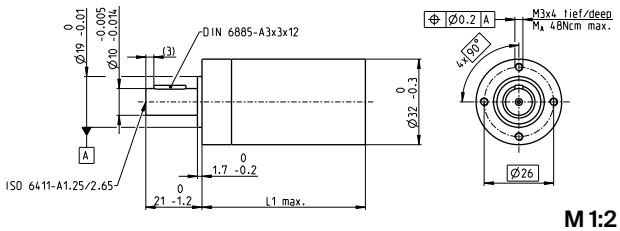

M 1:2

Technical Data

Planetary Gearhead			straight teeth
Output shaft			stainless steel
Bearing at output			ball bearing
Radial play, 10 mm from flange			max. 0.14 mm
Axial play			max. 0.4 mm
Max. axial load (dynamic)			120 N
Max. force for press fits			120 N
Direction of rotation, drive to output			=
Max. continuous input speed			8000 rpm
Recommended temperature range			-40...+100°C
Number of stages	2	3	4
Max. radial load, 10 mm from flange	200 N	250 N	300 N

gear

Stock program
Standard program
Special program (on request)

		Part Numbers						
		320247	326663	326664	326668	326672	324947	324952
Gearhead Data								
1 Reduction		14:1	33:1	51:1	111:1	190:1	456:1	706:1
2 Absolute reduction		676/49	529/16	17576/343	13824/125	456976/2401	89401/196	158171/224
3 Max. motor shaft diameter	mm	6	3	6	4	6	3	3
Part Numbers		326659		326665	326669	324942	324948	324953
1 Reduction		18:1		66:1	123:1	246:1	492:1	762:1
2 Absolute reduction		624/35		16224/245	6877/56	421824/1715	86112/175	19044/25
3 Max. motor shaft diameter	mm	6		6	3	6	6	4
Part Numbers		326660		326666	326670	324944	324949	324954
1 Reduction		21:1		79:1	132:1	295:1	531:1	913:1
2 Absolute reduction		299/14		3887/49	3312/25	101062/343	331776/625	36501/40
3 Max. motor shaft diameter	mm	6		6	4	6	4	3
Part Numbers		326661		326667	326671	324945	324950	
1 Reduction		23:1		86:1	159:1	318:1	589:1	
2 Absolute reduction		576/25		14976/175	1587/10	389376/1225	20631/35	
3 Max. motor shaft diameter	mm	4		6	3	6	6	
Part Numbers		326662		320297		324946	324951	
1 Reduction		28:1		103:1		411:1	636:1	
2 Absolute reduction		139/5		3588/35		359424/875	79488/125	
3 Max. motor shaft diameter	mm	4		6		6	4	
4 Number of stages		2	2	3	3	4	4	4
5 Max. continuous torque	Nm	4	4	8	8	8	8	8
6 Max. intermittent torque at gear output	Nm	6	6	12	12	12	12	12
7 Max. efficiency	%	75	75	70	70	60	60	60
8 Weight	g	178	178	213	213	249	249	249
9 Average backlash no load	°	0.8	0.8	1.0	1.0	1.0	1.0	1.0
10 Mass inertia	gcm²	1.6	0.5	1.5	0.7	1.5	1.5	0.7
11 Gearhead length L1	mm	48.3	48.3	55.0	55.0	61.7	61.7	61.7

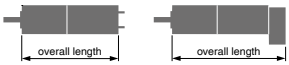

maxon Modular System

+ Motor	Page	+ Sensor/Brake	Page	Overall length [mm] = Motor length + gearhead length + (sensor/brake) + assembly parts						
EC-4pole 30, 200 W	261			112.4	112.4	119.1	119.1	125.8	125.8	125.8
EC-4pole 30, 200 W	261	22 EMT	457	140.3	140.3	147.0	147.0	153.7	153.7	153.7
EC-4pole 30, 200 W	261	16 EASY/XT/Abs.	464-468	126.3	126.3	133.0	133.0	139.7	139.7	139.7
EC-4pole 30, 200 W	261	16 EASY Abs. XT	470	126.8	126.8	133.5	133.5	140.2	140.2	140.2
EC-4pole 30, 200 W	261	16 RIO	481	124.8	124.8	131.5	131.5	138.2	138.2	138.2
EC-4pole 30, 200 W	261	AEDL/HEDL	484/490	133.0	133.0	139.7	139.7	146.4	146.4	146.4
EC-4pole 30, 200 W	261	AB 20	532	148.6	148.6	155.3	155.3	162.0	162.0	162.0
EC-4pole 30, 200 W	261	22EMT/AB 20	457/532	179.8	179.8	186.5	186.5	193.2	193.2	193.2
EC-4pole 30, 200 W	261	16 EASY/XT/Abs./AB 20	464/532	162.7	162.7	169.4	169.4	176.1	176.1	176.1
EC-4pole 30, 200 W	261	16 EASY Abs. XT/AB 20	470/532	163.2	163.2	169.9	169.9	176.6	176.6	176.6
EC-4pole 30, 200 W	261	16 RIO/AB 20	481/532	161.2	161.2	167.9	167.9	174.6	174.6	174.6
EC-4pole 30, 200 W	261	AEDL/HEDL/AB 20	490/532	169.2	169.2	175.9	175.9	182.6	182.6	182.6

Appendix A (continued)

A.3 Encoder ENC 16 EASY, 1000 pulses

Part number 499360

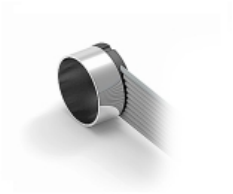

General information	
Counts per turn	1000
Number of channels	3
Line Driver	RS422
Max. length of encoder housing	8.5 mm
Max. electrical speed	90000 rpm
Max. mechanical speed	30000 rpm

Technical Data	
Supply voltage Vcc	5.0V ± 10.0%
Output signal	Incremental
Driver used logic	Differential, EIA RS 422
Output current per channel	-20...20 mA
Signal rise time	20 ns
Measurement condition for signal rise time	CL=25pF, RL=1kOhm
Signal fall time	20 ns
Measurement condition for signal fall time	CL=25pF, RL=1kOhm
Min. state duration	125 ns
Direction of rotation	A before B CW
Index position	A low & B low
Index synchronized to AB	Yes
Typical current draw at standstill	22 mA
Max. moment of inertia of code wheel	0.1 gcm²
Operating temperature	-40...+100 °C
Orientation of encoder output to motor flange	0 °

Product	
Weight	9 g

Appendix A (continued)

A.4 ESCON 50/5, 4-Q Servocontroller for DC/EC motors, 5/15 A, 10 - 50 VDC

Part number 409510

Product		
	Weight	204 g
Motor		
	DC motors up to	250 W
	EC motors up to	250 W
Sensor		
	Without sensor (DC motors)	Yes
	DC tacho	Yes
	Digital incremental encoder (2-channel, single-ended)	Yes
	Digital incremental encoder (2-channel, differential)	Yes
	Digital incremental encoder (3-channel, differential)	Yes
	Digital Hall sensors (EC Motors)	Yes
Operating modes		
	Current controller	Yes
	Speed controller (open loop)	Yes
	Speed controller (closed loop)	Yes
Electrical data		
	Operating voltage Vcc (min.)	10 V
	Operating voltage Vcc (max.)	50 V
	Max. output voltage (factor * Vcc)	0.98
	Max. output current Imax	15 A
	Max. time of peak output current Imax	20 s
	Continuous output current Icont	5 A
	PWM clock frequency of power stage	53.6 kHz
	Sampling rate PI current controller	53.6 kHz
	Sampling rate PI speed controller	5.36 kHz
	Max. efficiency	95 %
	Max. speed (DC)	150000 rpm
	Max. speed (EC; 1 pole pair) block commutation	150000 rpm
	Built-in motor choke per phase	30 μH
Inputs		
	Hall sensor signals	H1, H2, H3
	Encoder signals	A, A, B, B\
	Max. encoder input frequency	1 MHz
	Digital inputs	2
	Functionality of digital inputs	Enable, enable CW, enable CCW, enable CW+CCW, enable + direction of rotation, stop, PWM set value, RC Servo set value, fixed set value
	Analog inputs	2
	Resolution, range, circuit	12-bit, -10…+10V, differential
	Functionality of analog inputs	Set value, current limit, offset, speed ramp
	Potentiometers	2
	Functionality of the potentiometers	set value, current limit, offset, speed ramp, gain, IxR factor
Outputs		

Appendix B

SENSORS DATASHEETS

Appendix B (continued)

B.1

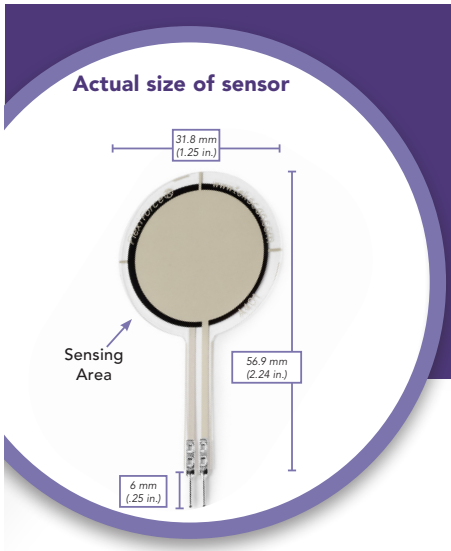

FlexiForce™
Standard Model A401

The FlexiForce A401 is our standard piezoresistive force sensor with the largest sensing area. It is available off-the-shelf for easy proof of concept and is also available in large volumes for design-in applications. The A401 can be used with our test & measurement, prototyping, and embedding electronics, including the FlexiForce Sensor Characterization Kit, FlexiForce Prototyping Kit, FlexiForce Quickstart Board, and the ELF™ System*. You can also use your own electronics, or multimeter.

Benefits

- Thin and flexible
- Easy to use
- Convenient and affordable

Physical Properties

Thickness	0.203 mm (0.008 in.)
Length	56.9 mm (2.24 in.)**
Width	31.8 mm (1.25 in.)
Sensing Area	25.4 mm (1 in.) diameter
Connector	2-pin Male Square Pin
Substrate	Polyester
Pin Spacing	2.54 mm (0.1 in.)

✓ROHS COMPLIANT

** Sensor will require an adapter/extender to connect to the ELF System. Contact your Tekscan representative for assistance.*

***Length does not include pins. Please add approximately 6 mm (0.25 in.) for pin length for a total length of approximately 32 mm (1.25 in).*

	Typical Performance***	Evaluation Conditions
Linearity (Error)	< ±3% of full scale	Line drawn from 0 to 50% load
Repeatability	< ±2.5%	Conditioned sensor, 80% of full force applied
Hysteresis	< 4.5% of full scale	Conditioned sensor, 80% of full force applied
Drift	< 5% per logarithmic time scale	Constant load of 111 N (25 lb)
Response Time	< 5µsec	Impact load, output recorded on oscilloscope
Operating Temperature	-40°C - 60°C (-40°F - 140°F)	Convection and conduction heat sources
Acceptance Criteria	±40% sensor-to-sensor variation	Output considered at test pressure
Durability	≥ 3 million actuations	Perpendicular load, room temperature, 22 N (5 lb)
Temperature Sensitivity	0.36%/°C (± 0.2%/°F)	Conductive heating

***All data above was collected utilizing an Op Amp Circuit (shown on the next page).** If your application cannot allow an Op Amp Circuit, visit www.tekscan.com/flexiforce-integration-guides, or contact a FlexiForce Applications Engineer.

DS Rev H 072720

ISO 9001:2008 Compliant & 13485:2016 Registered

Tekscan™

Appendix B (continued)

B.2

Electrical Data		
Nominal resistance	kOhm	5/10
Resistance tolerance	%	±20
Independent linearity	% of meas. range	±0.25
Electrical angle	°	150/354
Repeatability	°	max. 0.1
Temperature coefficient of the voltage divider	ppm/°C	50
Recommended wiper current	µA	max. 1
Max. wiper current in case of malfunction	mA	10
Power rating P	W/40°C	max. 0.5
Min. life (electrical)	movements	20 Mio.

Mechanical Data		
Mechanical range	° (continuous)	360
Torque	Ncm	max. 0.5
Min. life (mechanical)	movements	10 Mio.
Operating temperature	°C	-25 ... +75
Storage temperature	°C	-25 ... +105
Protection class		IP63

Standards		
Insulating resistance (500 VDC, 1bar, 2s)	GOhm	10
Dielectric strength (VAC, 50Hz, 1min, 1bar)	kV	1
Vibration (Amax = 0.75mm, f = 30…500 Hz)	g	10
Shock	g	50

GL60

Applications
- Door control system
- Road roller

Features
- Hollow shaft Ø 6mm
- 10 Mio. movements
- Excellent linearity up to ±0.25%
- Very good resolution, better 0,1°

Options
- Resistance tolerance ±10%
- Special electrical angles
- Radial cable outlet
- Mechanical end-stop

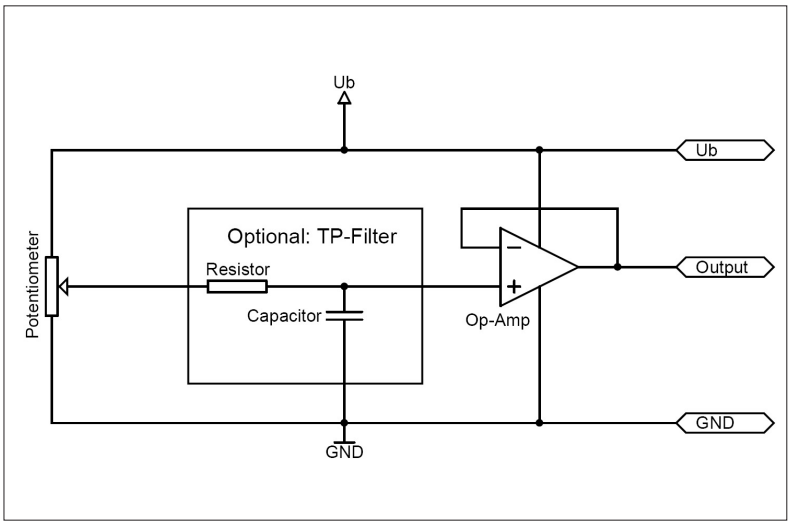

Ideal potentiometer wiring
Our potentiometers should be ideally used as an unloaded voltage divider.
If the potentiometer is loaded, nonlinearities arise due to the load resistance and the contact resistance.

Contelec AG
Portstrasse 38
CH-2503 Biel/Bienne
Telefon +41 (0)32 3665600
Telefax +41 (0)32 3665604
verkauf@contelec.ch

CONTELEC
A company of the Siedle-Group

Appendix B (continued)

B.3

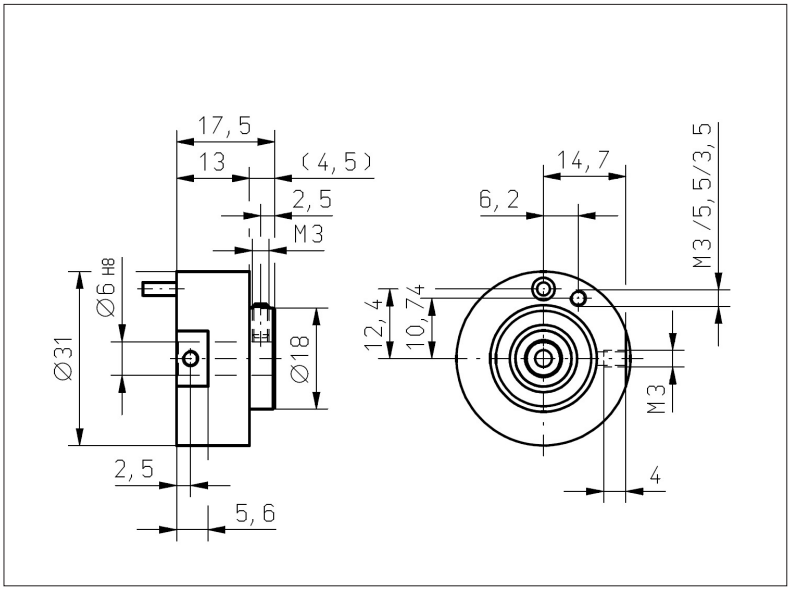

GL60

Accessories (incl.)
- None

Contelec AG
Portstrasse 38
CH-2503 Biel/Bienne
Phone +41 (0)32 3665600
Telefax +41 (0)32 3665604
sales@contelec.ch

CONTELEC
A company of the Siedle-Group

Appendix C

MATLAB CODE IMU SENSOR

```
function [ax,ay,theta,T] = SignalDetection()
persistent arduinomega imu9250 prevT
persistent ax_offset ay_offset thetaprime thetaprime_offset theta_offset


if isempty(arduinomega)
    arduinomega = arduino();
end
if isempty(imu9250)
    imu9250 = mpu9250(arduinomega);
end
%initialization output
ax=0;
ay=0;
theta=0;
T=0;
FUSE=imufilter;


%initialization computation parameters
```

Appendix C (continued)

```
21 if isempty(ax_offset)
       ax_offset=0;
23     ay_offset=0;
       prevT=0;
25     thetaprime_offset=0;
       theta_offset=0;
27

   %Compute avarage offset error produced by Accelerometer and Gyroscope
29     i_counter=100; %equal to sample rate
       for i=1:i_counter
31         if lt(i,i_counter)
               [accel,gyro]=read(imu9250);
33             [orientation,angvel] = FUSE(accel,gyro);
               thetaprime_offset=eulerd(orientation,'YZX','frame');
35         else
               [accel, gyro, ~, timestamp] = read(imu9250);
37             prevT = timestamp;
           end
39         ax_offset = ax_offset + accel(1);
           ay_offset = ay_offset + accel(2);
41         theta_offset=theta_offset + thetaprime_offset(1);
       end
43 ax_offset = ax_offset/i_counter;
```

Appendix C (continued)

```
ay_offset = ay_offset/i_counter;
theta_offset = theta_offset/i_counter;
end
%end of calibration\initialization
if isempty(ax)
     ax=0;
end
if isempty(ay)
     ay=0;
end
%read accelleration and velocity
[accel, gyro, ~, timestamp] = read(imu9250);
ax = accel(1) - ax_offset;
ay = accel(2) - ay_offset;
T= timestamp-prevT;
[orientation,angvel] = FUSE(accel,gyro);
thetaprime=eulerd(orientation,'YZX','frame');
theta=thetaprime(1)-theta_offset;
end
```

Appendix D

BLDC MOTOR DYNAMIC EQUATIONS

Stator phase voltages:

$$V_a = RI_a + (L - M)\frac{di_a}{dt} + e_a \tag{D.1}$$

$$V_b = RI_b + (L - M)\frac{di_b}{dt} + e_b \tag{D.2}$$

$$V_c = RI_c + (L - M)\frac{di_c}{dt} + e_c \tag{D.3}$$

where:

- V_a, V_b and V_c are the stator phase voltages;
- i_a, i_b and i_c are the stator phase currents;
- e_a, e_b and e_c are the phase back EMF;
- L,M and R is the self inductance, mutual inductance and phase resistance respectively.

Motor speed:

$$\frac{\omega_m}{dt} = \frac{P}{2J}(T_e - T_l - B\omega_r) \tag{D.4}$$

where:

- ω_m is the mechanical rotor speed;
- ω_r is the electrical rotor speed;

Appendix D (continued)

- T_e is the electromagnetic torque;
- T_l is the load torque;
- J is the motor inertia;
- B is the friction coefficient;
- P is the number of poles.

Trapezoidal back EMF:

$$e_{a,b,c} = f_{a,b,c}(\theta_r) \cdot E \tag{D.5}$$

where $E = k_e \omega_r$ and k_e is the back EMF constant, while $f_{a,b,c}(\theta_r)$ is function of rotor position. Depending on the rotor position, $f_{a,b,c}$ trapezoidal shape functions are generated, with upper and lower limit values equal to +1 and -1.

$$f_a(\theta_r) = \begin{bmatrix} \theta_r \frac{6}{\pi} & 0 < \theta_r <= \frac{\pi}{6} \\ 1 & \frac{\pi}{6} < \theta_r <= \frac{5\pi}{6} \\ -\theta_r \frac{6}{\pi} + 6 & \frac{5\pi}{6} < \theta_r <= \frac{7\pi}{6} \\ -1 & \frac{7\pi}{6} < \theta_r <= \frac{11\pi}{6} \\ \theta_r \frac{6}{\pi} - 12 & \frac{11\pi}{6} < \theta_r <= 2\pi \end{bmatrix} \tag{D.6}$$

Appendix D (continued)

$$f_b(\theta_r) = \begin{bmatrix} -1 & 0 < \theta_r <= \frac{\pi}{6} \\ \theta_r \frac{6}{\pi} - 4 & \frac{\pi}{6} < \theta_r <= \frac{5\pi}{6} \\ 1 & \frac{5\pi}{6} < \theta_r <= \frac{7\pi}{6} \\ -\theta_r \frac{6}{\pi} + 10 & \frac{7\pi}{6} < \theta_r <= \frac{11\pi}{6} \\ -1 & \frac{11\pi}{6} < \theta_r <= 2\pi \end{bmatrix} \tag{D.7}$$

$$f_c(\theta_r) = \begin{bmatrix} 1 & 0 < \theta_r <= \frac{\pi}{6} \\ -\theta_r \frac{6}{\pi} + 2 & \frac{\pi}{6} < \theta_r <= \frac{5\pi}{6} \\ -1 & \frac{5\pi}{6} < \theta_r <= \frac{7\pi}{6} \\ \theta_r \frac{6}{\pi} - 8 & \frac{7\pi}{6} < \theta_r <= \frac{11\pi}{6} \\ 1 & \frac{11\pi}{6} < \theta_r <= 2\pi \end{bmatrix} \tag{D.8}$$

Electronic torque

$$T_a = \frac{i_a e_a}{\omega_r} \tag{D.9}$$

$$T_b = \frac{i_b e_b}{\omega_r} \tag{D.10}$$

$$T_c = \frac{i_c e_c}{\omega_r} \tag{D.11}$$

CITED LITERATURE

1. Militerni, R.: Neuropsichiatria infantile. Idelson-Gnocchi, 2004.

2. Pavone, L. and Ruggieri, M.: Neurologia pediatrica. Elsevier Italia, 2015.

3. Wren, T. A., Rethlefsen, S., and Kay, R. M.: Prevalence of specific gait abnormalities in children with cerebral palsy: influence of cerebral palsy subtype, age, and previous surgery. Journal of Pediatric Orthopaedics, 25(1):79–83, 2005.

4. Valvano, J.: Activity-focused motor interventions for children with neurological conditions. Physical & occupational therapy in pediatrics, 24(1-2):79–107, 2004.

5. Bjornson, K. F., Belza, B., Kartin, D., Logsdon, R., and McLaughlin, J. F.: Ambulatory physical activity performance in youth with cerebral palsy and youth who are developing typically. Physical therapy, 87(3):248–257, 2007.

6. Rethlefsen, S. A., Blumstein, G., Kay, R. M., Dorey, F., and Wren, T. A.: Prevalence of specific gait abnormalities in children with cerebral palsy revisited: influence of age, prior surgery, and gross motor function classification system level. Developmental Medicine & Child Neurology, 59(1):79–88, 2017.

7. Hicks, J. L., Schwartz, M. H., Arnold, A. S., and Delp, S. L.: Crouched postures reduce the capacity of muscles to extend the hip and knee during the single-limb stance phase of gait. Journal of biomechanics, 41(5):960–967, 2008.

8. Arnold, A. S., Anderson, F. C., Pandy, M. G., and Delp, S. L.: Muscular contributions to hip and knee extension during the single limb stance phase of normal gait: a framework for investigating the causes of crouch gait. Journal of biomechanics, 38(11):2181–2189, 2005.

9. Thomas, S. S., Moore, C., Kelp-Lenane, C., and Norris, C.: Simulated gait patterns: the resulting effects on gait parameters, dynamic electromyography, joint moments, and physiological cost index. Gait & Posture, 4(2):100–107, 1996.

10. Prosser, L. A., Lee, S. C., VanSant, A. F., Barbe, M. F., and Lauer, R. T.: Trunk and hip muscle activation patterns are different during walking in young children with and without cerebral palsy. Physical therapy, 90(7):986–997, 2010.

CITED LITERATURE (continued)

11. Kawamoto, H., Lee, S., Kanbe, S., and Sankai, Y.: Power assist method for hal-3 using emg-based feedback controller. In SMC'03 Conference Proceedings. 2003 IEEE International Conference on Systems, Man and Cybernetics. Conference Theme-System Security and Assurance (Cat. No. 03CH37483), volume 2, pages 1648–1653. IEEE, 2003.

12. Sankai, Y.: Hal: Hybrid assistive limb based on cybernics. In Robotics research, pages 25–34. Springer, 2010.

13. Zoss, A. B., Kazerooni, H., and Chu, A.: Biomechanical design of the berkeley lower extremity exoskeleton (bleex). IEEE/ASME Transactions on mechatronics, 11(2):128–138, 2006.

14. Veneman, J. F., Kruidhof, R., Hekman, E. E., Ekkelenkamp, R., Van Asseldonk, E. H., and Van Der Kooij, H.: Design and evaluation of the lopes exoskeleton robot for interactive gait rehabilitation. IEEE Transactions on Neural Systems and Rehabilitation Engineering, 15(3):379–386, 2007.

15. Beyl, P., Vanderborght, B., Grosu, V., Van Damme, M., Van Ham, R., and Lefeber, D.: Knexo: a knee exoskeleton to test design and control concepts for gait rehabilitation. In New and Emerging Technologies in Assistive Robotics Workshop at IEEE/RSJ IROS 2011, Sep. 26 2011, pages 1–2, 2011.

16. Chen, B., Zhong, C.-H., Zhao, X., Ma, H., Guan, X., Li, X., Liang, F.-Y., Cheng, J. C. Y., Qin, L., Law, S.-W., et al.: A wearable exoskeleton suit for motion assistance to paralysed patients. Journal of orthopaedic translation, 11:7–18, 2017.

17. Zhang, D. and Wei, B.: Human–Robot Interaction: Control, Analysis, and Design. Cambridge Scholars Publishing, 2020.

18. Rossi, S., Colazza, A., Petrarca, M., Castelli, E., Cappa, P., and Krebs, H. I.: Feasibility study of a wearable exoskeleton for children: is the gait altered by adding masses on lower limbs? PloS one, 8(9):e73139, 2013.

19. Regnaux, J., Pradon, D., Roche, N., Robertson, J., Bussel, B., and Dobkin, B.: Effects of loading the unaffected limb for one session of locomotor training on laboratory measures of gait in stroke. Clinical biomechanics, 23(6):762–768, 2008.

20. Khanna, I., Roy, A., Rodgers, M. M., Krebs, H. I., Macko, R. M., and Forrester, L. W.: Effects of unilateral robotic limb loading on gait characteristics in subjects with chronic stroke. Journal of neuroengineering and rehabilitation, 7(1):1–8, 2010.

CITED LITERATURE (continued)

21. Rossi, S., Patanè, F., Del Sette, F., and Cappa, P.: Wake-up: A wearable ankle knee exoskeleton. In 5th IEEE RAS/EMBS International Conference on Biomedical Robotics and Biomechatronics, pages 504–507. IEEE, 2014.

22. Samadi, B., Achiche, S., Parent, A., Ballaz, L., Chouinard, U., and Raison, M.: Custom sizing of lower limb exoskeleton actuators using gait dynamic modelling of children with cerebral palsy. Computer methods in biomechanics and biomedical engineering, 19(14):1519–1524, 2016.

23. Lerner, Z. F., Damiano, D. L., Park, H.-S., Gravunder, A. J., and Bulea, T. C.: A robotic exoskeleton for treatment of crouch gait in children with cerebral palsy: Design and initial application. IEEE Transactions on Neural Systems and Rehabilitation Engineering, 25(6):650–659, 2016.

24. Lerner, Z. F., Damiano, D. L., and Bulea, T. C.: The effects of exoskeleton assisted knee extension on lower-extremity gait kinematics, kinetics, and muscle activity in children with cerebral palsy. Scientific reports, 7(1):1–12, 2017.

25. Eguren, D., Cestari, M., Luu, T. P., Kilicarslan, A., Steele, A., and Contreras-Vidal, J. L.: Design of a customizable, modular pediatric exoskeleton for rehabilitation and mobility. In 2019 IEEE International Conference on Systems, Man and Cybernetics (SMC), pages 2411–2416. IEEE, 2019.

26. Lerner, Z. F., Gasparri, G. M., Bair, M. O., Lawson, J. L., Luque, J., Harvey, T. A., and Lerner, A. T.: An untethered ankle exoskeleton improves walking economy in a pilot study of individuals with cerebral palsy. IEEE Transactions on Neural Systems and Rehabilitation Engineering, 26(10):1985–1993, 2018.

27. Fang, Y., Orekhov, G., and Lerner, Z. F.: Adaptive ankle exoskeleton gait training demonstrates acute neuromuscular and spatiotemporal benefits for individuals with cerebral palsy: A pilot study. Gait & Posture, 2020.

28. Wehner, M., Quinlivan, B., Aubin, P. M., Martinez-Villalpando, E., Baumann, M., Stirling, L., Holt, K., Wood, R., and Walsh, C.: A lightweight soft exosuit for gait assistance. In 2013 IEEE international conference on robotics and automation, pages 3362–3369. IEEE, 2013.

29. Marieswaran, M., Sikidar, A., Goel, A., Joshi, D., and Kalyanasundaram, D.: An extended opensim knee model for analysis of strains of connective tissues. Biomedical engineering online, 17(1):1–13, 2018.

CITED LITERATURE (continued)

30. Grosu, S., Rodriguez-Guerrero, C., Grosu, V., Vanderborght, B., and Lefeber, D.: Evaluation and analysis of push-pull cable actuation system used for powered orthoses. Frontiers in Robotics and AI, 5:105, 2018.

31. Wu, Q., Wang, X., Du, F., and Zhang, X.: Design and control of a powered hip exoskeleton for walking assistance. International Journal of Advanced Robotic Systems, 12(3):18, 2015.

32. Lerner, Z. F., Damiano, D. L., and Bulea, T. C.: Relationship between assistive torque and knee biomechanics during exoskeleton walking in individuals with crouch gait. In 2017 International Conference on Rehabilitation Robotics (ICORR), pages 491–497. IEEE, 2017.

33. Mentiplay, B. F., Banky, M., Clark, R. A., Kahn, M. B., and Williams, G.: Lower limb angular velocity during walking at various speeds. Gait & posture, 65:190–196, 2018.

34. Anderson, A., Richburg, C., Czerniecki, J., and Aubin, P.: A model-based method for minimizing reflected motor inertia in off-board actuation systems: Applications in exoskeleton design. In 2019 IEEE 16th International Conference on Rehabilitation Robotics (ICORR), pages 360–367. IEEE, 2019.

35. Schiele, A., Letier, P., Van Der Linde, R., and Van Der Helm, F.: Bowden cable actuator for force-feedback exoskeletons. In 2006 IEEE/RSJ International Conference on Intelligent Robots and Systems, pages 3599–3604. IEEE, 2006.

36. Carlson, L. E., Veatch, B. D., and Frey, D. D.: Efficiency of prosthetic cable and housing. JPO: Journal of Prosthetics and Orthotics, 7(3):96–99, 1995.

37. Sweeney, P., Lyons, G., and Veltink, P. H.: Finite state control of functional electrical stimulation for the rehabilitation of gait. Medical and biological engineering and computing, 38(2):121–126, 2000.

38. Strutzenberger, G., Alexander, N., De Asha, A., Schwameder, H., and Barnett, C. T.: Does an inverted pendulum model represent the gait of individuals with unilateral transfemoral amputation while walking over level ground? Prosthetics and orthotics international, 43(2):221–226, 2019.

39. McGrath, M., Howard, D., and Baker, R.: The strengths and weaknesses of inverted pendulum models of human walking. Gait & posture, 41(2):389–394, 2015.

CITED LITERATURE (continued)

40. Jasiewicz, J. M., Allum, J. H., Middleton, J. W., Barriskill, A., Condie, P., Purcell, B., and Li, R. C. T.: Gait event detection using linear accelerometers or angular velocity transducers in able-bodied and spinal-cord injured individuals. Gait & posture, 24(4):502–509, 2006.

41. Bishop, E. and Li, Q.: Walking speed estimation using shank-mounted accelerometers. In 2010 IEEE International Conference on Robotics and Automation, pages 5096–5101. IEEE, 2010.

42. Hirata, N. S.: 1 stack filters: From definition to design algorithms. Advances in Imaging and Electron Physics, 152:1, 2008.

43. Liu, Y., Noguchi, N., and Ishii, K.: Development of a low-cost imu by using sensor fusion for attitude angle estimation. IFAC Proceedings Volumes, 47(3):4435–4440, 2014.

44. Gasparri, G. M., Luque, J., and Lerner, Z. F.: Proportional joint-moment control for instantaneously adaptive ankle exoskeleton assistance. IEEE Transactions on Neural Systems and Rehabilitation Engineering, 27(4):751–759, 2019.

45. Ranzani, R.: Adaptive human model-based control for active knee prosthetics. Master's thesis, ETH Zürich, 2014.

46. Murray, S. A., Ha, K. H., and Goldfarb, M.: An assistive controller for a lower-limb exoskeleton for rehabilitation after stroke, and preliminary assessment thereof. In 2014 36th Annual International Conference of the IEEE Engineering in Medicine and Biology Society, pages 4083–4086. IEEE, 2014.

47. Tagliamonte, N. L., Valentini, S., Sudano, A., Portaccio, I., De Leonardis, C., Formica, D., and Accoto, D.: Switching assistance for exoskeletons during cyclic motions. Frontiers in neurorobotics, 13:41, 2019.

48. Lencioni, T., Carpinella, I., Rabuffetti, M., Marzegan, A., and Ferrarin, M.: Human kinematic, kinetic and emg data during different walking and stair ascending and descending tasks. Scientific data, 6(1):1–10, 2019.

49. Ali, S. A., Annuar, K. A. M., and Miskon, M. F.: Trajectory planning for exoskeleton robot by using cubic and quintic polynomial equation. International Journal of Applied Engineering Research, 11(13):7943–7946, 2016.

50. Siciliano, B., Sciavicco, L., Villani, L., and Oriolo, G.: Robotics: modelling, planning and control. Springer Science & Business Media, 2010.

CITED LITERATURE (continued)

51. Agrawal, L. K., Chauhan, B. K., and Banerjee, G.: Speed control of brushless dc motor using fuzzy controller. International Journal of Pure and Applied Mathematics, 119(15):2689–2696, 2018.

52. Tibor, B., Fedak, V., and Durovskỳ, F.: Modeling and simulation of the bldc motor in matlab gui. In 2011 IEEE International Symposium on Industrial Electronics, pages 1403–1407. IEEE, 2011.

53. Angeti, J., Kadalla, A. S., and Zirata, B. K.: Speed control of bldc motor using fuzzy: Tuned pid controller. Communications, 7:6–12, 2019.

54. Lee, B.-K. and Ehsani, M.: Advanced simulation model for brushless dc motor drives. Electric power components and systems, 31(9):841–868, 2003.

55. Mahmud, M., Motakabber, S., Alam, A., and Nordin, A. N.: Control bldc motor speed using pid controller. International Journal of Advanced Computer Science and Applications (IJACSA), 11(3):477–481, 2020.

56. Basilio, J. C. and Matos, S.: Design of pi and pid controllers with transient performance specification. IEEE Transactions on education, 45(4):364–370, 2002.

VITA

NAME	Sara Lo Vecchio
EDUCATION	
	Master of Science in Electrical and Computer Engineering, University of Illinois at Chicago, October 2019 - present, USA
	Master of Science in Mechatronic Engineering, October 2019 - present, Polytechnic of Turin, Italy
	Bachelor's Degree in Biomedical Engineering, October 2019, Polytechnic of Turin, Italy
LANGUAGE SKILLS	
Italian	Native speaker
English	Full working proficiency
	2018 - TOEFL examination (98/120)
	A.Y. 2020/21 One Year of study abroad in Chicago, Illinois
	A.Y. 2019/20 Lessons and exams attended exclusively in English
Spanish	Full working proficiency
	A.Y. 2018/2019 Erasmus+/Young Talents program in Madrid, Spain
SCHOLARSHIPS	
Spring 2021	Italian scholarship for final project (thesis) at UIC
Fall 2020	Italian scholarship for TOP-UIC students
Fall 2018	European scholarship for Erasmus+/Young Talents program in Madrid, Spain
2016 - 2019	Italian scholarship for "Giovani Talenti" program at Polytechnic of Turin, Italy
TECHNICAL SKILLS	
Advanced level	Programming in C, MATLAB/Simulink, Python;
	CAD Modeling with Fusion360, SolidWorks, AutoCAD;

VITA (continued)

WORK EXPERIENCE AND PROJECTS

Spring and Summer 2021	Internship position at Shirley Ryan AbilityLab in Chicago, IL
Spring 2019	Training as Orthopedics prosthesis Designer at Officina Ortopedica "Maria Adelaide", Turin, Italy